Deriving Beach Grain Size from Satellite Imagery

A multimethod approach for deriving intertidal beach slopes and sediment grain sizes for different coastal environments

Menno Onrust

Deltares
Enabling Delta Life

TU Delft

Deriving Beach Grain Size from Satellite Imagery

A multimethod approach for deriving intertidal beach slopes and sediment grain sizes for different coastal environments

by

Menno Onrust

Email: monrust.tudelft@outlook.com

to obtain the degree of

Master of Science
in Civil Engineering,

to be defended publicly on Monday 20 April 2020 at 16:00.

Thesis comittee

Chair	Prof. dr. ir. S.G.J. Aarninkhof,	TU Delft
Supervisor	dr. ir. A.P. Luijendijk,	TU Delft / Deltares
	ir. W.P. de Boer,	TU Delft / Deltares

An electronic version of this thesis is available at `https://repository.tudelft.nl/`.

Delft University of Technology
Department of Coastal Engineering

"Eternity begins and ends with the ocean's tides"

Preface

This thesis presents my research into deriving the grain size of the beach using satellite imagery. It is the final product of my graduation project which is the last hurdle for obtaining the degree of Master of Science. It concludes my master's programme in Hydraulic Engineering at the Delft University of Technology. The research has been carried out in collaboration with Deltares.

Writing this thesis has been a journey into the fascinating world of remote sensing. I am amazed by the endless possibilities of using satellite imagery and I am eager to see the future applications. I foresee that the usage of 'big data' in the field of Civil Engineering is becoming increasingly popular and hope to have contributed to that with this thesis.

This report was written from the perspective of a hydraulic engineer. Anyone with a background in Hydraulic Engineering should be able to understand the approach, results and conclusions presented in this report. An abundance of background information is provided, especially on the remote sensing part, so that no prior knowledge on satellite imagery is required.

This thesis is the product of a long process; the past few months have been a concatenation of long days, sleepless nights, hope for good results and occasionally followed by a eureka moment. It has been a interesting but tough challenge and I cannot thank enough my friends and fellow students who provided me with the necessary distraction.

I want to thank my thesis committee for their enthusiasm and valuable feedback. Arjen Luijendijk foremost, whose ideas and critical comments helped me improve the quality of this research significantly.

Special thanks go to my grandfather Opa Douwe. Not only for being an amazing grandfather, but also I really appreciate your feedback on the English in my report. Last, thanks to you, reader. If you are reading this line after the others, you at least read one page of my thesis. Thank You.

Enjoy your reading!

Menno Onrust
Delft, 6 April 2020

Abstract

The world's coasts are at risk: an estimated 24 % of the world's beaches are eroding. Extreme events such as storms continuously threaten the coastal region and pose a serious risk of coastal flooding. Under the influence of climate change, the seaward pressures are only expected to increase. Sea level rise is accelerating, storm intensities and frequencies will increase, and precipitation will become more extreme.

At the same time human pressures such as coastal tourism and rapid urbanisation impose stresses to the coastal system. An estimated 23 % of the world's population lives in the coastal zone where natural hazards cause a direct flood risk. Protection of the coastal region becomes more and more relevant.

Coastal management strategies need to take the local circumstances into account. Therefore, a good understanding of the coastal zone is needed, but especially in data-poor regions there is a lack of geomorphological information such as slope and grain size. This thesis presents an alternative approach for acquiring this data with the ability to run on a global scale using remote sensing technologies. Remote sensing, satellite imagery in particular, has proven to be a promising new technology to monitor coastal regions at large temporal and spatial scales and is applied here to determine coastal slopes and sediment sizes.

This research implements a two-step approach. First, optical satellite images analysed using the Google Earth Engine . Three methods (FAST, Sagar and Onrust) are used to derive the slope of the intertidal beach from Sentinel-2 images. Second, the median grain size is estimated with help of two beach face slope relations from literature (Bujan, McFall).

Three study sites have been selected (Delfland coast, Duck coast & Hasaki coast) for validating the method presented in this thesis. The intertidal beach slope derived by satellite and the median grain size derived by satellite are validated individually.

It is found that there is good agreement between the observed and the satellite derived slopes with an average deviation of approximately 22 %. The results indicate that the beach face slope is very sensitive to the definition of the beach face. Depending on the tidal phase and wave height of the incoming waves a different zone would be selected; this makes it hard to compare the observed slopes to the satellite derived slopes.

Furthermore, the results show that the approach is able to differentiate between different sediment classes (e.g. fine, medium or coarse sands) for all study sites. Although estimated grain diameters are still off, this is a big leap forward as it first attempt at estimating the sediment size using generally available data.

Due to the limited spatial resolution, the approach for deriving sediment size from satellite imagery can only be applied to beaches with an intertidal zone that spans multiple pixels (> 20 m). Furthermore, the method is only suitable for stable beaches with little erosion or accretion and for beaches made of unconsolidated granular sediments.

It can be concluded that the approach presented in this thesis is very promising and paves the way for an estimate of the grain size at beaches around the world. Some hurdles remain to be taken but this thesis is clear on the future of coastal monitoring: satellite imagery and big data will change the way we study our coasts forever. This research is a major step forwards in the global monitoring of the world's coasts, but only shows the beginning of the endless possibilities.

Contents

Appendices

Acronyms & Symbols

List of Acronyms

BOA	Bottom Of Atmosphere
CRAB	Coastal Research Amphibious Buggy
DEM	digital elevation model
ESA	European Space Agency
FAST	Foreshore Assessment using Space Technology
FRF	Field Research Facility (of the U.S. Army Corps of Engineers)
GEBCO	General Bathymetric Chart of the Oceans
GEE	Google Earth Engine (geospational cloud computing platform)
GPS	Global Positioning System
HAT	highest astronomical tide
HORS	Hazaki Oceanographical Research Station
JarKus	annual coastal monitoring programme by Rijkswaterstaat (JAaRlijkse KUStmetingen)
LAT	lowest astronomical tide
LARC	Lighter Amphibious Resupply Cargo
LECZ	Low Elevation Coastal Zone
LTS	Least Trimmed Squares algorithm for robust linear regression
MNDWI	Modified Normalised Difference Water Index
MODIS	Moderate Resolution Imaging Spectroradiometer
MSI	Multispectral Instrument
MSL	mean sea level
NASA	National Aeronautics and Space Administration
NAP	Normaal Amsterdams Peil, or Amsterdam Ordnance Datum (vertical datum used in the Netherlands)
NAVD88	North American Vertical Datum of 1988
NDWI	Normalised Difference Water Index
NEMO	Nearshore Monitoring and Modelling Project
NIR	near-infrared (light in the 0.7 to 0.9 μm wavelength range)
RCP	Representative Concentration Pathway (greenhouse gas concentration trajectory adopted by the IPCC)
RMSE	Root Mean Square Error
SDS	Satellite Derived Shoreline
SLR	sea level rise (absolute)
SRTM	Shuttle Radar Topography Mission, a data set of digital elevation model (DEM) data
SWIR	short-wave infrared (light in the 1.6 to 2.2 μm wavelength range)

TEA	Time Ensemble Averaged
TOA	top of atmosphere

List of Symbols

β	slope angle of the beach face
$d50$	median grain diameter [mm]
g	gravitational acceleration [m/s^2]
h	elevation (positive up) [m]
H_b	breaker wave height [m]
H_s	significant wave height [m]
T	wave period [s]
T_p	peak wave period [s]
x	cross-shore distance (positive offshore) [m]
y	alongshore distance [m]

1 Context and research outline

The coastal region accommodates a significant part of the world population. Also, the same region is under pressure: many coasts are eroding. Hazards such as sea level rise (SLR) are imminent; protection of the coastal region becomes more and more relevant. However, an accurate global data set of basic geomorphological data such as slope and grain size does not exist. This chapter aims at providing the context and outline of this research. In addition, a reading guide is provided.

1.1 The coastal zone

The coastal zone is the interface between land and sea. It is defined as the part of the land affected by the proximity of the sea and the part of the sea affected by its proximity to the land. In this thesis the coastal zone is limited to areas within a 100 km distance from the shore and less than 100 m above sea level. Low-lying areas within the coastal zone, with an elevation less than 10 m above mean sea level (MSL), are referred to as the Low Elevation Coastal Zone (LECZ).

Coasts are highly vulnerable to extreme events such as storms. Simultaneously, human pressures such as coastal tourism and rapid urbanisation impose stresses to the coastal system (Hinkel et al., 2013; McGranahan et al., 2007; Nicholls et al., 2007). The attraction of the coast resulted in a disproportionate rapid expansion of economic activities, settlements, urban centres and tourist resorts (Nicholls et al., 2007) and this trend is expected to continue.

The coastal zone is densely populated: an estimated 23 % of the world's population lives in the coastal zone (Nicholls et al., 2007). Coastal communities in the LECZ are especially vulnerable as seaward hazards pose a direct flood risk. 13 % of the world's urban population lives in these areas (Seto & Shepherd, 2009).

1.2 Imminent coastal hazards

Luijendijk et al. (2018) report that 24 % of the world's coasts are eroding. The level of protection from retreating coasts decreases, so they pose a threat to coastal communities. Also, marine protected coastlines are at risk. In addition to the existing threats from seaward hazards, climate change will increase the risk of erosion and flooding. This will have adverse physical and socio-economical impacts on the world's coasts.

The new IPCC report about the ocean and the cryosphere in a changing climate summarises the latest findings in global climate research. IPCC (2019) concluded

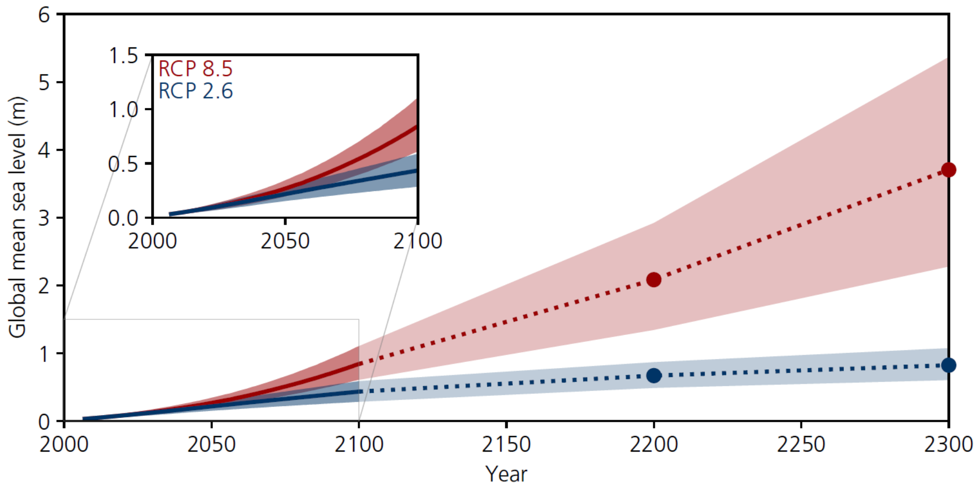

Figure 1.1: Projected rise of the global mean sea level until 2300. The inset shows an assessment of the *likely* range of the projections for climate scenarios RCP2.6 and RCP8.5 up to 2100. (IPCC, 2019)

that there is SLR due to climate change and that the rate of SLR is increasing (see figure 1.1). IPCC (2019) also warns for increased storm intensities and frequencies.

Extreme sea level events that are historically rare are projected to occur frequently. IPCC (2019) predicts with high confidence that local sea levels that historically occurred once per century will occur at least annually by 2100 under all climate scenarios, or Representative Concentration Pathways (RCPs). Local subsidence caused by natural processes and human activities aggravate the effect of SLR. Coastal hazards will be exacerbated by the projected increases in tropical cyclone intensity and precipitation (IPCC, 2019). Associated storm surge and wave heights are expected to increase.

1.3 Coastal protection

Reducing the risk of disaster in coastal settlements, coastal flooding in particular, presents a challenge for engineers. McGranahan et al. (2007) state that it is too late to rely only on mitigating measures to reduce the flood risk. Reducing the risk of disaster in low-lying urban areas will require a combination of mitigation, migration and coastal protection. Figure 1.2 summarises the possible responses to the rising water levels.

Hinkel et al. (2013) expect that 1.6 to 5.3 million people are forced to migrate (retreat) in the 21st century with an associated migration costs of $US\$300$ to 1000 billions. Strategic coastal protection measures, in the form of beach nourishments, can reduce these costs by (77 to 84) %. Hinkel et al. (2013) only quantify the impact of climate change on a global level, but do not provide a strategy for local coastal management.

Coastal management is a local matter: Coastal protection can effectively reduce the risks of coastal flooding, but depends on large investments. Such investments are only cost efficient for densely populated urban areas. Engineers will need to develop coastal management strategies taking into account the local political and socio-economical circumstances. Protection is not always the best solution.

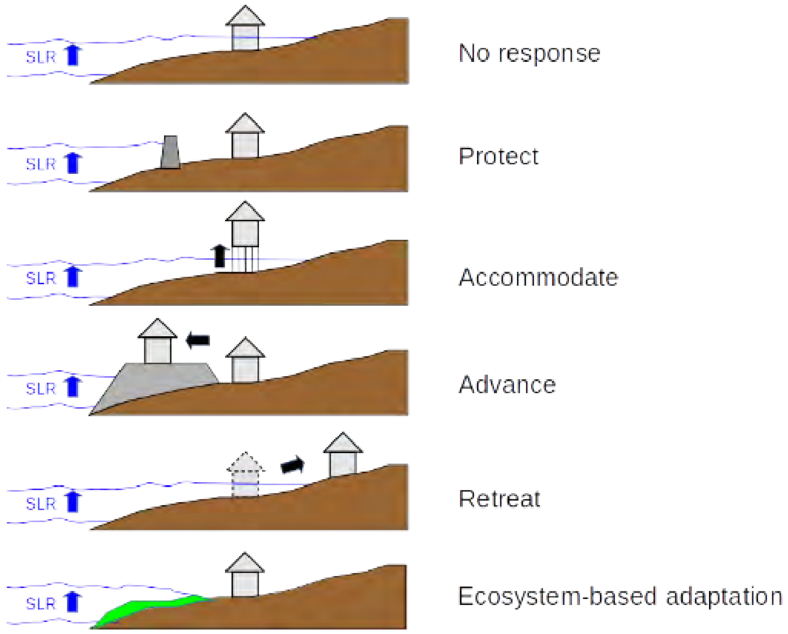

Figure 1.2: Different types of responses to coastal risk and SLR. (IPCC, 2019)

The Bruun rule (Bruun, 1962) for the representation of the coastal response to SLR is inadequate (Dickson et al., 2007); a morphodynamic method is required. Thus, engineers will have to employ physical or numerical coastal models. The grain size of the beach sediments is essential for determining the impact of storms (Roelvink & Reiniers, 2011). Also, the nearshore bathymetry is one of the most important input requirements of any coastal numerical model (Roelvink & Reiniers, 2011). Although current observation methods are generally simple and cheap, they are often laborious and have a small spatial coverage. As a result, a global data set of grain size data and nearshore bathymetry is missing: there is a need for improved basic coastal geomorphological data (Hinkel et al., 2013).

1.4 Recent developments in coastal research

With the engineering challenges related to coastal erosion laying ahead, there is renewed interest in solving the data gap. Much effort is placed on data-poor environments. Researchers are particularly interested in understanding the dynamics of the beach face, because little is known about the morphodynamics. The beach face is the part that interacts regularly with wave run-up and its shape can respond on short timescales. Recently, McFall (2019) related the sediment grain size to the beach face slope in order to gain better understanding of the expected beach face slope for different beach exposures. The high correlation coefficients show that there is good agreement with data from 181 beaches around the world.

Another recent development is in the use of space-borne remote sensing techniques for coastal monitoring. These techniques, referred to as satellite imagery, have proven to be a promising new technology to monitor changes in coastal waters (Hoepffner & Zibordi, 2009). Satellite imagery with application in the Coastal Engineering field is emerging, especially since the launch of the Google Earth Engine (GEE), Google's platform for analysing satellite imagery.

Currently, the main application of satellite imagery in Coastal Engineering is coastal monitoring. Luijendijk et al. (2018); Vos et al. (2019) have applied shoreline detection algorithms to detect the variability and evolution of shorelines. Bishop-Taylor et al. (2019); Sagar et al. (2017) have applied a water detection algorithm to optical satellite images and combined it with tidal elevation data to extract the intertidal extent and topography of the Australian coastline. FAST (2017) employed satellite imagery for deriving the slope in the intertidal zone. The use of space-born remote sensing in Coastal Engineering practice is an active field of research and new possibilities are still being explored. It seems that satellite imagery can cantribute to an improved data set of basic coastal geomorphological data.

1.5 Research question and objectives

This thesis explores the possibilities of deriving the sediment grain size using remote sensing data. Researchers come up with new applications of multispectral remote sensing, but the idea of using it to estimate grain size is not new: Leu (1977) already explored this idea in 1977 using the spectral reflectance but was unsuccessful. In this graduation project a different approach is investigated. The main question in this research is:

To what level can we derive the beach grain size using Sentinel-2 images?

The main goal of this research is to present an approach for deriving beach grain size from satellite imagery. The starting point is a two-step approach where satellite imagery is employed to derive the coastal slopes and empirical formulae are used to relate these to the grain size. The two steps are represented by the two research objectives:

1. To derive the intertidal beach slope from optical satellite imagery
2. To determine the sediment size from satellite derived intertidal beach slopes

For both objectives multiple methods are evaluated. The methods are based on existing methods from literature and are adjusted to achieve the research objectives: the focus is not on improving these methods.

This thesis is limited to the use of Sentinel-2 images, because of the high spatial and temporal resolution. In the analysis of the imagery, only unsupervised classifiers are considered because machine learning classifiers (supervised) tend to become a black box. With global data availability this method has the potential to be employed at a global scale, but that is outside the scope of this report. This thesis only deals with the development of a new approach to derive the grain diameter and the validation of this approach at three study sites.

1.6 Reading guide

This report consists of 8 chapters. Relevant background information is given in chapter 2. This chapter also gives an overview of the existing knowledge.

The research methodology is described in chapter 3. The various steps of this research are presented. A multimethod approach is adopted: three methods for deriving the intertidal beach slope from satellite imagery are highlighted. Two methods for estimating the grain size of the beach are given.

Chapter 4 shows the results for the first research objective: the satellite derived intertidal slopes. Chapter 5 shows the results for the second research objective: the sediment grain sizes.

The discussion in chapter 6 reflects on the obtained slopes and grain sizes. It also reflects on the limitations and applicability of the methods involved.

The final chapter is chapter 7 with the main conclusions of this thesis, and with three recommendations for future research.

2 Background information

This chapter gives the necessary background information and an overview of the present knowledge related to the research objective. The first section (2.1) describes the beach profile and gives some key definitions. Next, the beach face is discussed with focus on the relation between the beach face slope and the sediment grain size. Section 2.4 deals with the background information of satellite imagery and image processing techniques. 2.5 summarises the approach by Hagenaars (2017) in which these techniques are used to extract the shoreline from satellite images.

2.1 The beach profile

The term “beach profile” refers to a cross-sectional trace of the beach perpendicular to the high tide shoreline and extends from the backshore cliff or dune to the inner continental shelf or a location where waves and currents do not transport sediment to and from the beach.

The beach profile is an important term in this thesis. Figure 2.1 shows a beach profile, where the important definitions are pointed out:

Bar elongated sand body created by currents or by waves.

Beach zone of unconsolidated material that extends from the (low-water) shoreline to the dunefoot or the line of permanent vegetation.

Beach face seaward section of the beach which is exposed to and shaped by the action of the waves.

Intertidal zone area of the shore within the tidal range. In other words, it is the area that is above water level at low tide and underwater at high tide. The intertidal zone is often synonymous with the beach face; in this thesis it is used to point out the same area as the beach face.

Shoreline boundary line between land and water.

The beach profile has always been of interest to researchers as it provides useful information for the scientific understanding of coastal processes (Andrade & Ferreira, 2006). Traditionally, beach surveys were performed using the Emery board method (Emery, 1961), which is very labour intensive. More recent methods, such as GPS surveying, video derived bathymetry (Aarninkhof, 2003) or LIDAR (Light Detection And Ranging) measurements, have overcome this disadvantage. Unfortunately, these surveying techniques only have a small spatial coverage, and thus cannot be used to obtain a global data set.

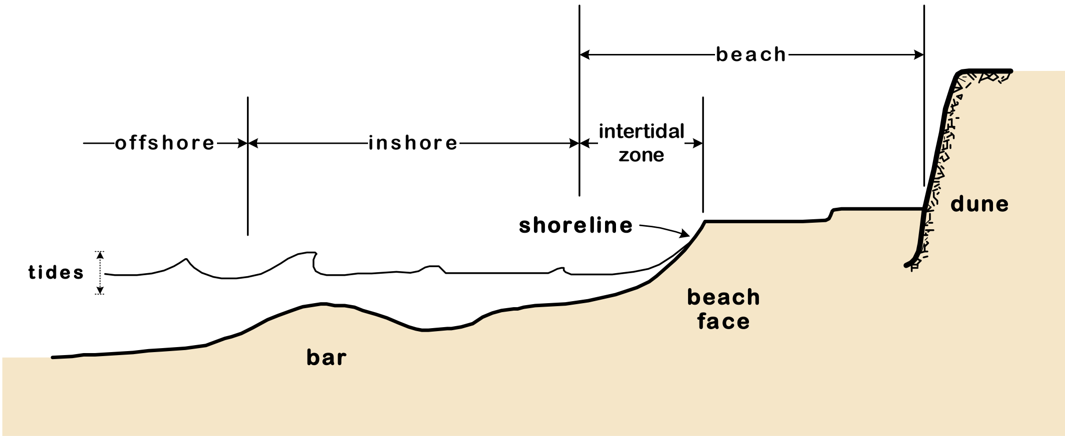

Figure 2.1: Definitions of the beach profile Adopted from US Army 2002.

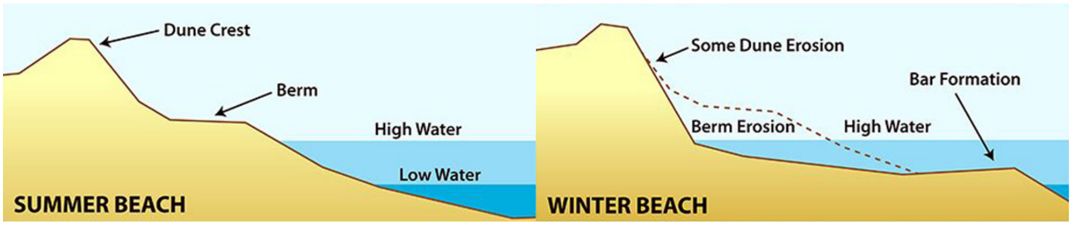

Figure 2.2: Schematic of the difference between the summer and winter beach. Waves are generally more powerful in winter resulting in a flatter shape of the beach.

The beach environment is an extremely complex one in which many process variables affect the form of the beach through the movement of, and change in, the material of which it is composed (King & Mather, 1972). Under the influence of wind, waves and the tides, the shape of the beach is always evolving. The variability depends on the time of year within the annual beach cycle and the elapsed time after a storm. As storms are accompanied with a lot of wave action, they have a significant impact on the morphology of a coast. Water level and grain size are other controlling factors of the beach profile shape.

Storms erode the beach and give rise to the formation of a storm or 'winter' profile. During the storm season, which is in winter on the Northern Hemisphere, sand from the beach is deposited lower in the profile. This often results in the formation of an alongshore sand bar. Figure 2.2 shows a schematic of the difference between the summer and the winter beach. Typically, the summer profile is steeper than the winter profile. Intertidal bars enlarge the horizontal extent of the intertidal zone resulting in flat slopes.

The variability of the profile shape is most widespread at the beach face due to the constant movement of sediment by the swash processes. These variations have response times of several days or even minutes (Holland & Holman, 1996).

2.2 The equilibrium beach profile

An equilibrium beach profile describes the equilibrium state of the beach profile. Even though an equilibrium state does not exist in the dynamic coastal environment, these models are widely used. Fenneman (1902) was one of the first to describe the concept:

> "It is the form of the profile which the water is striving to give to the shore; towards this form it is continually tending."

The equilibrium beach profile is mainly a theoretical concept: a shore can only be in equilibrium under constant forcing (of wind, waves, currents, etc.); such conditions seldom, if ever, occur in nature. Experiments in the laboratory (among others Bruun, 1954; Sunamura, 1984), however, have successfully produced a stable profile without net transport of sediment.

Beach profile models have proven to be a useful tool for describing the overall average form of the shore (Work & Dean, 1991). Although beach profiles may have deviant shapes, such as bars and troughs, in general they are steepest at the shoreline and have a progressively decreasing slope as the water depth increases in the offshore direction (Komar & McDougal, 1994). Numerous models have been developed; in this research the following two models are used:

- Bruun model (Bruun, 1954; Dean, 1977)
- Bernabeu model (*or 2-Step equilibrium beach profile;* Bernabeu et al., 2003)

Appendix B will go more into depth about the existing beach profile models. The two models mentioned above are discussed hereafter.

Bruun model

The Bruun model has seen the most widespread use in coastal-engineering application (N. J. Cooper Beng et al., 2000) and is often considered a good indicator of the theoretical beach profile expected. The Bruun model has the following form:

$$h = A_1 x^{2/3} \quad \text{with} \quad A_1 = 2.25 \left(\frac{w_f^2}{g} \right)^{2/3} \tag{2.1}$$

Where h is the water depth, x is the cross-shore distance from the waterline and A_1 is an empirical parameter based on the settling velocity of sediments (w_f).

Bernabeu model

Dissatisfied with the already available models, Bernabeu et al. (2002) developed the 2-Step Equilibrium Beach Profile model. It is a based on the assumption that surf zone processes dominate the profile morphology. The equilibrium beach profile consists of two steps, with separate relations for the surf zone and the shoaling zone:

Surf profile:
$$x = \left(\frac{h}{A_2} \right)^{3/2} + \frac{B_2}{A_2^{3/2}} h^3 \tag{2.2}$$

Shoaling profile:
$$X = x - x_0 = \left(\frac{h}{C_2} \right)^{3/2} + \frac{D_2}{C_2^{3/2}} h^3 \tag{2.3}$$

Where h is the water depth and x is the cross-shore distance from the waterline. A_2, B_2, C_2 & D_2 are scale parameters based on the grain size.

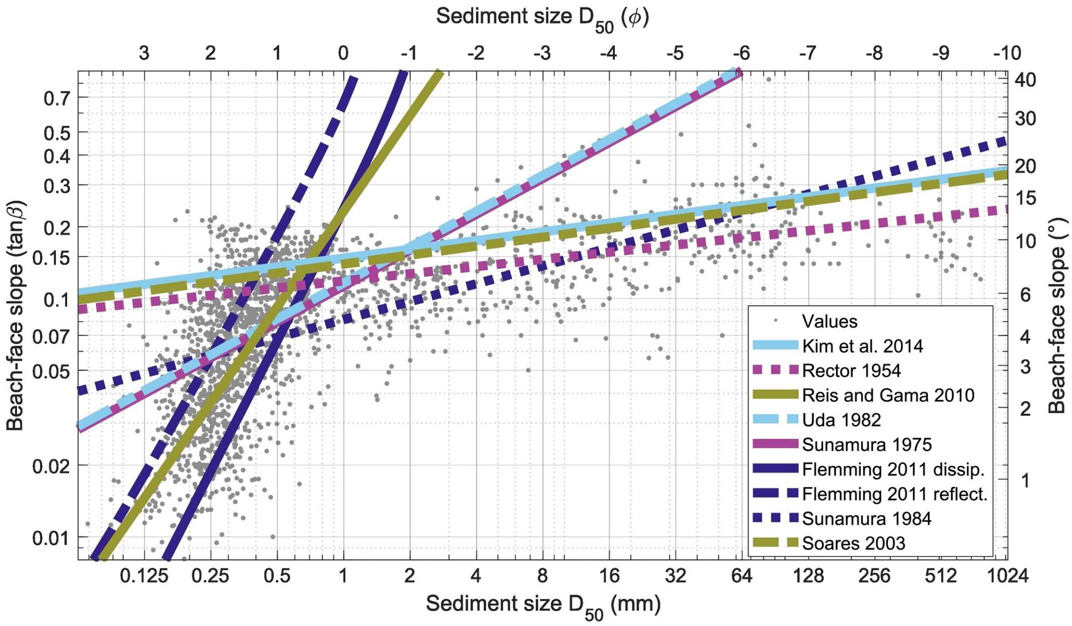

Figure 2.3: Overview of the existing beach face relations. The most recent methods (Bujan et al. (2019); McFall (2019)) are not included. (Bujan et al., 2019)

2.3 The beach face

The beach face is the most dynamic part of the beach profile. The dynamics are controlled by numerous variables, including the beach sediment characteristics, the wave properties, the groundwater level, the tidal stages and the velocity of the alongshore current. This creates an extremely complex environment in which the detailed processes involved are not fully understood.

Grain size of the beach sediment, wave height and wavelength are generally considered the governing physical quantities controlling the beach face slope (Bujan et al., 2019; Madsen & Plant, 2001; McFall, 2019; McLean & Kirk, 1969; Reis & Gama, 2010; Sunamura, 1984). Larger grains are associated with steeper beaches, whereas more energetic conditions (larger wave height) are associated with flatter beaches.

A number of empirical relations were developed in previous research activities relating the beach face slope to the parameters mentioned before. Bujan et al. (2019) provide an overview of the existing relations; this overview is presented in figure 2.3. This research focusses on the relations by Bujan et al. (2019); McFall (2019) (see table 2.1), because these relations are valid accross the entire range of grain sizes. Appendix B.3 provides more background on the dynamics of the beach face and the different beach face models.

2.4 Satellite imagery

Earth observation is the gathering of information of our planet via remote sensing technologies. Earth observation in this thesis is limited to images acquired using space-borne equipment, or satellite images. More specifically, this research focusses on optical satellite imagery; that is images with wavelengths in the visible spectrum. Analysis of satellite imagery forms the basis of this thesis.

Source	Equation	Parameters
Bujan et al. (2019)	$\tan\beta = a_4\,(d50 - 0.125)^{b_4} + c_4$	$a_4 = -0.154$ $b_4 = -0.145$ $c_4 = 0.268$
	Based on an analysis of a data set from 2144 measurements of beach face slope and associated grain sizes from beaches around the world. The entire range of grain sizes from very fine sand (0.07 mm) to boulders (770 mm) is represented in the data set, as well as a large variety of beach face slopes.	
McFall (2019)	$\tan\beta = 1\,/\,(a_5)\cdot d50^{n_5}$	$H_{s12}\begin{cases} < 1 & a_5 = 3.1, n_5 = 1.1 \\ \vdots & a_5 = 2.1, n_5 = 1.8 \\ > 3 & a_5 = 3.9, n_5 = 1.85 \end{cases}$
	Based on an analysis of a data set from 181 sand beaches around the world. Only sand beaches (0.1 to 1.0 mm) are represented in the data set, but a large variety of beach face slopes are included. Sediment sorting was minimised in the study.	

Table 2.1: Formulae expressing the beach face slope as a function of sediment size. Only the Bujan and McFall relation are considered, more models are discussed in appendix B.3.

2.4.1 Optical remote sensing

Satellite images are pixel based geospatial data sets. Light intensities are recorded in different ‘bands’: the instruments of the satellites are sensitive in specific wavelength ranges. Figure 2.4 shows the band configuration for the Sentinel-2, Landsat 8 and Landsat 7 satellites. All have a dedicated bands for visible red, green and blue light and are thus optical satellites.

Satellite missions

Although there are over 700 earth observing satellites in orbit, only few are suitable. Most satellite missions do not publicly release all images or only work on assignment. The American Landsat programme and the European Copernicus programme, featuring the Sentinel-2 mission, have an open data policy so scenes from these programmes are freely available.

NASA’s Landsat programme is the longest running space observation programme, with over 45 years of imagery. Each of the Landsat missions provides images with a 30 metre resolution and a revisit time of 16 days; Landsat 7 and Landsat 8 combined yields a temporal resolution of 8 days. The Sentinel family of satellites from ESA’s Copernicus programme provide high-quality earth observation data sets with optical imagery from the Sentinel-2 mission. The Sentinel-2 mission provides high resolution images with a 10 metre resolution and a revisit time of 5 days.

The high temporal resolution of the Sentinel-2 mission is an advantage for deriving the coastal slopes: Satellite images show the instantaneous situation, but deriving the intertidal beach slope requires combining multiple images. A short revisit time is desired in order to minimise morphological changes between consecutive images. In addition, the higher spatial resolution can help achieve a better accuracy. Therefore,

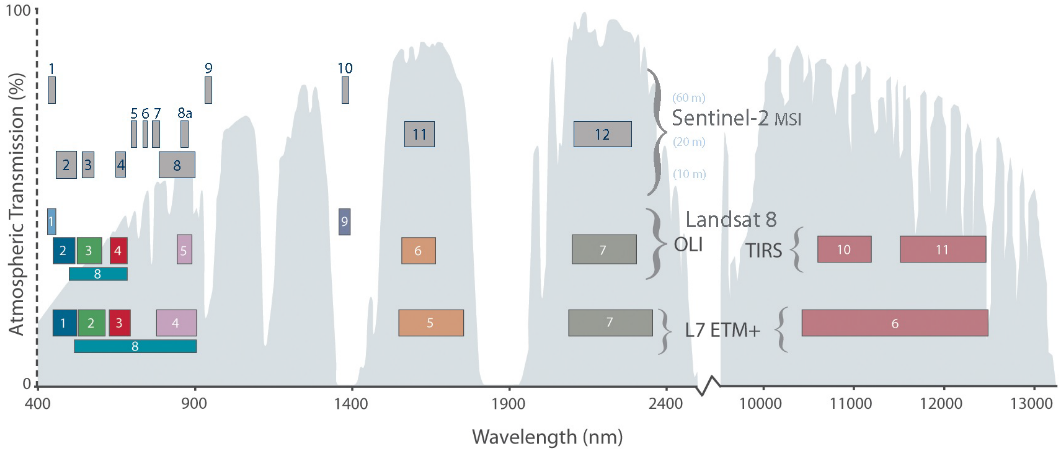

Figure 2.4: Band configuration of the Sentinel-2, Landsat 8 and Landsat 7 sensors. Light in the visible spectrum (blue 490 nm, green 560 nm and red 665 nm) is recorded by all sensors. The bands for the different sensors are comparable, except for the thermal band (11000 nm) which is not found on the Sentinel-2.

	Spatial resolution	Revisit time	Operational since
Sentinel-2	10 m	5 days	June 2017 (October 2015)
Landsat 8	30 m	16 days	May 2013
Landsat 7	30 m	16 days	June 1999

Table 2.2: Characteristics of the satellite missions considered. The Sentinel-2 mission consists of a constellation of two satellites; the first was operational since October 2015. The Landsat programme provides images since 1972.

Sentinel-2 is selected in this research. Additional information on the Copernicus programme is provided in appendix A.

A disadvantage of the Sentinel-2 imagery compared to images from the Landsat satellites is the inferior algorithm of detecting clouds. Landsat records thermal values which means that clouds can be identified more easily and cloud shadows can also be filtered; this is not possible with Sentinel-2 imagery (Hagenaars, 2017).

Tidal bias

Tidal bias is one of the issues to consider with earth observing satellites. Earth observing satellites are placed in a sun-synchronous orbit so that images always have consistent lighting conditions. Images at a certain location are always made at the same time of day.

As the tidal amplitude and phase depend on the earth-moon-sun geometry there is always a relationship between the tidal constituents (Eleveld et al., 2014). With images taken by a sun-synchronous satellite at a regular interval, not all tidal stages are represented. High or low water levels may be better described by the images. Eleveld et al. (2014) found that this bias is largely location-dependent.

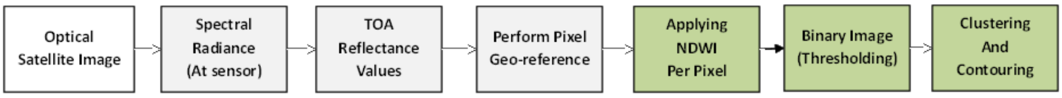

Figure 2.5: Image procession steps for the extraction of SDS. The steps depicted in gray are referred to as raw image processing and are required for feature recognition of any kind. The highlighted steps are specific for the method described by Hagenaars (2017) to extract shoreline features.

2.4.2 Google Earth Engine

Until recently, analysing remote sensing data required considerable technical expertise and effort (Gorelick et al., 2017). Processing geospatial data sets was associated with IT pains. This meant that taking full advantage of these resources was not rendered available to many researchers. However, with the launch of Google Earth Engine (GEE), Google's planetary-scale platform for Earth science data and analysis, it has become easy to process large geospatial data sets. The cloud-based platform combines a large repository of publicly available geospatial data sets with a high-performance parallel computing service to analyse these data sets.

2.5 Automated shoreline detection

An application of satellite imagery in the Coastal Engineering field is monitoring shoreline evolution. Luijendijk et al. (2018) applied an automated shoreline detection method to the entire Landsat archive to create a global-scale data set of annual shoreline positions called the Shoreline Monitor. Analysis of the Satellite Derived Shorelines (SDSs) indicates where the world's beaches are eroding and accreting and where they are stable. This provides useful insights for coastal managers, scientists and engineers.

2.5.1 Shoreline detection method

The basis for the Shoreline Monitor is a 33-year-collection of satellite images. Annual composites were used for the analysis, the images were analysed on the GEE platform. The method for extracting shoreline features (Hagenaars, 2017) consists of a number of image processing steps, as can be seen in figure 2.5. Three steps are highlighted for shoreline detection:

1. Applying $NDWI$ per pixel
2. Binary image (thresholding)
3. Clustering and contouring

The Normalised Difference Water Index ($NDWI$) is an enhancement technique for monitoring water content. It is based on the different reflectance properties of water and land. By applying a thresholding algorithm on the $NDWI$, it is possible to classify pixels as water or non-water. The third step (clustering and contouring) is applied to the binary image to extract the SDS: The shoreline is the defined as the interface between water and non-water pixels. The SDS has a sawtooth shape, as the boundary follows the shape of the pixels. A smoothing algorithm is used to obtain a smooth shoreline. A short guide on extracting shoreline features from satellite imagery based on the method described by Hagenaars (2017) is included in appendix C. The main concepts are discussed hereafter.

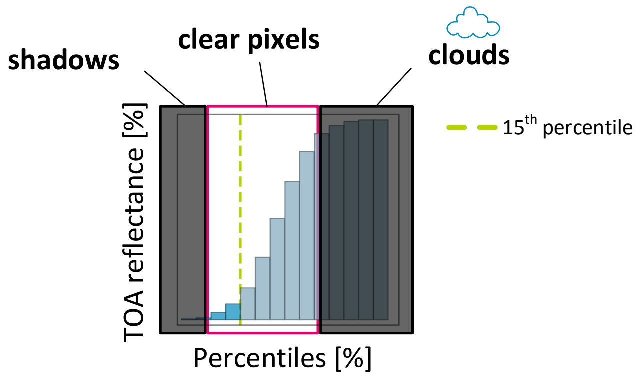

Figure 2.6: Cumulative distribution of TOA reflectance values of one band and one pixel based on all image in the image collection. Pixels with low TOA reflectance values are associated with shadows; high values with clouds. The reduced pixel value is defined as the 15th percentile value. Adopted from Hagenaars et al. (2018)

Image compositing

Compositing is an image processing technique that is often used in optical satellite imagery to reduce the impact of cloud cover on the image quality Hagenaars et al. (2018); Luijendijk et al. (2018). This is achieved by reducing a collection of satellite images to a single image so that impurities such as clouds are filtered out. The pixel value of the composite image is based on all available pixels for that location.

The Shoreline Monitor, for example, uses annual composites based on all images from a specific year. The top of atmosphere (TOA) reflectance value per band and per pixel for the reduced image is calculated by taking the 15th percentile value of the TOA reflectance values of all the underlying images. This is illustrated in figure 2.6. Other reduction techniques such as the mean are also common.

Classification of water and non-water pixels

The main image processing step is the classification of water and non-water pixels. Classification means that every pixel is labelled as a land pixel or as a water pixel. There are two techniques for differentiating land and water pixels: (1) unsupervised pixel thresholding and (2) supervised machine learning. This research adopts the method by Hagenaars (2017) which is based on pixel thresholding.

(1) The pixel thresholding technique is an index-based approach that can be applied in a user-independent way. The *NDWI* (McFeeters, 1996) is a widely used index to discriminate between water and land features:

$$NDWI = \frac{\lambda_{green} - \lambda_{NIR}}{\lambda_{green} + \lambda_{NIR}} \tag{2.4}$$

where λ_{green} and λ_{NIR} are the pixel intensities in the green band (0.54 to 0.58 μm) and the short-wave infrared band (0.78 to 0.88 μm).

Light in the near-infrared (NIR) wavelengths is absorbed in water, whereas it is reflected on the earth's surface. Figure 2.7 shows how this classification works for a Sentinel-2 scene of the Sand Motor mega-nourishment in the Netherlands. Each pixel is assigned an *NDWI* value (between -1.0 and 1.0); the left figure shows the resulting grayscale image. The middle figure is a histogram of all the *NDWI* values. The threshold determines which pixels are associated with water and which pixels are

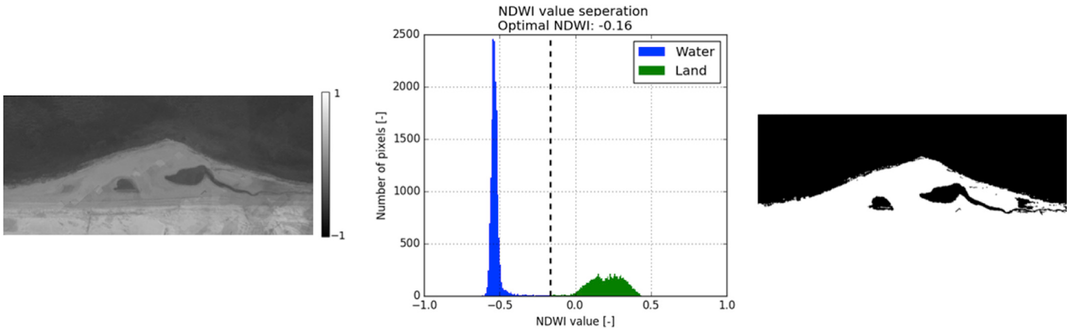

Figure 2.7: *NDWI* greyscale image (left), *NDWI* histogram (middle) and resulting binary image (right). Adopted from Hagenaars et al. (2018).

associated with land. This example uses the Normalised Difference Water Index, but there are many more indices available that can be applied similarly (see appendix C).

(2) Machine learning relies on recognizing patterns in an abundance of data. Classification using machine learning uses labelled data, or 'training data', to find patterns, rather than using a predefined algorithm. Because training data are required, machine learning classifiers are referred to as supervised. This implies that machine learning algorithms are user-dependent (Hagenaars, 2017; Sagar et al., 2017). They are computationally more demanding, but are better able to distinguish land and water.

2.5.2 Accuracy of the SDS position

Hagenaars et al. (2018) checked the accuracy of SDS position versus the in-situ shoreline for yearly composites. Six drivers of inaccuracy have been identified:

1. Cloud cover
2. Waves (surface roughness and foam)
3. Soil moisture and grain size
4. Sensor corrections
5. Georeferencing
6. Image pixel resolution

In a benchmark case, with these inaccuracies minimised, Hagenaars et al. (2018) showed that the SDS has an accuracy of 1 m. This is well within the image pixel resolution (30 m for Landsat images). In a real-life case, cloud cover and waves cause a significant seaward bias. Cloud cover results in deviations of the SDS position in the order of 200 m; waves result in deviations of about 40 m.

3 Research methods

As stated in the research outline, the objective of this research is (1) to explore the possibility of deriving the intertidal beach slope from satellite imagery and (2) to use this to estimate the grain size of the beach sediments. This chapter elaborates on the two-step approach. For both research objectives multiple methods are evaluated. First, an overview is given of the methodology and the assumptions made. 3.2 focusses on three methods (FAST, Sagar & Onrust) related to the first research objective. 3.3 focusses on two methods (equilibrium beach profile & beach face relation) related to the second research objective.

3.1 Overview methodology and assumptions

This research combines existing methods from literature with new ideas to enable the classification of beach sediments from satellite imagery. The basis is a two-step approach, following the two main research objectives (see figure 3.1). The first step is to derive the intertidal beach slope from satellite imagery. The second step is to estimate the grain size from the satellite derived intertidal beach slopes. Both steps are discussed separately in this chapter: the method for the first step is discussed in section 3.2, section 3.3 discusses the second step.

For the first step, deriving the intertidal beach slope from satellite imagery, three methods are selected: the FAST method (FAST, 2017), the Sagar method (Sagar et al., 2017), and the Onrust method (newly developed).

The second step continues from the intertidal beach slope to estimate the sediment class. Two methods are studied, based on equilibrium beach profiles and beach face slope relations respectively.

A transect-based approach is adopted: intertidal beach slopes and grain sizes are calculated per cross-shore transect. The methods are compared and validated using data from three study sites. These sites are introduced in section 3.4.

3.1.1 Variability and seasonality

Deriving the slope of the intertidal beach requires combining multiple satellite images to get an understanding of the shoreline position in each phase of the tidal cycle. The number of images in a collection of images is always a compromise between accuracy of the method and the variability of the in-situ beach. More data will make the methods more robust, but inevitably means that the image collection spans a longer timeseries.

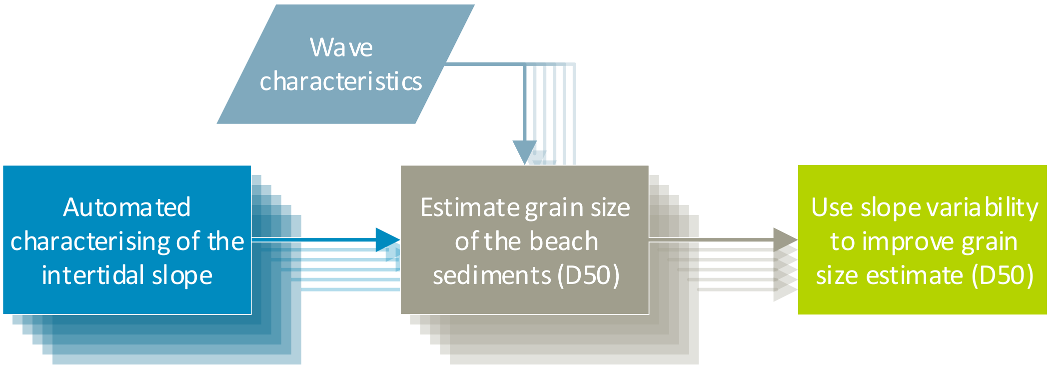

Figure 3.1: The research methodology consists of three steps. The intertidal beach slope and grain size are calculated for different time periods in order to distract the variability. This variability is used to make the grain size estimate more robust.

Different time series result in different intertidal beach slopes due to the natural variability of the environmental conditions. Where the beach face has a short response time, the grain size is generally much more constant (not always as is demonstrated by Bujan et al. (2019)). This means that different time series of satellite images result in different beach slopes, but should result in a similar grain size. Combining the different time series is used in this research to improve the estimate of the grain sizes, see figure 3.1.

3.1.2 Satellite images: Sentinel-2

The analysis of satellite images is done on the Google Earth Engine (GEE) platform. Sentinel-2 images with a cloudcover percentage less than 20 % are used in this thesis. Visible wavelengths are blocked by clouds, so they make it impossible to identify land and water correctly. This significantly impacts the accuracy of Satellite Derived Shorelines (Hagenaars et al., 2018).

3.1.3 Unsupervised water classification using *NDWI*

The analysis of satellite images includes a water classification step. As stated in the previous chapter, there are multiple solutions for detecting water. These solutions can be roughly divided as index classification and machine learning classification.

In this research, preference is given to the use of an unsupervised classification algorithm instead of a machine learning classifier. The Normalised Difference Water Index (*NDWI*) is selected because it has proven to be a robust index in different environments (Murray et al., 2012; Sagar et al., 2017).

3.2 Characterisation of intertidal beach slopes

This section provides the methodology for the first research objective:

To derive the intertidal beach slope from optical satellite imagery

First, an analysis of the field observations. Next, three methods for deriving the slope of the intertidal beach are investigated. These methods are based on literature but are adjusted for this graduation work.

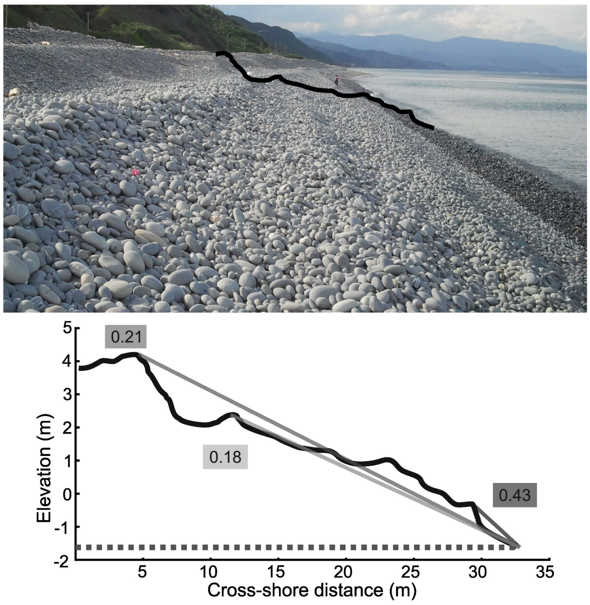

Figure 3.2: Photo of a steep cobble beach in Nantian, Taiwan. The beach profile along a cross-shore transect is indicated by the black line. The beach face slopes are determined for different parts of the beach profile with different return periods of the wave run-up (hours, weeks and years). This example illustrates the complexity of selecting a single slope to characterise the beach face (Bujan et al., 2019).

Method FAST is discussed in 3.2.2
Method Sagar is discussed in 3.2.3
Method Onrust is discussed in 3.2.4

The intertidal beach slopes are computed per transect. A 1D gaussian filter is applied in the alongshore to smooth sudden variations of the slope. The various filtering steps are discussed in 3.2.5.

3.2.1 Determining the slope of the intertidal beach from field observations

In order to compare the satellite derived slopes to intertidal beach slopes from field measurements, the latter must first be determined. The slope of the intertidal beach, or beach face slope, is rarely measured in the field, so it must be derived from the observed beach profiles. However, "The region over which a proper beach face slope should be calculated is poorly defined" (Holland & Holman, 1996).

The slope of the intertidal beach can be determined by taking a least squares fit from the observed beach profiles. A linear model is fitted to the part of the observed profile that comprises the intertidal zone. However, the extend of the intertidal zone varies over time, so this calculation isn't straightforward.

The intertidal zone is defined as *the area that is above water level at low tide and underwater at high tide.* The low intertidal zone is virtually always underwater except during the lowest of spring tides. The high intertidal zone is only submerged during severe storms, or when high waves cause high wave run-up. In conclusion this means that this definition results in a different intertidal zone depending on the conditions. Figure 3.2 clearly shows that the slope of the beach face is very sensitive to the estimate of the extend of the intertidal zone.

It may be clear that the region that demarcates the intertidal zone is poorly defined. In addition, it is unclear which part of the intertidal zone is observed by the satellite imagery. Due to the tidal bias (read chapter 2), this varies from place to place.

This problem is solved by optimising the reach of the intertidal zone for every location. Two arbitrary points are chosen to delineate its extent based on the Root Mean Square Error (*RMSE*) with the satellite derived slopes. Subsequently, the observed slopes are determined by taking the least squares fit of a linear model to the measured beach profiles. When multiple surveys are available within the analysis period, the weighted average using the number of images as weights is computed.

3.2.2 Method FAST: using time ensemble averaging

Foreshore Assessment using Space Technology (FAST) is a European research project aimed at supporting cost-effective, nature-based shoreline protection against flooding and erosion. Their MI-Safe viewer (FAST, 2017) includes an elevation data set compiled of GEBCO and SRTM data. Intertidal regions are often missing in these data sets and the spatial and vertical resolutions are low. FAST (2017) uses remote sensing data to fill this gap.

The scheme in figure 3.3 shows the different steps of the FAST method. The four steps are indicated below. Identification of surface water allows composite, Time Ensemble Averaged (TEA) images of the probability of inundation, to be built up in tidal coastal zones.

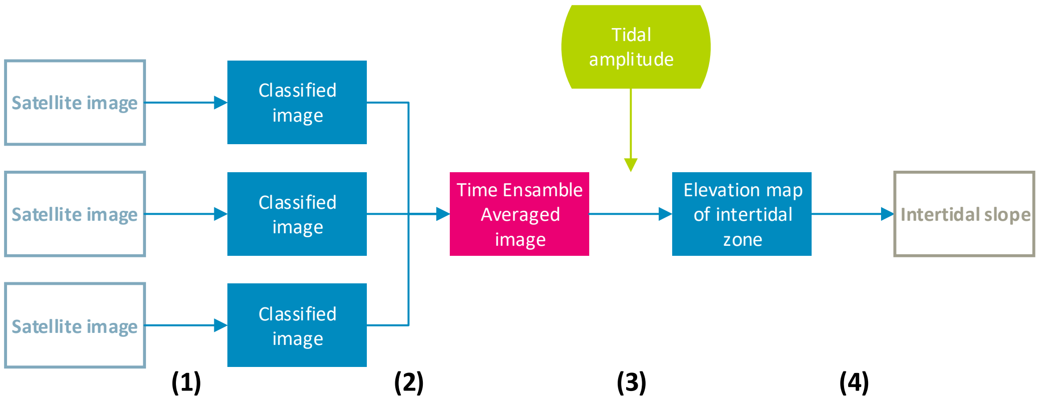

Figure 3.3: Schematic overview of the FAST method. The method consists of four steps indicated by the numbers 1, 2, 3, and 4.

Step 1: Classification of water/land pixels
An unsupervised classifier, the *NDWI*, is applied to every image to discriminate between water and land. Next, the Otsu thresholding algorithm is used to create a binary (water/land) image. Every pixel in this image has the value 0 (water) or 1 (land). This holds good for every image in the collection.

Step 2: Compositing by averaging in time
The image collection of binary (water/land) images is reduced to a single image by applying an averaging compositing technique. This results in a so-called TEA image, where every pixel has a value between 0.0 and 1.0. Figure 3.4 shows an example of a TEA image.

The pixel value in the TEA image signifies the 'probability' of water occurrence; a pixel in the TEA image can only have a value of 1.0 if water was detected here in every image of the collection. The same holds for land pixels. Thus, pixels that are

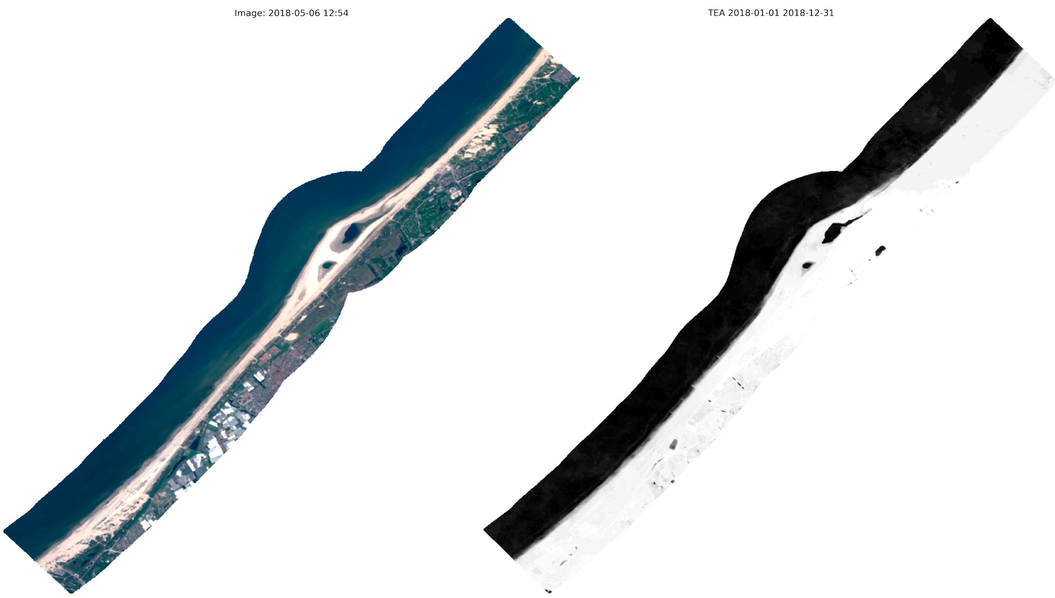

(a) Visible image (b) TEA image

Figure 3.4: Example of a Time Ensemble Averaged image, generated from the Sentinel-2 images (2018) of the Delfland coast. The shade of gray indicates the probability of water, where black indicates a probability of 1.0 and white a probability of 0.0. Around the shoreline, a clear zone with intermediate values can be observed. A shadow band near the shoreline can also be seen, where wave foam and clouds are often misinterpreted as land. The true-colour image is one of the images used to create the TEA image.

classified as land in some images and water in other images have an intermediate value in the TEA image.

Step 3: Convert TEA image to intertidal elevation map

Pixels with an elevation above the highest astronomical tide (HAT) are land in all of the individual images and consequently have a value of 0.0 in the TEA image. Pixels with an elevation below the lowest astronomical tide (LAT) are classified as water in all images and have a pixel value of 1.0. When the tidal amplitude is known, the TEA image can be converted to an elevation map of the intertidal zone. For intermediate pixel values, a linear gradient is assumed. The elevation map is only valid in the intertidal zone as elevations above the HAT (or below the LAT) are white (or black) in the TEA image.

Step 4: Fitting the intertidal slope

The intertidal elevation map is mapped to a cross-shore transect based on the location. The pixel values are transferred to the transect, as can be seen in figure 3.5.

No elevations above the HAT or below the LAT are inferred because the elevation is based on the probability of water occurrence. The transition between adjacent pixels with different elevation values, results in a stepped shape of the plot.
Disturbances such as clouds and wave foam cause noise in the cross-shore distance versus elevation plot. Consequently, the shape is often not simply linear.

In order to retrieve the intertidal beach slope, a stepped linear model is fitted to the data using the least squares method. This stepped linear model has two constant tails and a linear part in the area around the shoreline. Figure 3.5 shows an example.

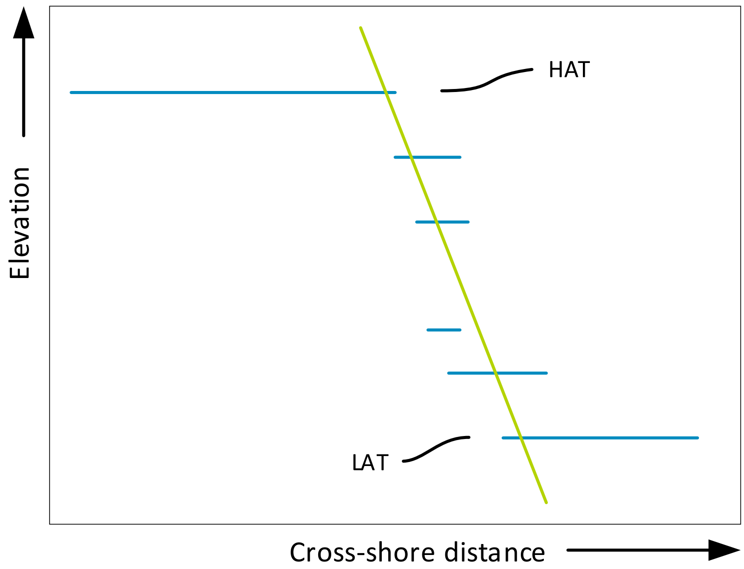

Figure 3.5: Example of a fitted slope using the FAST method. The datapoints are obtained by mapping a cross-shore transect to the intertidal elevation map. The elevation decreases to the right, which is further offshore. A slope is fitted to the data using a least squares algorithm.

3.2.3 Method Sagar: composite images per tidal level

The Sagar method is based on work by Sagar et al. (2017). Sagar et al. (2017) applied an unsupervised classifying algorithm to composite images from the entire Landsat archives to find the extend and topography of the Australian coastline.

The scheme in figure 3.6 shows the different steps of the Sagar method. The water level in each image is determined, subsequently the images are grouped on the water level. A composite image is created from each group in order to improve image quality (clouds and wave foam are filtered out). The elevation of the shoreline extracted from these composites is assumed to be the average elevation of the individual images. Combining the data from the different groups allows for the derivation of the slope of the intertidal beach.

Step 1: Image grouping per water level
The water level is determined for every image in the image collection. The images are then grouped according to their water level elevation. Sagar et al. (2017) used 9 groups based on the tidal range ([0 to 10] %, [10 to 20] % ... [80 to 100] % of the tidal range), but any number of groups may be chosen. With fewer image groups, the uncertainty in the elevation increases. With more image groups, a larger number of images is required. Here, 5 groups are used.

Step 2: Compositing per group
A composite image is made for every group. The water level in the composite image is assumed to be the average of the water level of the images in the group. Due to the compositing approach, it is impossible to say anything about the physical water level as this may differ per pixel, or even per band in each pixel.

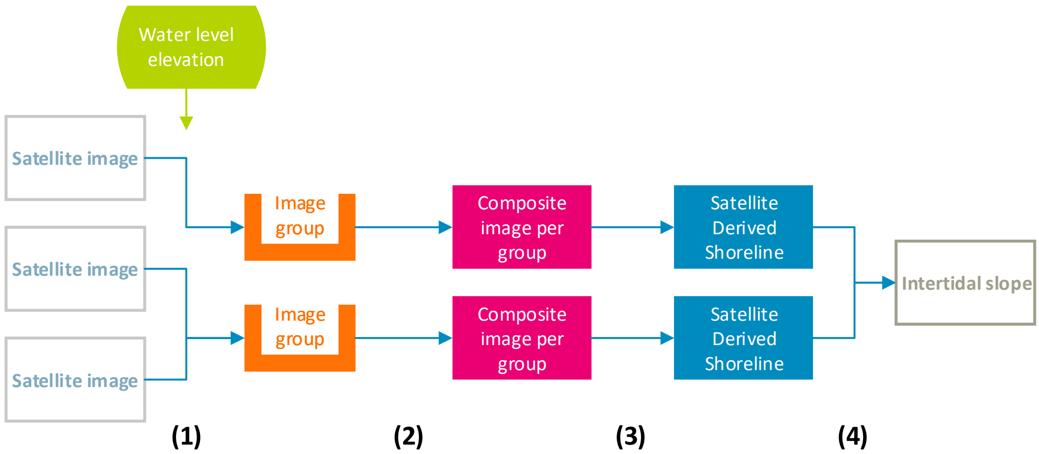

Figure 3.6: Schematic overview of the Sagar method. The method consists of four steps indicated by the numbers 1, 2, 3, and 4.

Step 3: Shoreline detection

The Satellite Derived Shoreline (SDS) is determined using the shoreline detection algorithm described by Hagenaars et al. (2018). Section 2.5 describes the intermediate steps for the automated shoreline detection. The shoreline detection algorithm uses the *NDWI* to differentiate between water and non-water pixels. A shoreline is retrieved for every image composite.

Step 4: Fitting the intertidal slope

The intersections between the obtained shorelines and a user-defined cross-shore transect are called waterline points. Every SDS results in one waterline point; if multiple intersections are found per transect, the most offshore point is selected. Figure 3.7 shows an example of a cloud of waterline points. The elevation is plotted against the cross-shore distance. A linear profile is fitted to the data points using least squares to find an intertidal beach slope.

3.2.4 Method Onrust: shoreline detection based on single images

The FAST and Sagar method use compositing techniques for the derivation of the slope of the intertidal beach. Despite the advantages of compositing (i.e. filtering clouds from images), this means that information on the variability within the time sequence is lost. A method based on single images contains all the information so has the potential to map a lot of the variability of the intertidal beach slope. This is interesting because the beach face is known to be very dynamic.

Another disadvantage of compositing in the context of this research is the large number of images required. The FAST and Sagar method need a minimum of 17 and 50 images, respectively. As a result, time sequences for the derivation of the slope of the intertidal beach are very long.

The Onrust method is developed to overcome these disadvantages. The Onrust method is a single-image method with the purpose to capture more of the variability. The methodology resembles the Sagar method as it uses an algorithm based on shoreline detection, but does not need the image grouping step. Instead a manual filtering step (0) is added to filter out inaccuracies such as clouds, see figure 3.8.

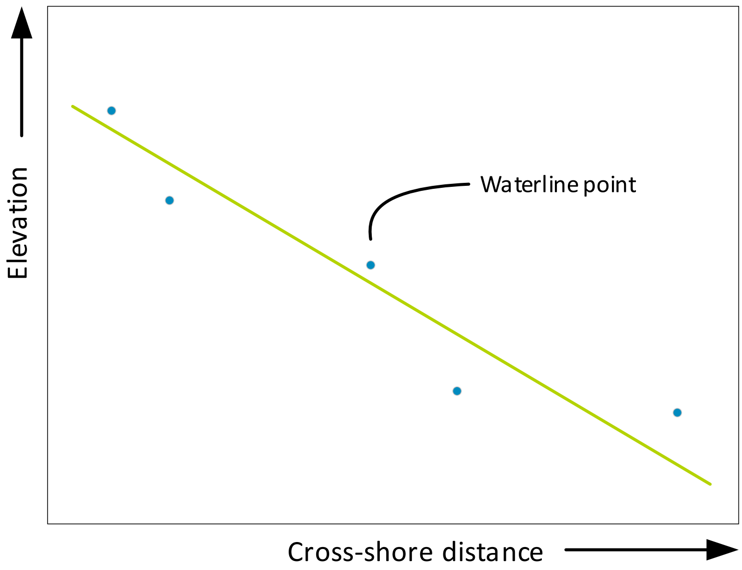

Figure 3.7: Example of a fitted slope using the Sagar method. The datapoints are obtained by finding the intersection between a cross-shore transect and the Satellite Derived Shorelines from the composite images. A slope is fitted to the data using a least squares algorithm.

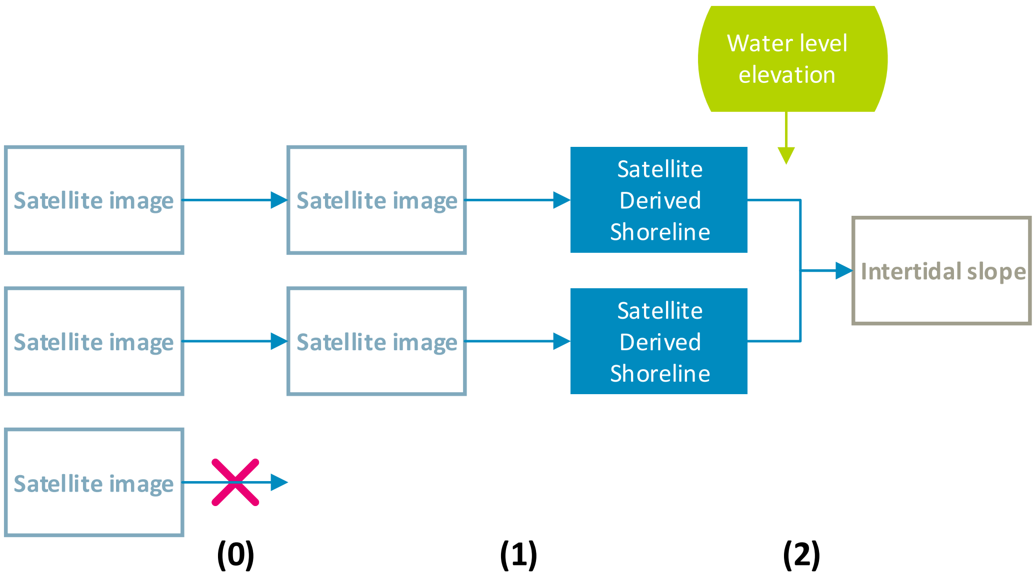

Figure 3.8: Schematic overview of the Onrust method. The method consists of a pre-processing step (0) and two model steps indicated by the numbers 1, and 2.

Step 0: Manual filtering of images

Unlike the other methods, single images are used instead of composites. This implies that there are unwanted features in the images that disturb the classification of land and water using the *NDWI*. Therefore, an additional pre-processing step is added: the individual images are assessed and removed from the image collection if any source of inaccuracy is spotted. Cloudy images are first filtered on image metadata. Attention is paid to three sources of inaccuracy, see figure 3.9:

- Clouds
- Cloud shadows
- Wave foam

Step 1: Shoreline detection

The SDS is determined using the shoreline detection algorithm described by Hagenaars et al. (2018). Section 2.5 describes the intermediate steps for the automated shoreline detection. The shoreline detection algorithm uses the *NDWI* to differentiate between water and non-water pixels. A shoreline is retrieved for every image.

Step 2: Fitting the intertidal beach slope

The intersections between the obtained shorelines and a user-defined cross-shore transect are called waterline points. Every SDS results in one waterline point; if multiple intersections (of the shoreline and the transect) are found, the most offshore point is selected.

The water level at each transect at the moment the image was captured is determined. This is the elevation of the waterline point. Figure 3.8 shows an example of a cloud of waterline points. The elevation is plotted against the cross-shore distance.

As the Onrust method uses single images instead of composites, the SDS positions are polluted by the presence of clouds, shadows and wave foam. Therefore, it is unavoidable that there are outliers in the cloud of waterline points. This means that the intertidal beach slope cannot simply be determined by applying a least squares fit of a linear profile.

The least squares regression model is highly sensitive to outliers, so a robust regression model is preferred. Rousseeuw & van Driessen (2006) suggest the Least Trimmed Squares (LTS) regression model as an alternative of the least squares regression model in the presence of outliers. LTS regression is based on linear least squares calculated over a subset of the data points. Figure 3.10 shows an example of a intertidal beach slope fitted to the data points using LTS.

3.2.5 Filtering outliers and unreliable slopes

With the large amounts of data related to analysing satellite imagery, it is important to carefully filter all data. Inaccuracies are inevitable and result in outliers in the data. Several filtering steps are incorporated to filter out inaccuracies:

- First, a quality band is provided with the Sentinel-2 1C data products. This band contain metadata about the image quality, such as the presence of clouds. This metadata is used to mask clouds in the satellite images. Not all clouds are detected by the cloud detection algorithm.

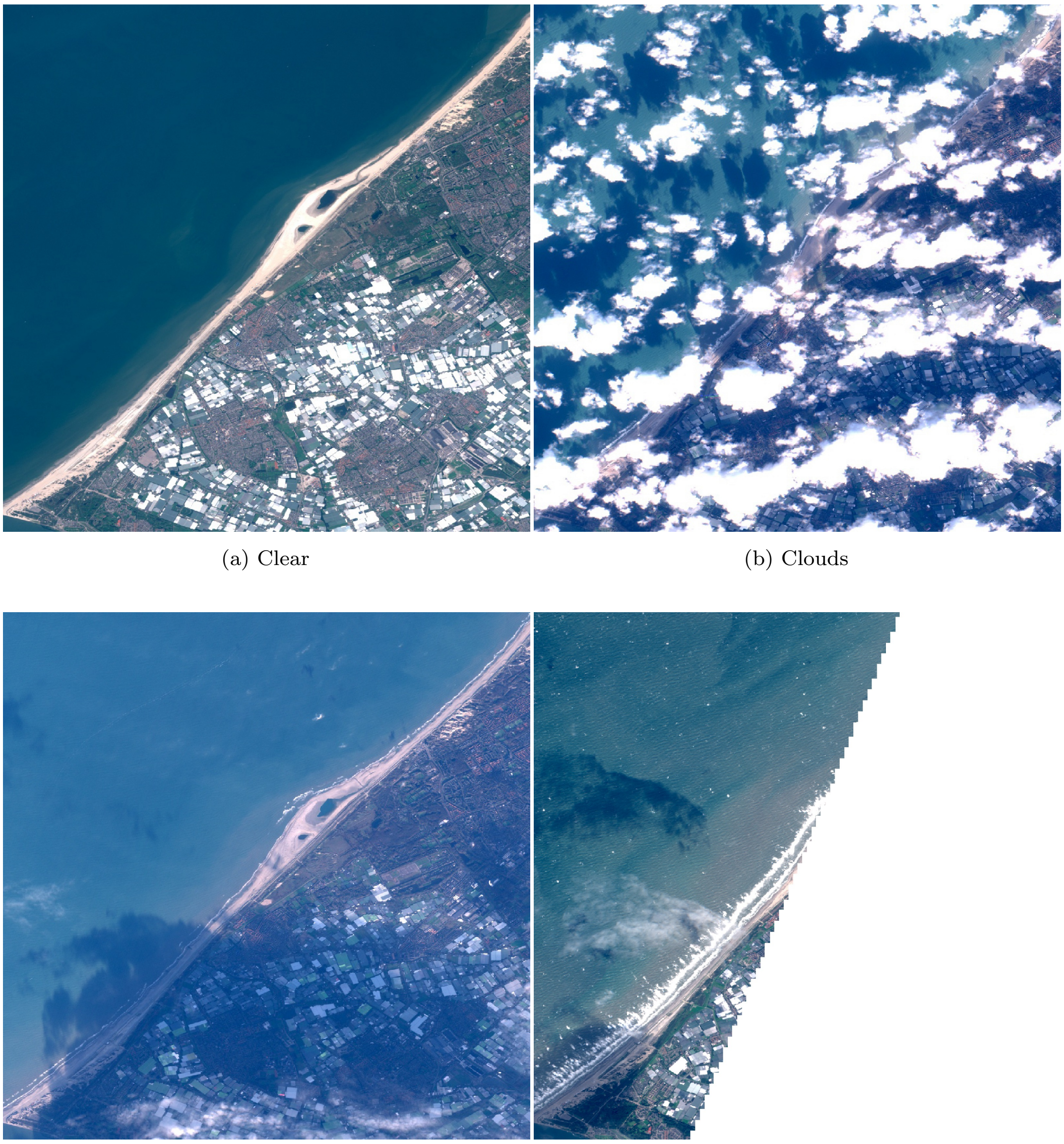

(a) Clear (b) Clouds

(c) Shadow (d) Waves

Figure 3.9: Images are assessed based on visual inspection. This figure shows four example images from the Delfland coast. (a) shows a clear image, (b) is polluted with clouds, (c) is polluted with cloud shadows, and (d) is polluted with waves.

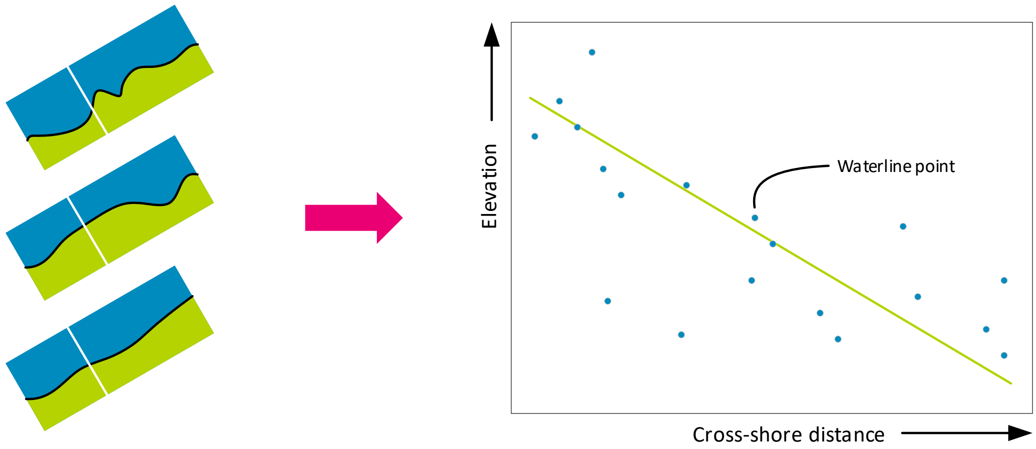

Figure 3.10: Example of a fitted slope using the Onrust method. The datapoints are obtained in a similar way to the Sagar method. The difference is that Satellite Derived Shorelines are derived from individual images. The slope is fitted to the data using the Least Trimmed Squares algorithm to account for outliers.

- Second, a 1D filter is applied to the cross-shore positions of the SDS in the Sagar and Onrust method. SDSs with a cross-shore position further than three times the standard deviation are labelled as 'outlier'.
- The Sagar and Onrust method use a regression technique to fit a linear model through the data points. The LTS algorithm, a robust regression method, is used for this. Robust means that it, unlike the least squares algorithm, performs well in the presence of 'outliers' (Rousseeuw & van Driessen, 2006). Data points with large residuals are labelled as 'outliers' and the linear fit is based on a subset of the data points.
- Finally, the resulting intertidal beach slopes are filtered. The regression method (LTS in the case of the Sagar and Onrust method and least squares in the case of the FAST method) also computes the standard error of the gradient. Slopes with an error larger than 0.05 are filtered out. In addition, slopes based on less than 5 data points are removed and negative slopes are removed.

The FAST and Sagar method use a compositing technique to improve image quality. The Onrust method is based on single images. This implies that there are inaccuracies that cause outliers. A manual screening step is added to the method.

3.3 Estimating the grain size of the beach

This section provides the methodology for the second research objective:

To determine the sediment size from satellite derived intertidal beach slopes

Two methods are investigated: (1) based on equilibrium beach profiles and (2) based on beach face slope relations. Both methods take the intertidal beach slope as input parameter to calculate the median sediment grain size ($d50$). Even though the intertidal beach and beach face relate to slightly different sections of the beach, their slopes are assumed identical. This assumption seems justifiable because these sections overlap almost entirely (they are often considered synonymous).

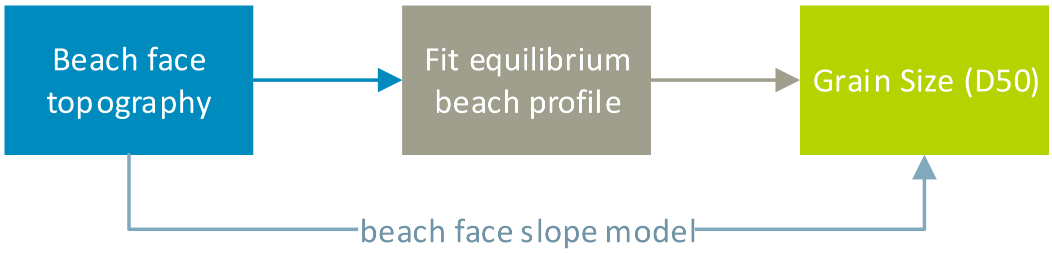

Figure 3.11: Two approaches are considered for deriving the median grain size from the beach face topography: (top) equilibrium beach profile approach and (bottom) beach face relation approach.

3.3.1 Equilibrium beach profile method

Most equilibrium beach profile models include the intertidal zone, and thereby these models can potentially relate the intertidal beach slope to the grain size. Empirical constants in descriptive models, such as the Bodge's model (Bodge, 1992; Komar & McDougal, 1994) or Lee's model (Lee, 1994), limit the applicability of these models to a description of the cross-shore shape. The Bruun model developed by Bruun and Dean (Bruun, 1954; Dean, 1977) or the 2-Step Equilibrium Beach Profile model (Bernabeu et al., 2003) for example, have clear physical interpretations of the parameters. Consequently, these models can be applied prognostically. Although there are many more models available, this research is limited to these two. Description of the Bruun model and the 2-Step Equilibrium Beach Profile model are given below.

The basis of the approach using equilibrium beach profiles are the waterline points. These points along a cross-shore transect describe the position of the shoreline at a certain elevation and in doing so describe the shape of the profile in the intertidal zone. Fitting the equilibrium beach profile models to the waterline points makes it possible to determine the model parameters. As the model parameters in the applied models have clear physical meaning they can be described. This makes it possible to estimate the grain size of the sediment in the intertidal zone.

- Bruun model
- 2-Step equilibrium beach profile

3.3.2 Beach face slope relations method

In order to gain a better understanding of the beach system and the beach face in particular, beach face slope relations have been used. These equations relate the beach face slope to, among other things, the grain size. Focus is placed on the relations by Bujan et al. (2019); McFall (2019).

3.4 Study sites

Satellite derived intertidal beach slopes and sediment sizes are compared to data from the field. Three study sites are considered in this research: Delfland coast, Netherlands; Duck coast, USA; and Hasaki coast, Japan. Figure 3.12 shows the locations of the study sites. Beach profiles and grain size data are collected regularly at these sites.

The field sites are distinctively different in terms of sediment characteristics, beach

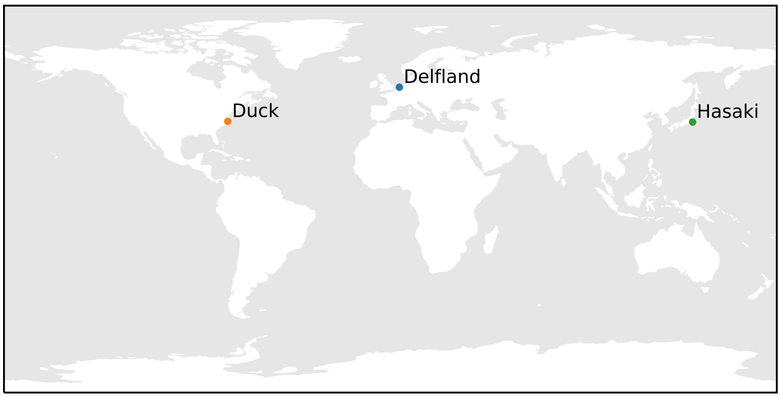

Figure 3.12: Map of study site locations

Location	Grain size $[\mu m]$	Beach face slope $[-]$	Tidal range $[m]$
Delfland (NLD)	$250 - 300$	0.02 (1 : 50)	± 2.1
Duck (USA)	600	0.1 (1 : 10)	± 1.2
Hasaki (JPN)	180	0.03 (1 : 30)	± 1.0

Table 3.1: Characterising properties of the beach at the three study sites.

slope and wave climate. The Delfland coast is a morphodynamically dynamic region due to the presence of the Sand Motor mega-nourishment. Sediments are fine to medium sands. The Duck site has a very notable sorting of sediments with course sands in the intertidal zone. The Hasaki coast is composed of fine sands. Table 3.1 gives the characteristic grain size and tidal range for each of the study sites (Vos et al., 2019, copied from).

Besides the three validation sides, the methods are also applied to the Ebro Delta coast in Spain. This site is characterised by a micro-tidal range ($\mathcal{O}$ 0.25 m) and an alongshore variation in the grain size. The idea of this case study is to check how well the models perform in locations with a small intertidal zone. This case study is discussed in appendix F.

3.4.1 Delfland coast (The Netherlands)

The Delfland study site is located between Scheveningen and Hook of Holland on the west coast of the Netherlands. Seasonal variation of the wave climate is large with the largest waves from October to April due to storms. Water levels may be driven up to extreme heights during these tempestuous weather conditions.

The Sand Motor, also referred to as Sand Engine, was constructed here in 2011 (De Schipper et al., 2014). This mega-nourishment forms a peninsula on the Delfland coast. As sediment is distributed along the coast, severe erosion is observed at the tip of the peninsula. Figure 3.13 is an analysis from the Shoreline Monitor showing a significant retreat of the shoreline since the construction. The coastal slopes are diverging to their natural state.

JarKus is the annual coastal monitoring programme by Rijkswaterstaat. The programme carries out yearly profile measurements along the entire Dutch coast at 250 m spaced transects. There are 114 cross-shore transects at the Delfland coast;

Figure 3.13: Image from the shoreline monitor of the Sand Motor. The change of shoreline position between 2012 (after the nourishment) and 2018 is indicated in the figure by the blue and green areas. Blue means erosion of the beach; green means that there is shoreline progression.

the JarKus transect system is used in this thesis.

Water levels are measured relative to Normaal Amsterdams Peil (NAP). HAT is at NAP +1.1 m; LAT is at NAP −1.0 m.

Beach profile measurements

The Nearshore Monitoring and Modelling Project (NEMO) performs regular measurements to monitor the morphology of the Sand Motor. This data is combined with the JarKus measurements (Rijkwaterstaat et al., n.d.). Data is interpolated to the 114 cross-shore transects in the region. Observations are done by a combination of a PWC (jetski) survey system, an ATV (quad bike) with mounted RTK-DGPS and by walking a wheeled GPS (De Schipper et al., 2014). Sediment composition is measured at various locations at the nourishment site.

3.4.2 Duck beach (United States of America)

The Field Research Facility (FRF) conducts research at the Duck coast (U.S. Army Engineer Research et al., n.d.). Duck is located in the east of the US, it's beach exposed to the Atlantic Ocean. The FRF transect system includes 30 cross-shore transect which are used in this research.

Water levels are measured relative to NAVD88, the local datum level. HAT, MSL and LAT are at 0.655 m, 0.058 m and at −0.488 m, respectively.

Beach profile measurements

At the Duck coast, the profile measurements are conducted along the FRF transects. A specially designed vehicle called the Coastal Research Amphibious Buggy (CRAB) is deployed to measure the bathymetry. In addition, the Lighter Amphibious Resupply Cargo (LARC) is equipped with echosounders and an RTK-DGPS system to conduct nearshore surveys.

The FRF has several wave buoys to measure the wave climate at multiple locations. There have been extensive campaigns for measuring sediment in the past (U.S. Army Engineer Research et al., n.d.).

3.4.3 Hasaki beach (Japan)

Hasaki beach is located near Tokyo on the east coast of Japan at the Pacific Ocean. The Hazaki Oceanographical Research Station (HORS) has a 427-metres-long pier where various phenomena in the nearshore zone have been measured, including an impressive timeseries of weekly profile measurements (Hasaki Oceanographical Research Station (HORS), n.d.).

The high, the mean and the low water levels are 1.252 m, 0.651 m, and 0.196 m, respectively (based on local datum level). Large waves are mainly generated by typhoons from July to September and by strong atmospheric depressions from February to April. Grain size is relatively uniform along the beach at HORS, with a median sediment diameter of 180 μm.

Beach profile measurements

Beach profiles along the pier are obtained on a weekly basis. Measurements are done at 5 m intervals with a 3 kg lead on the pier.

4 Validation of the satellite derived intertidal beach slopes

The previous chapter describes the two-step method for estimating the grain size of beach sediments. Each step is validated separately. This chapter covers the validation of the intertidal beach slopes derived by satellite against field data from the three study sites. Each of the three methods is applied and it is shown that the FAST method performs best, but that the Onrust method can capture more variability.

4.1 Explanation error statistics

The intertidal beach slopes are derived from Sentinel-2 images using three methods (FAST, Sagar and Onrust). The slopes are computed per transect and are validated against the in-situ slope of the beach face. The derivation of an example transect at the Delfland coast is worked out in appendix D.

Although the satellite derived slopes are derived per transect, an along-the-shoreline analysis is presented here. Such an analysis gives a good overview to what extent the satellite derived slopes relate to the observed values. Two parameters to assess the capabilities of the methods are investigated:

Coverage* The previous chapter (3.2.5) describes the various filtering steps that are applied. Unreliable slopes (based on the standard regression error of the gradient) are filtered out. The coverage is the measure of available slopes. In other words, it is the percentage of transects with a reliable slope.

RMSE The Root Mean Square Error ($RMSE$) is a measure of the error: it tells how far the observed and satellite derived slopes are apart. The observed slopes are averaged based on the number of images per season as weight factor.

The coverage is a measure of the robustness of a method. A higher coverage means that the method is better able to deal with outliers. The $RMSE$ is a measure of the accuracy of a method. A lower $RMSE$ means that the method is more accurate. These two measures come hand-in-hand: stricter filtering on reliable slopes has the effect of increasing the $RMSE$.

Alongshore smoothing is applied to the satellite derived slopes. The validation of the intertidal beach slopes only assesses satellite images from 2018.

*Coverage herein refers to the availability of satellite derived slopes in the region of interest. Not to be confused with the coverage of satellite imagery.

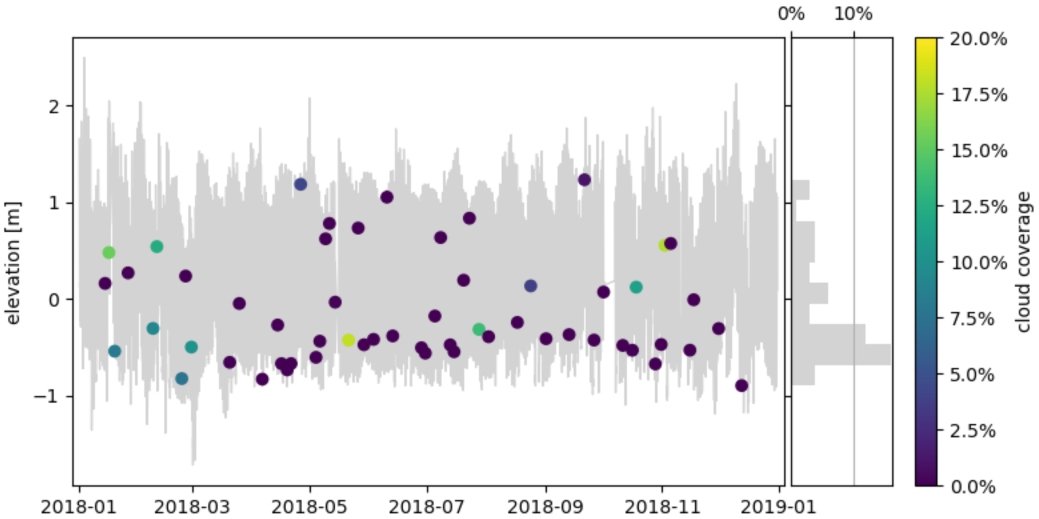

Figure 4.1: Distribution of images in time plotted against the water level. Each dot represents an image. The water levels have been recorded at the Scheveningen and Rotterdam measurement stations (Rijkwaterstaat et al., n.d.). The cloud cover limit is set at 20 % to ensure good image quality. No water level information is available between 1 October 2018 and 7 October 2018.

4.2 Case study: Delfland coast

This section describes the results of a case study of the Delfland coast in the Netherlands. A description of the study site is given in 3.4.1. The beach slopes are calculated at 114 cross-shore transects along the 17 km long coast between Scheveningen and Hook of Holland. The satellite derived slopes are compared to slopes derived from field observations. The data set (Rijkwaterstaat et al., n.d.) contains measured beach profiles from multiple measuring campaigns: JarKus and NEMO data are combined.

First an analysis of the satellite images. Then, an analysis of the field observations, in which the slope is derived from the profile. Next, the intertidal beach slopes are calculated using the three methods discussed in the previous chapter. The analysis is only performed for 2018, chapter 6 shows an analysis of the Delfland coast for multiple years.

4.2.1 Analysis of the satellite images

A total of 57 satellite images from 2018 are analysed, as is shown in figure 4.2. Although images are filtered on cloud cover percentage (< 20 %), considerable cloud cover can be distinguished; also because of the inferior cloud detection algorithm. This means that features derived from these scenes, such as Satellite Derived Shorelines (SDSs), have considerable deviations in their positions.

Water level measurements by the Scheveningen and Rotterdam stations are used as elevation data. The elevation is based on the times of image acquisition. Figure 4.1 shows the distribution of images in time plotted against the water level elevation. A bias to the lower elevations can be observed. This ‘tidal bias’ is the effect of the regular phase difference between the satellite’s orbit and the tides (Eleveld et al., 2014, read also 2.4).

Figure 4.2: The 57 Sentinel-2 images of the Delfland coast in 2018. The images are only a visible representation: more 'bands' are available in the analysis. Some images do not cover the entire area of interest. That is because the Delfland coast is on the edge of a Sentinel-2 datastrip.

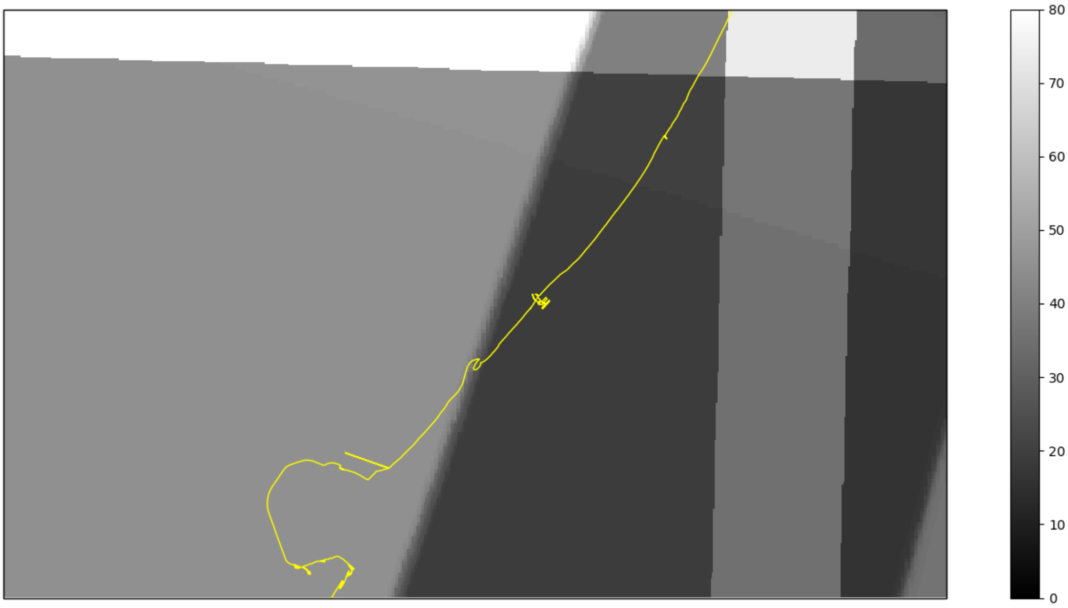

Figure 4.3: Number of images available in 2018. The images are filtered on a cloud cover percentage of 20 %. Three areas with few, average and many images can be distinguished. The band of few images marks the edge of the Sentinel-2 datastrip, the bands of many images are overlapping areas from adjacent image tiles.

Although images are acquired at a regular 5 day interval, they are not equally distributed in the year. In winter (December - March), fewer images are available due to the cloud filter. Moreover, these images have a cloud coverage that is relatively large.

Number of images

When looking more closely at figure 4.2 the fact that some images do not cover the entire region of interest stands out. This interesting effect is studied in more detail. Figure 4.3 shows a map of the Delfland coast with an overlay indicating the number of images at that location. Only satellite images from 2018 with a cloud cover percentage smaller than 20 % are included in the analysis.

Interestingly, figure 4.3 shows how the Sentinel-2 imagery system works. Imagery data from the satellites are split into 100×100 km tiles that are slightly overlapping, which explains the large number of images at the top of the figure. Moreover, there is a large diagonal zone of fewer images that covers the area. It turns out that the Delfland coast is on the edge of a Sentinel-2 datastrip. This means that many images do not cover the entire domain. At transect 9010288 for example (near Scheveningen) only 22 images are available in 2018.

As discussed before, there is a tidal bias in the satellite imagery. Since the number of images in the northeastern section of the domain differs from the southwestern section of the domain, this tidal bias is different throughout the domain. This results in an unfair comparison of the northeastern and southwestern section. Therefore, the analysis is carried out for each section separately.

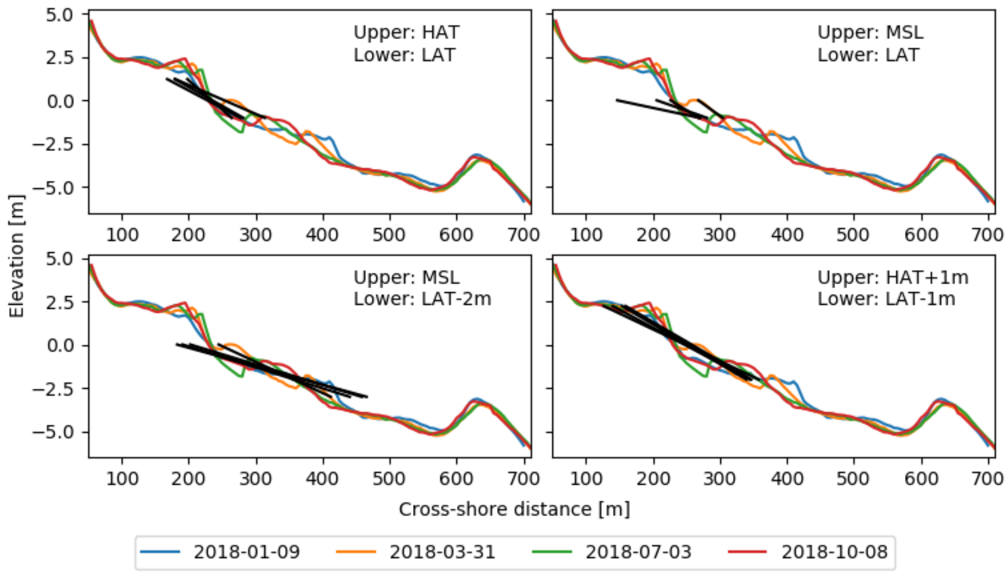

Figure 4.4: The intertidal beach slopes according to the four definitions at JarKus transect 9011094. The intertidal beach slopes are indicated in black. The profiles were obtained during four surveys in 2018. Transect 9011094 is located south of the Sand Motor.

4.2.2 Analysis of the field observations

There were four surveys in 2018: in January, March, July and October. The JarKus were executed in March; the other observations are from the NEMO project. The NEMO project does not cover the entire Delfland coast.

As discussed in chapter 3, the beach face slope is very sensitive to the boundaries of the intertidal zone. To illustrate this, the observed slopes are calculated using four different definitions. Figure 4.4 shows observed profiles along JarKus transect 9011094.

The following four definitions are used:

- HAT to LAT
- MSL to LAT
- MSL to LAT -2m
- HAT +1m to LAT -1m

The 'observed' slopes are 0.0232, 0.0184, 0.0131 and 0.0211 respectively.

The slope of the intertidal beach are derived for every transect along the Delfland coast and plotted against the alongshore position in figure 4.5. The slopes derived using the four definitions of the intertidal zone are very different. Both the steepest and the flattest slopes are observed at the tip of the Sand Motor. Due to wave focussing, the slope of the beach face is steep here; due to the presense of a sand bar, a flat slope is observed lower in the profile.

Figure 4.5 shows a large alongshore variation of the beach face slope which is the result of the construction of the Sand Motor. Just north of the Sand Motor, in the area around the lagoon entrance, the observed slopes are particularly flat. This area has an extensive intertidal zone where water enters the channel connecting the lagoon to the North Sea.

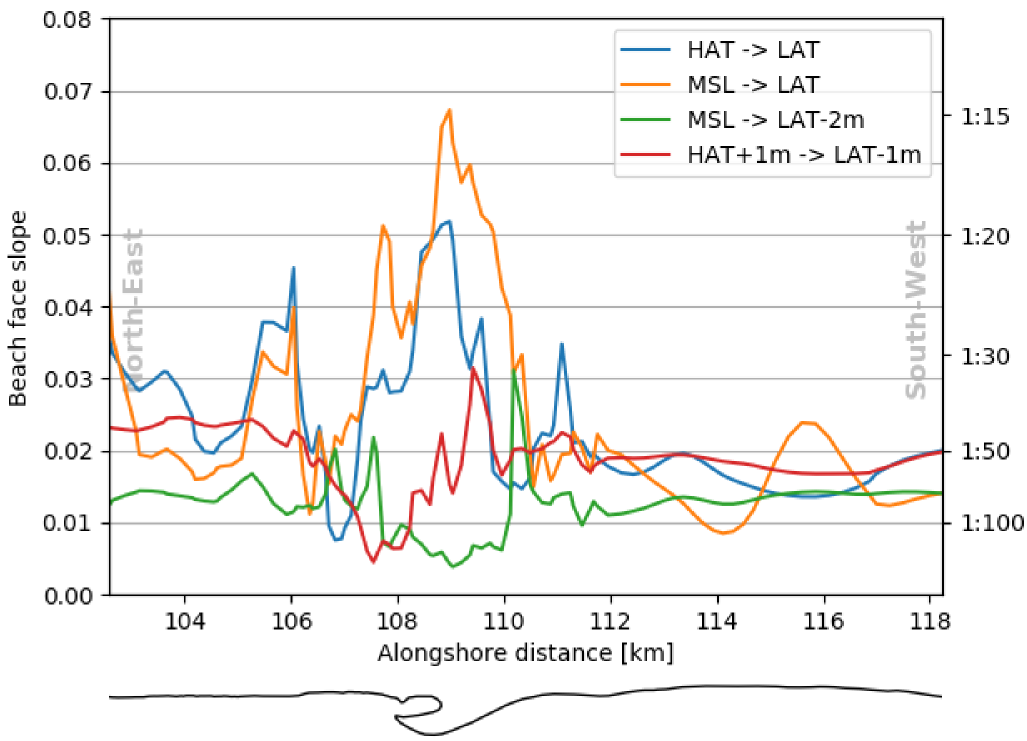

Figure 4.5: Beach face slopes observed in 2018 along the Delfland coast. Four definitions for the extent of the intertidal zone are used. A top view of the Delfland coast is shown at the bottom.

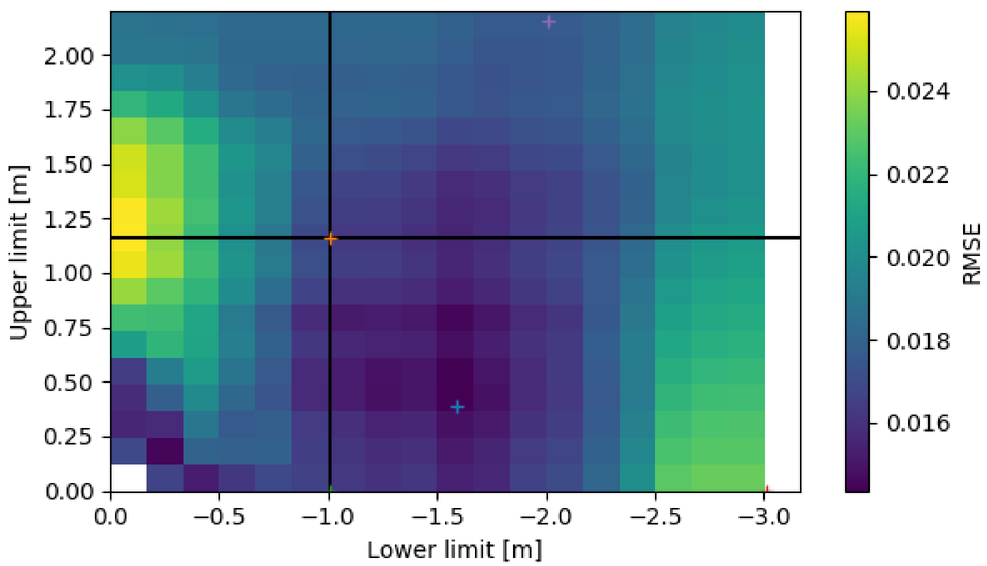

Figure 4.6: Optimising upper and lower limit of the intertidal beach. The black lines indicate the LAT and HAT. The minimum *RMSE* is found at (0.39, −1.59).

Notable is the difference between the slopes north and south of the Sand Motor (steeper in the northeast). This can be explained by the difference in sediment size. The sediment to the north is coarser, so consequently the corresponding gradient of the beach is larger.

Optimising the extent of the intertidal zone

To resolve the issue of an unclear beach face slope definition, this research optimises the extent of the intertidal zone by minimising the *RMSE*. The satellite derived slopes are computed using the methodology described in chapter 3. The 'observed' slopes of the intertidal beach are calculated for a large number of combinations of the upper and lower limit of the intertidal zone. The *RMSE* is computed for every 'definition' of the intertidal zone.

Figure 4.6 shows the *RMSE* value for all upper and lower limits. The beach slopes are derived from satellite imagery with the Onrust method. Such an optimisation is carried out for every method. The minimum error is found at (0.39, −1.59). This implies that the satellite images are focussed on the lower part of the profile. This conforms to the tidal bias that is observed at the Delfland coast.

4.2.3 Analysis of the satellite derived intertidal beach slopes

The satellite derived slopes are computed for every transect along the Delfland coast using the three methods discussed before. An alongshore overview is provided.

FAST method

The intertidal beach slopes are computed using the FAST method and plotted against the alongshore position, see figure 4.7. The observed slopes have some variability that is incidated by the shading around the blue line.

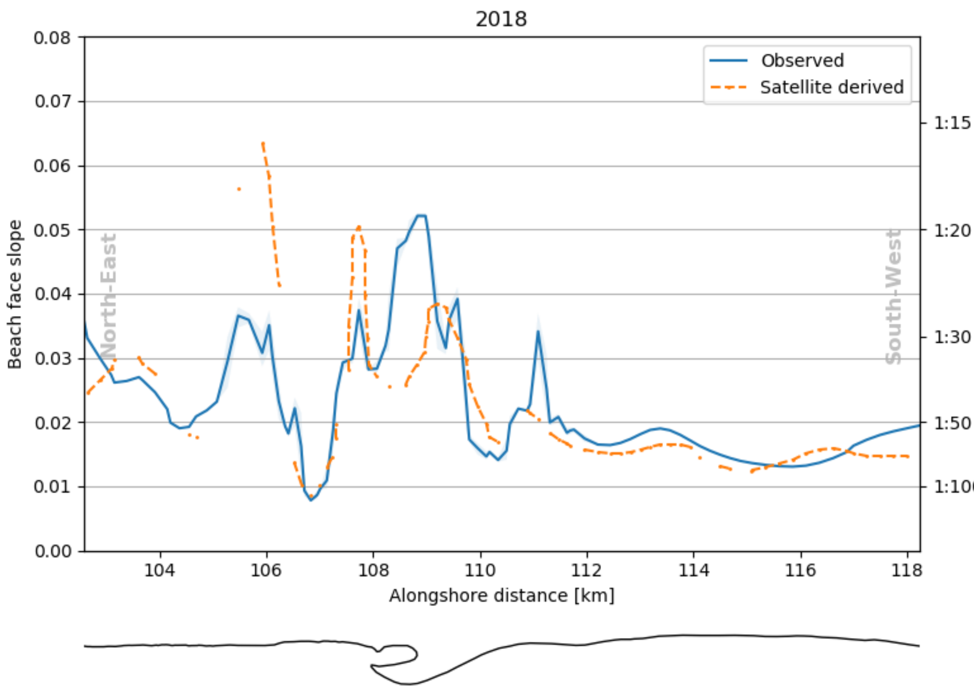

Figure 4.7: The intertidal beach slopes as observed and satellite-derived using the FAST method. The slopes are plotted against the alongshore position at the Delfland coast. The bandwidth around the observed slopes indicate the variability.

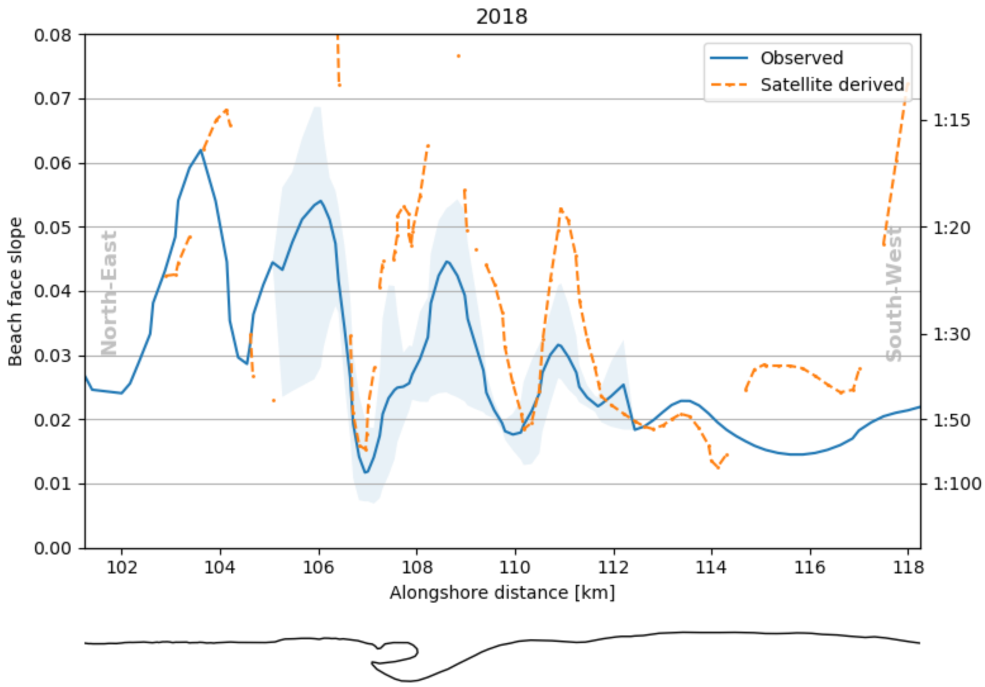

Figure 4.8: The intertidal beach slopes as observed and satellite-derived using the Sagar method. The slopes are plotted against the alongshore position at the Delfland coast. The bandwidth around the observed slopes indicate the variability.

The satellite derived slopes seem to match the observed slopes well. The peaks in the satellite derived slopes also appear in the observed slopes, except at the tip of the Sand Motor where a flatter slope is predicted. This results in a very good *RMSE* value of 0.0092.

Sagar method

The results of the Sagar method are presented in figure 4.8. The satellite derived slopes show a lot more fluctuation in space compared to the FAST method. As discussed in section D.3.2 there were errors in the composite images which led to these fluctuations.

However, the satellite derived slopes still form a good match to the observed slopes. When looking at another definition of the extent of the intertidal zone, these fluctuations are also present in the observed slopes. In the area northeast of the Sand Motor the coverage* is low; there are only a small number of images in this area.

In the southwestern section of the domain the satellite derived slopes are off. This results in a higher *RMSE*: 0.0185.

Onrust method

An alongshore overview of the satellite derived slopes using the Onrust method can be seen in figure 4.9. Like the other methods, the peaks in the observed slopes are very well represented by the slopes derived by satellite.

The *RMSE* is 0.0123, so it is in the same order of magnitude as the FAST and the

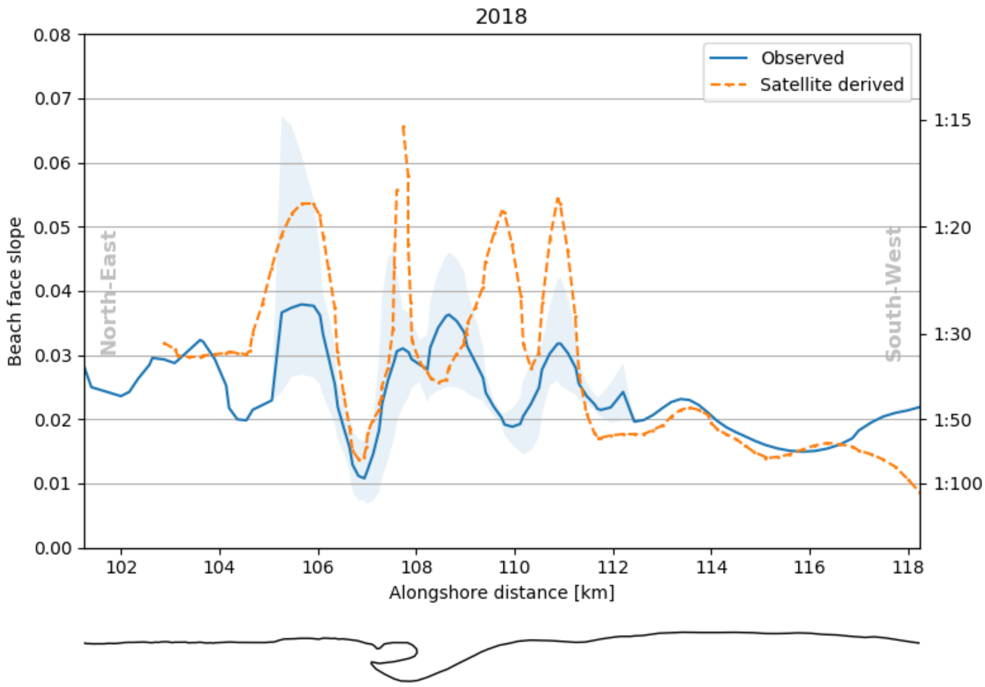

Figure 4.9: The intertidal beach slopes as observed and satellite-derived using the Onrust method. The slopes are plotted against the alongshore position at the Delfland coast. Images are first manually screened for clouds, shadows and waves. The bandwidth around the observed slopes indicate the variability.

Sagar method. Remarkable is the high coverage* of the Onrust method: 96 % of all the transects have a reliable estimate of the intertidal beach slope. Like the Sagar method, the slope at the tip of the Sand Motor is underestimated, possibly because this region is very dynamic.

The Onrust method is also applied without the manual filtering step. The computed slopes are presented in figure 4.10. Surprisingly, there seems to be little difference between the satellite derived slopes for the Onrust method with manual (*RMSE* of 0.0099) and with automated filtering (*RMSE* of 0.0123). This suggests that the automated filtering steps are sufficient; at the Delfland coast this seems to be the case.

Comparison of the methods

All methods perform poor in the northeastern section of the domain. For a clear comparison of the four methods the coverage* and the *RMSE* valuses are summarised in table 4.1.

Although a single image method is much more vulnerable to outliers, the Onrust method can measure up to the compositing methods: The error is in the same order of magnitude as the other two methods. On the other hand the Onrust method has the potential to captures much more of the variability. Appendix G shows how the Onrust method can be applied seasonally.

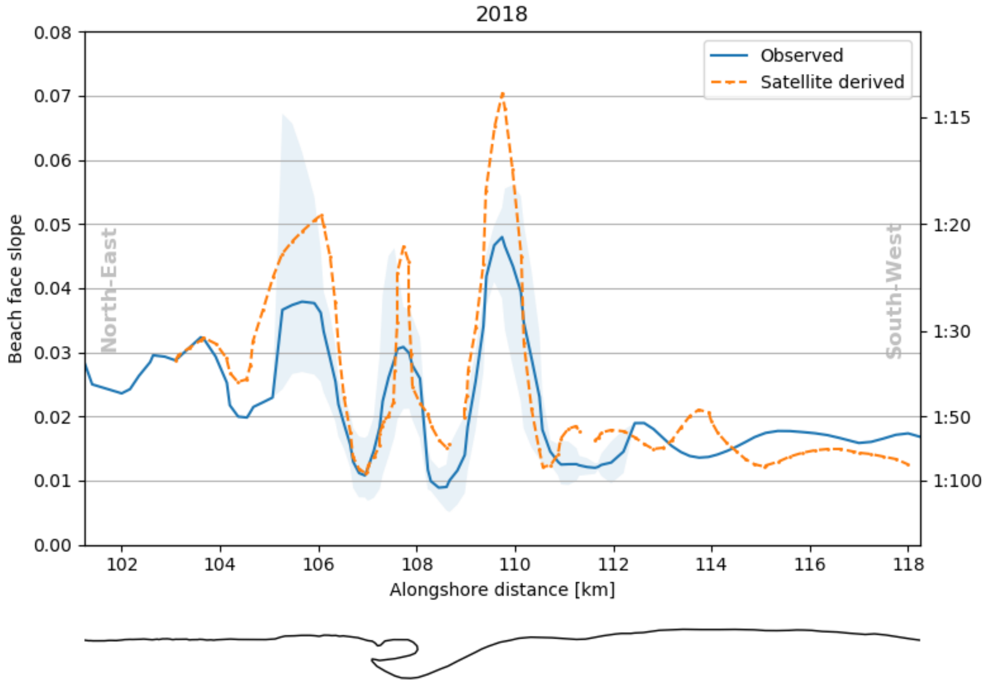

Figure 4.10: The intertidal beach slopes as observed and satellite-derived using the Onrust method. The slopes are plotted against the alongshore positions at the Delfland coast. No manual filtering has been applied. The bandwidth around the observed slopes indicate the variability.

		-		*Manual filtering*	
		Coverage	*RMSE*	Coverage	*RMSE*
Method FAST	Full year	0.75	0.0092		
Method Sagar	Full year	0.76	0.0185		
Method Onrust	Full year	0.094	0.0099	0.96	0.0123

Table 4.1: Summary of the coverage* and *RMSE* for the FAST, Sagar and Onrust method at the Delfland coast.

4.3 Case study: Duck coast

This section describes the results of a case study of the Duck coast in the United States of America. A description of the study site is given in 3.4.2. The intertidal beach slopes are computed at 30 cross-shore transects along a 1.2 km long coast near the Field Research Facility (FRF) operated by the U.S. Army Corps of Engineers. The satellite derived slopes are compared to slopes derived from field observations (U.S. Army Engineer Research et al., n.d.).

4.3.1 Analysis of the field observations

The beach profiles at the Duck hydraulic laboratory are measured monthly. This means that a lot of the dynamics are captured in the field observations. Not all of them, because of the short response times the slopes of the beach face may vary from day to day.

Figure 4.11 shows the profiles for three transects along the Duck coast. The beach face slopes are indicated by black lines. Two sets of slopes can be differentiated: steep and flat slopes. The flat slopes are found when the alongshore bar has moved into the intertidal zone.

This is also to be seen in figure 4.12, where the beach face slopes from the field observations are plotted against the alongshore distance. The two modes of the beach face slope are $\mathcal{O}\,(0.03 \text{ to } 0.04)$ and $\mathcal{O}\,(0.10 \text{ to } 0.12)$; the slope derived from the measured profiles constantly switches between these two modes.

4.3.2 Analysis of the satellite images

A total of 67 satellite images from 2018 are analysed. Water level measurements by the FRF are used as elevation data. Figure 4.13 shows the distribution of images in time plotted against the water level elevation. It also shows the distribution over the height: a bias to the middle and lower elevations can be observed.

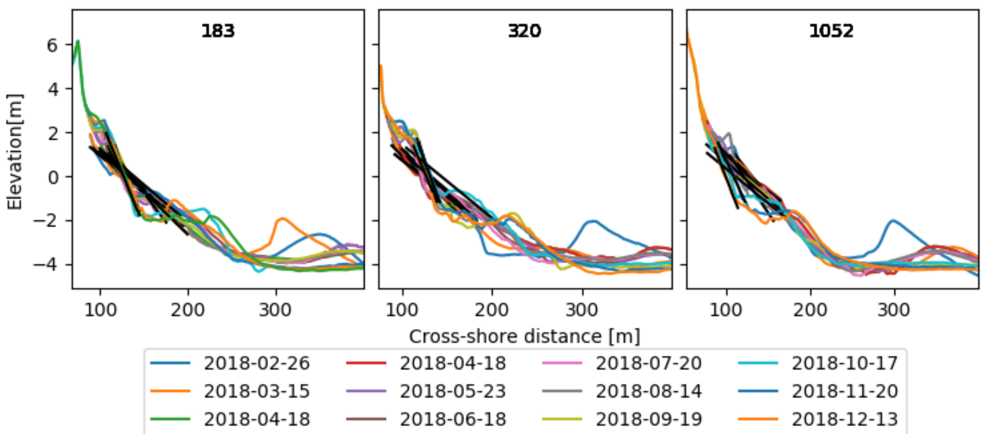

Figure 4.11: Observed profiles for three transects at the Duck coast. Measurements are done using the CRAB or the LARC. FRF uses a custom transect system indicated by the alongshore distance; the pier is located at transect 517. Transect 183 is to the south of the pier and transect 1052 to the north. There were 13 surveys in 2018. The beach face slopes are derived from the profiles and are indicated in black.

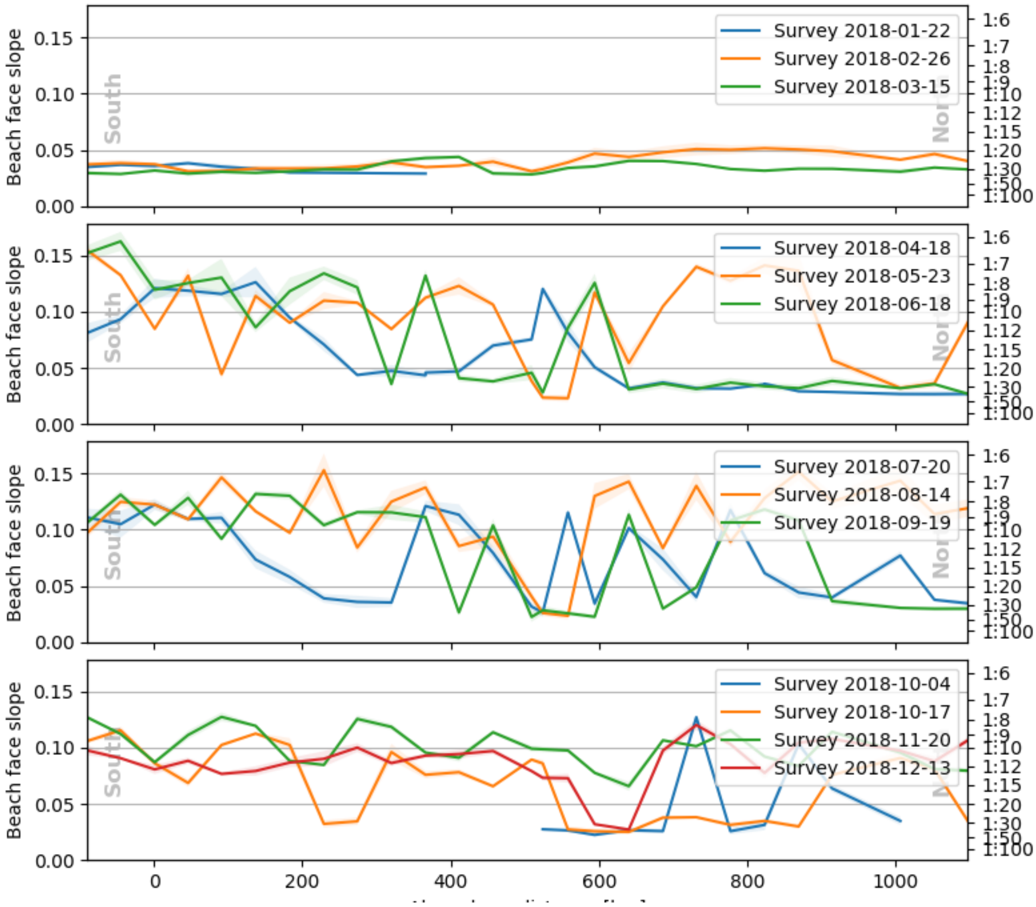

Figure 4.12: Observed beach face slopes along the Duck coast in 2018. The slopes are derived from the measured profiles. Two rough modes can be distinguished: $\mathcal{O}\,(0.03$ to $0.04)$ in the presence of an intertidal bar and $\mathcal{O}\,(0.10$ to $0.12)$ without it. The FRF research pier is located at transect 517.

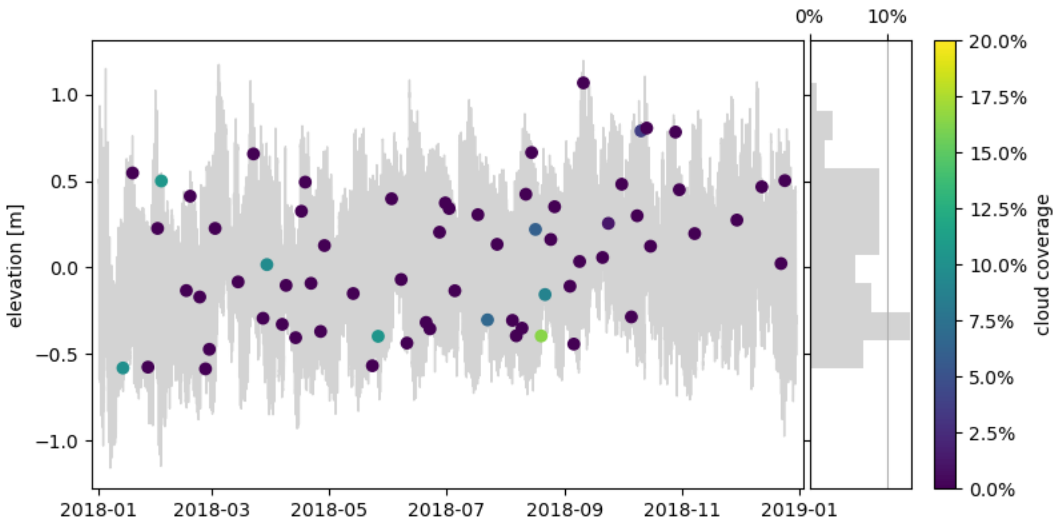

Figure 4.13: Distribution of images in time plotted against the water level. Each dot represents an image. The water levels have been recorded at FRF (U.S. Army Engineer Research et al., n.d.). The cloud cover limit is set at 20 % to ensure good image quality.

		-		*Manual filtering*	
		Coverage	*RMSE*	Coverage	*RMSE*
Method FAST	Full year	0.87	0.0180		
Method Sagar	Full year	0.13	0.0125		
Method Onrust	Full year	0.63	0.0388	0.73	0.0214

Table 4.2: Summary of the coverage* and *RMSE* for the FAST, Sagar and Onrust method at the Duck coast.

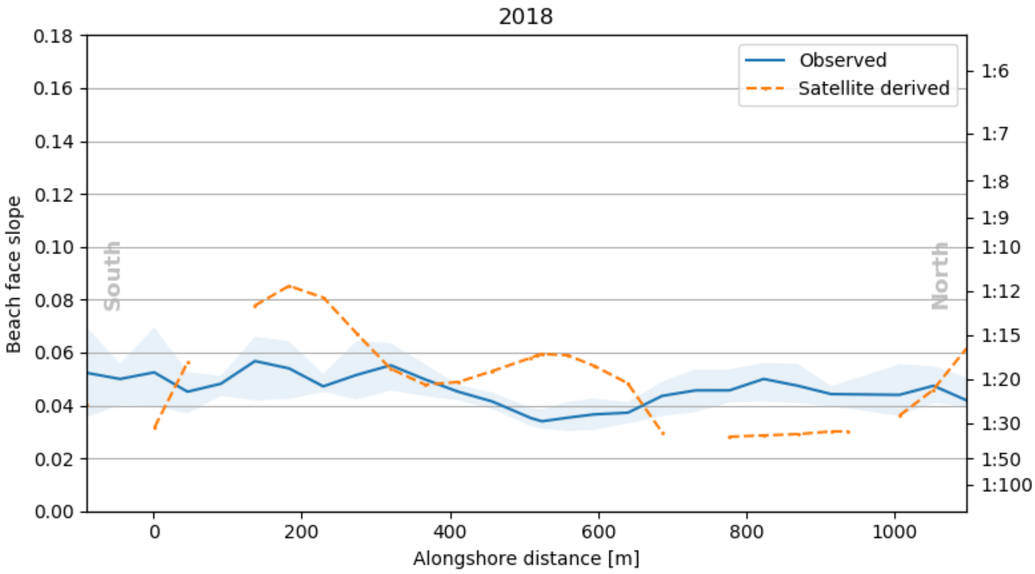

Figure 4.14: The intertidal beach slopes as observed and satellite-derived using the FAST method. The slopes ares plotted against the alongshore position at the Duck coast. The bandwidth around the observed slopes indicate the variability.

4.3.3 Analysis of the satellite derived intertidal beach slopes

The satellite derived slopes are computed for every transect along the Duck coast using the three methods discussed before. An alongshore overview is provided.

A summary of the coverage values and the *RMSE* values for the satellite derived slopes at the Duck coast can be found in table 4.2. Like the case study at the Delfland coast, the FAST obtains good results. The Onrust method seems to suffer a lot from outliers: the effect of manually filtering the satellite images results in a significant increase in the accuracy.

FAST method

Figure 4.14 presents the beach face slopes derived from satellite imagery using the FAST method. The satellite derived slopes are very close to the observed slopes, resulting in a very low *RMSE*: 0.0180.

Sagar method

For the Sagar method, the satellite derived intertidal beach slopes are plotted against the alongshore position in figure 4.15. The observed slopes are indicated in blue.

The coverage* is very small, see the figure. Only 13 % of the transects contain a

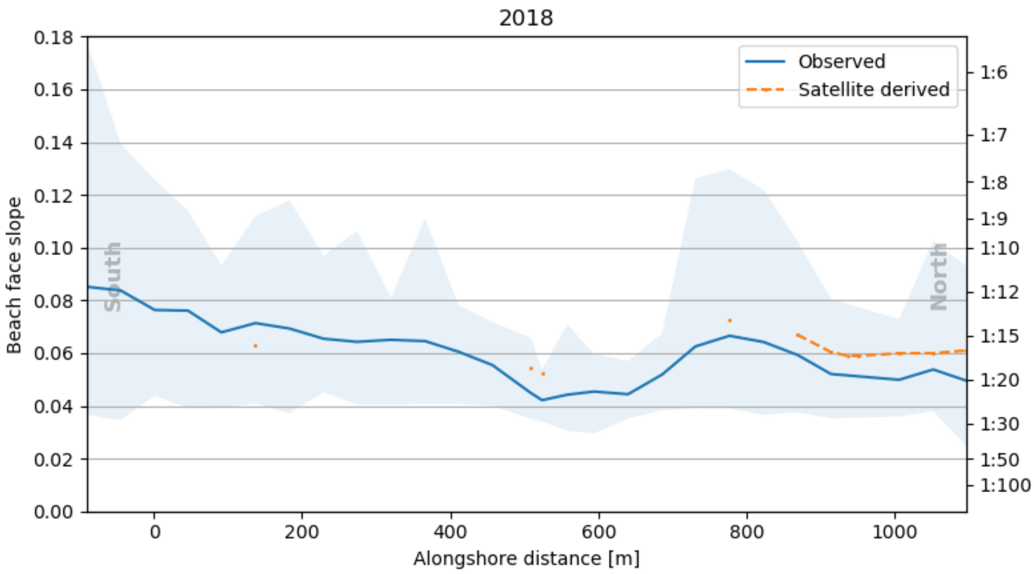

Figure 4.15: The intertidal beach slopes as observed and satellite-derived using the Sagar method. The slopes are plotted against the alongshore position at the Duck coast. The bandwidth around the observed slopes indicate the variability.

satellite derived slope. Despite the small coverage*, the satellite derived slopes are all in the range of the observed slopes. This results in a good *RMSE*: 0.0125.

Onrust method

As noted in table 4.2 the Onrust method works well when manual filtering is applied, but poor without. This can be seen when comparing figures 4.16 and 4.17. In figure 4.16 there are many satellite derived slopes within the variability of the observed slopes. The flatter slopes at alongshore position 600 m and the steeper slopes at 800 m can also be seen in the observed slopes.

Without manual filtering this method really suffers from outliers. At the Duck coast, there is often a band of wave foam that leads to errors in the derivation of the intertidal beach slopes.

Clearly the FAST method scores better at the Duck coast. This can mainly be attributed to the strip of wave foam that results in outliers. Although the FAST method scores better, the *RMSE* has the same order of magnitude.

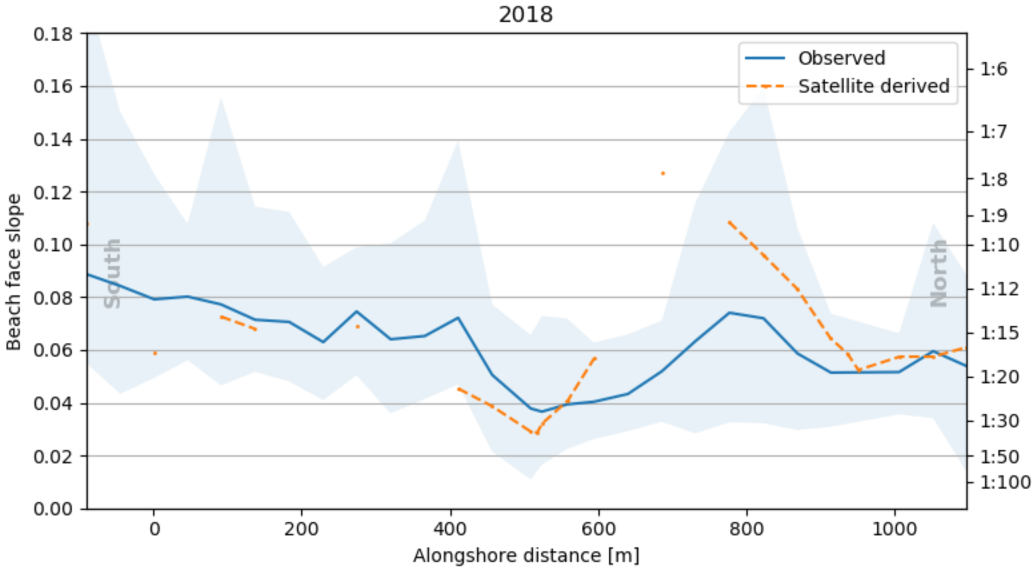

Figure 4.16: The intertidal beach slopes as observed and satellite-derived using the Onrust method. The slopes are plotted against the alongshore position at the Duck coast. Images are first manually screened for clouds, shadows and waves. The bandwidth around the observed slopes indicate the variability.

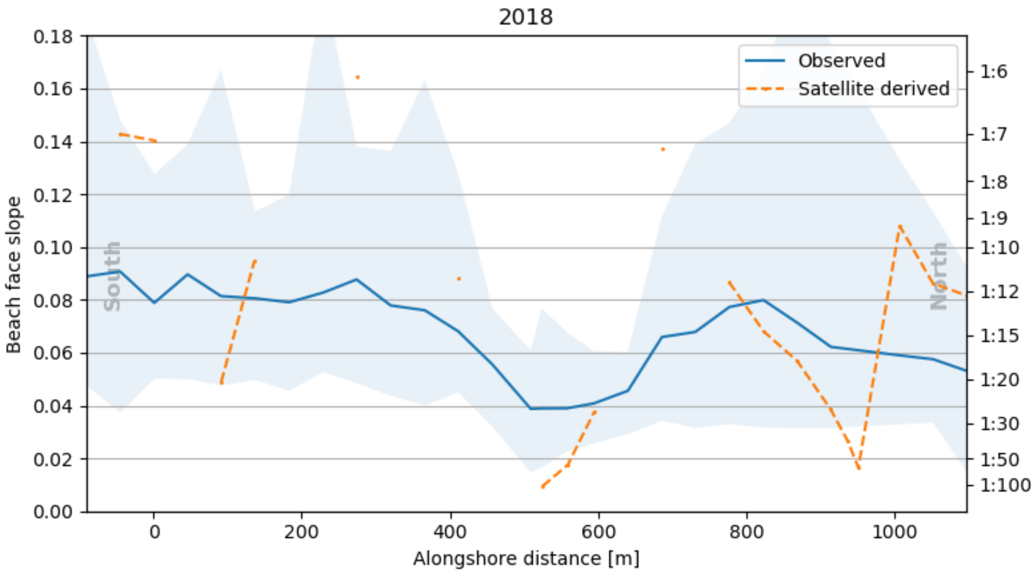

Figure 4.17: The intertidal beach slopes as observed and satellite-derived using the Onrust method. The slopes are plotted against the alongshore position at the Duck coast. No manual filtering has been applied. The bandwidth around the observed slopes indicate the variability.

4.4 Case study: Hasaki coast

This section describes the results of a case study of the Hasaki coast in Japan. A description of the study site is given in 3.4.3. The intertidal beach slopes are derived at 7 cross-shore transects along a 600 m coast centred around the Hazaki Oceanographical Research Station (HORS) pier. The satellite derived slopes are compared to slopes derived from field observations (Hasaki Oceanographical Research Station (HORS), n.d.).

4.4.1 Analysis of the field observations

The beach profiles along the research pier are obtained on a weekly basis. This means that a lot of the dynamics are captured in the field observations. Unfortunately, the beach profiles are only measured at this transect. Assuming that the Hasaki coast is alongshore uniform, the observed intertidal beach slopes are extended to the other transects. The observed slopes are given in figure 4.18.

4.4.2 Analysis of the satellite images

A total of 62 satellite images from 2018 are analysed. Water level measurements by the Choshi fishing port are used as elevation data. Figure 4.19 shows the distribution of images in time plotted against the water level elevation. It also shows the distribution over the height: a bias to the higher elevations can be observed. Although images are acquired at a regular 5 day interval, they are not equally distributed in the year. In summer (June - September), fewer images are available as this is the storm season in Japan.

4.4.3 Analysis of the satellite derived intertidal beach slopes

The satellite derived slopes are computed for every transect along the Hasaki coast using the three methods discussed before. An alongshore overview is provided. A summary of the coverage values and the *RMSE* values for the satellite derived slopes at the Duck coast can be found in table 4.3.

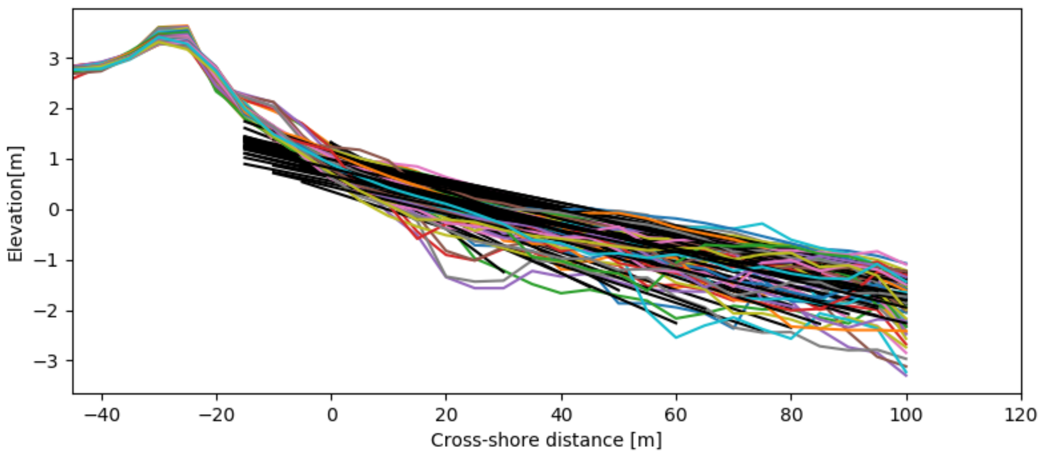

Figure 4.18: Observed profiles at the Hasaki coast. Measurements are done along the HORS pier. There were 50 surveys in 2018. The beach face slopes are derived from the profiles and are indicated in black.

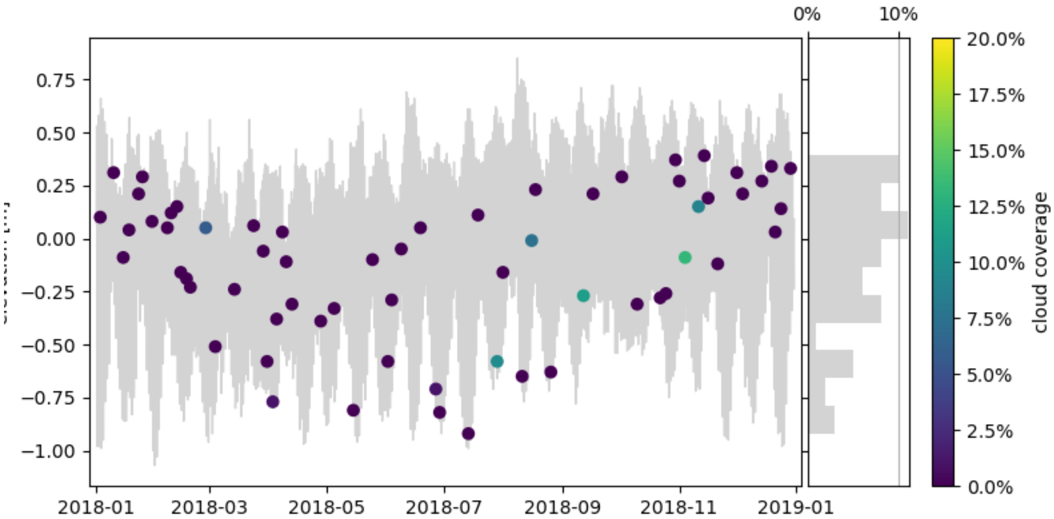

Figure 4.19: Distribution of images in time plotted against the water level. Each dot represents an image. The water levels have been recorded at the Choshi fishing port (Hasaki Oceanographical Research Station (HORS), n.d.). The cloud cover limit is set at 20 % to ensure good image quality.

		-		*Manual filtering*	
		Coverage	*RMSE*	Coverage	*RMSE*
Method FAST	Full year	0.71	0.0207		
Method Sagar	Full year	0.0	–		
Method Onrust	Full year	0.14	0.0189	0.71	0.0203

Table 4.3: Summary of the coverage* and *RMSE* for the FAST, Sagar and Onrust method at the Hasaki coast.

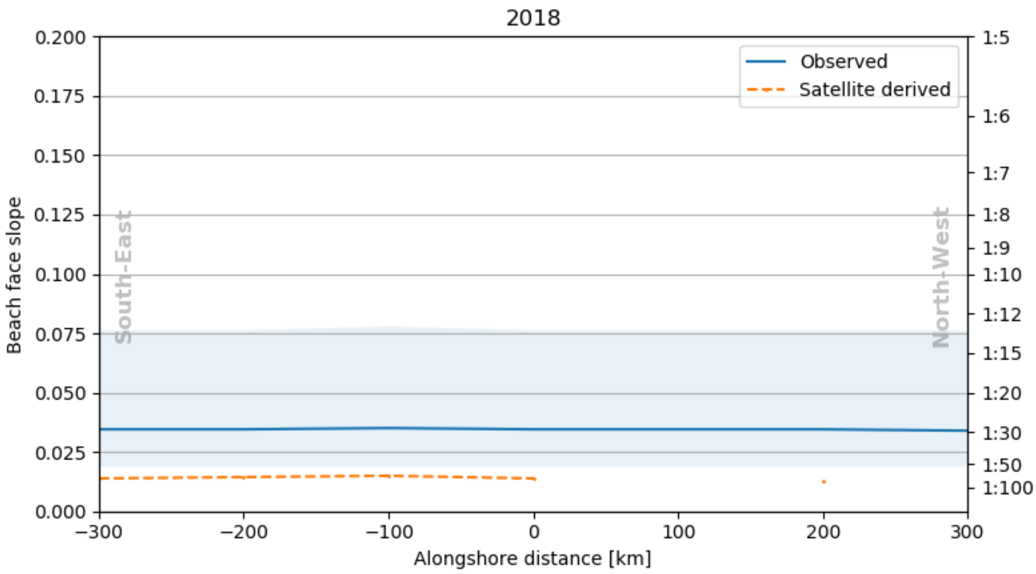

Figure 4.20: The intertidal beach slopes as observed and satellite-derived using the FAST method. The slopes are plotted against the alongshore position at the Hasaki coast. The bandwidth around the observed slopes indicate the variability.

The beach profiles at the HORS are only surveyed along the pier (alongshore 0 m). As only a small beach section is analysed (600 m length) the observed slopes are assumed alongshore uniform. The satellite derived slopes are computed at 7 transects in this beach section.

FAST method

Figure 4.20 shows the intertidal beach slopes as observed and satellite-derived using the FAST method. The satellite derived slopes are very alongshore uniform. The *RMSE* is 0.0207.

Sagar method

All slopes calculated using the Sagar method are found unreliable as discussed in chapter 3.2.5. Therefore, the coverage is 0.0.

Onrust method

Figure 4.21 and figure 4.22 show the intertidal beach slopes as observed and satellite-derived for the Onrust method with and without manual filtering. The effect of the manual filtering of the images on the satellite derived slopes is clearly visible. The slopes in figure 4.21 are found within the range of observed slopes. The *RMSE* is 0.0203, an excellent score.

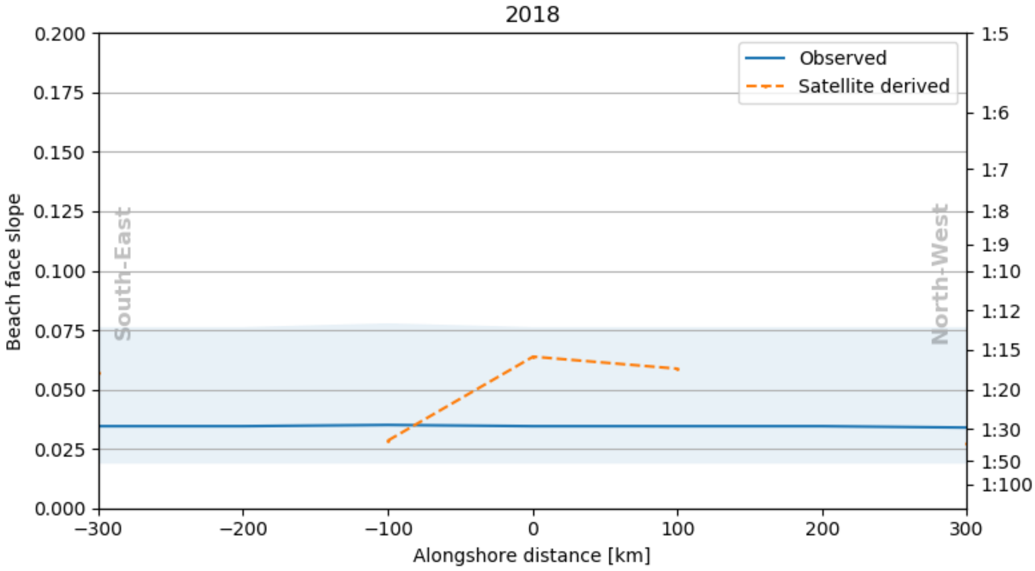

Figure 4.21: The intertidal beach slopes as observed and satellite-derived using the Onrust method. The slopes are plotted against the alongshore position at the Hasaki coast. Images are first manually screened for clouds, shadows and waves. The bandwidth around the observed slopes indicate the variability.

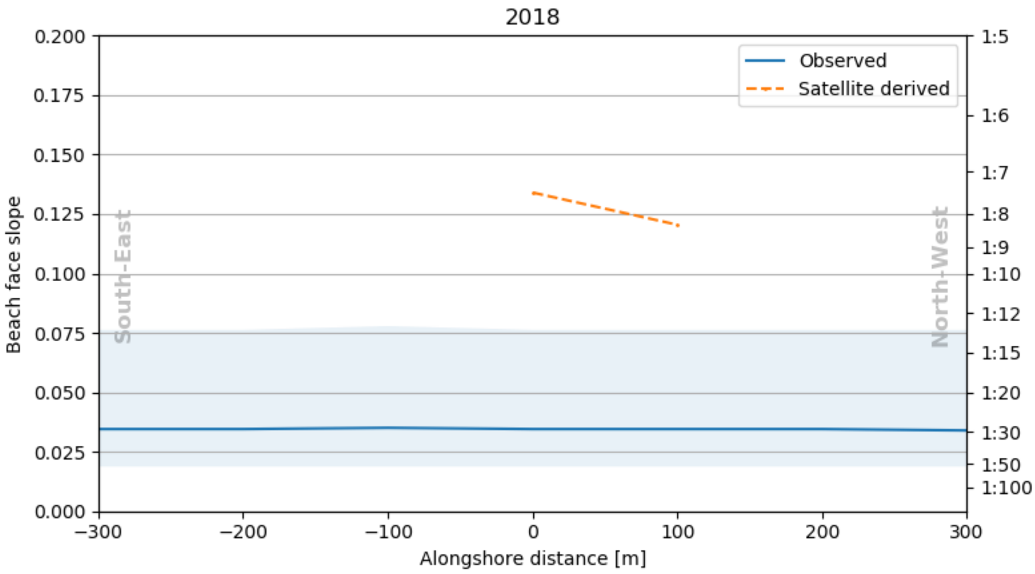

Figure 4.22: The intertidal beach slopes as observed and satellite-derived using the Onrust method. The slopes are plotted against the alongshore position at the Hasaki coast. No manual filtering has been applied. The bandwidth around the observed slopes indicate the variability.

5 Validation of the satellite derived sediment sizes

Chapter 3 describes a two-step methodology for estimating the sediment size of beaches. Each step is validated separately. In this chapter the satellite derived grain diameters are validated against field data from the three study sites (Delfland, Duck, Hasaki). First, the field observations are analysed. Then, the sediment size of the beach is derived from satellite images.

An estimate of the sediment size is computed using the intertidal beach slopes derived from satellite. The results from the Onrust method with manual filtering are used because they have small errors and capture the variability of the slope. No error analysis for the sediment size is included, because the current method is not considered accurate enough. To validate the satellite derived sediment size, the sediment class (e.g. fine, medium, coarse sand) is compared to the sediment class as measured in the field.

5.1 Beach face relations and equilibrium beach profile relations

As discussed in chapter 3.3, several methods from literature have been selected for deriving the median grain size from the beach face slope. These can be divided into two groups:

1. Beach face relations
2. Equilibrium beach profile relations

The beach face relations are a group of empirical relations describing the slope of the beach face. The equilibrium beach profile models are a group of empirical relations describing the shape of the beach profile. These equilibrium beach profile models are not specifically intended for describing the slope of the beach face and appendix E concludes that equilibrium beach profiles cannot be used for estimating the sediment size from the beach face slope. In the remainder of this thesis only the beach face slope models are considered.

5.2 Case study: Delfland coast

This section describes the results of a case study of the Delfland coast in the Netherlands. A description of the study site is given in section 3.4.1. The sediment size is derived from the satellite derived slopes presented in chapter 4. The sediment size is represented by a single parameter: the median grain size ($d50$). The derived values are compared to observed grain sizes from Rijkwaterstaat et al. (n.d.).

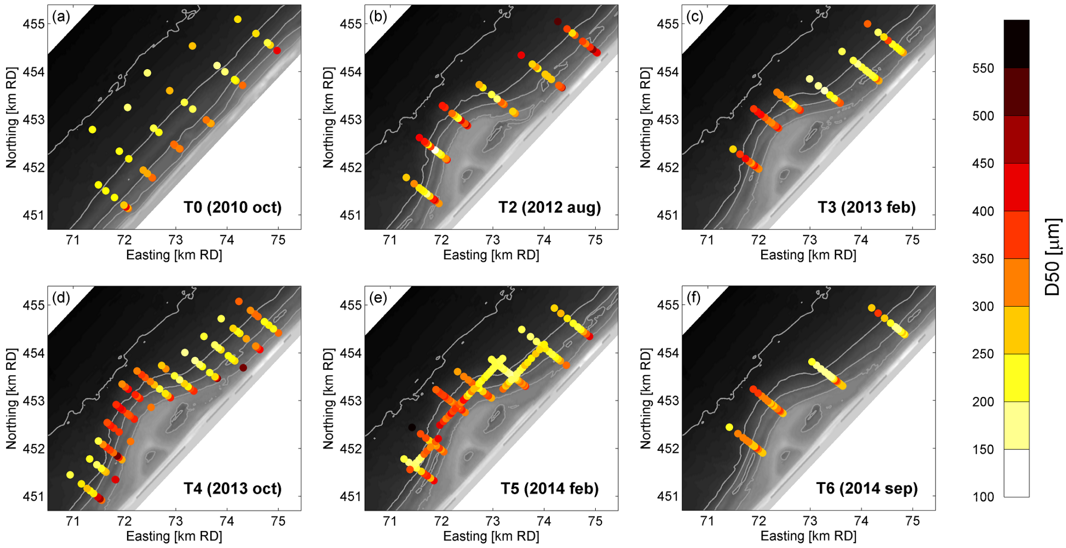

Figure 5.1: Median grain diameter of the sediment samples for Delfland coast. 7 surveys were carried out: T0 was prior to construction, T1 (not included) was during construction and the T2-T6 surveys show the development of the grain size after construction. (Huisman, 2019)

First an analysis of the field observations is done, in which the cross-shore and alongshore variability of the median sediment size are studied. Then, the grain sizes are derived using the satellite derived profiles to compare the performance of the different methods.

5.2.1 Analysis of the field observations

Huisman (2019, chapter 4) presents a thorough analysis of the grain size samples taken from the Sand Motor nourishment. 6 surveys between 2010 (prior to construction) and 2014 are studied, see figure 5.1.

The sand grain diameter was alongshore uniform in the pre-construction situation (panel a in figure 5.1). A fining of the sediment in the offshore direction was found. Typically a $d50$ of about 300 to 400 μm was found at the beach face and 200 μm at deeper parts of the profile.

The bed composition at the Sand Motor was significantly altered: coarser sand was used in the construction and hydrodynamic sorting processes have led to a gradual coarsening of the $d50$. Alongshore heterogeneity is prominent in deeper waters with coarse sediments at the tip of the Sand Motor. At the beach face the alongshore variation is not so evident, as can be seen in figure 5.1.

5.2.2 Satellite derived grain size

Every slope computes to a grain size estimate; multiple time sequences use the wave conditions corresponding to that period. The variability of the satellite derived slopes reflects in different grain size estimates. Subsequently, the grain sizes are averaged per transect: the number of satellite images per period is taken as weight factor.

Figure 5.2 shows the grain diameters derived from satellite imagery for the different beach face relations. The first thing to notice is the staggering of the observed grain sizes. It is unlikely that they change so much from transect to transect, but is a result of the spread in the measurements.

The field observations show that the sediment at the beach is a medium sand. Bujan's model underestimates the grain size and predicts a fine sand. The McFall relation is closest to the observed sizes and predicts a medium sand. Both the Bujan and McFall model find the largest grains at the tip of the Sand Motor; also the steepest slopes are observed here. Considering that the sediment sizes are derived from satellite imagery and generally available data, they come close to the observed values.

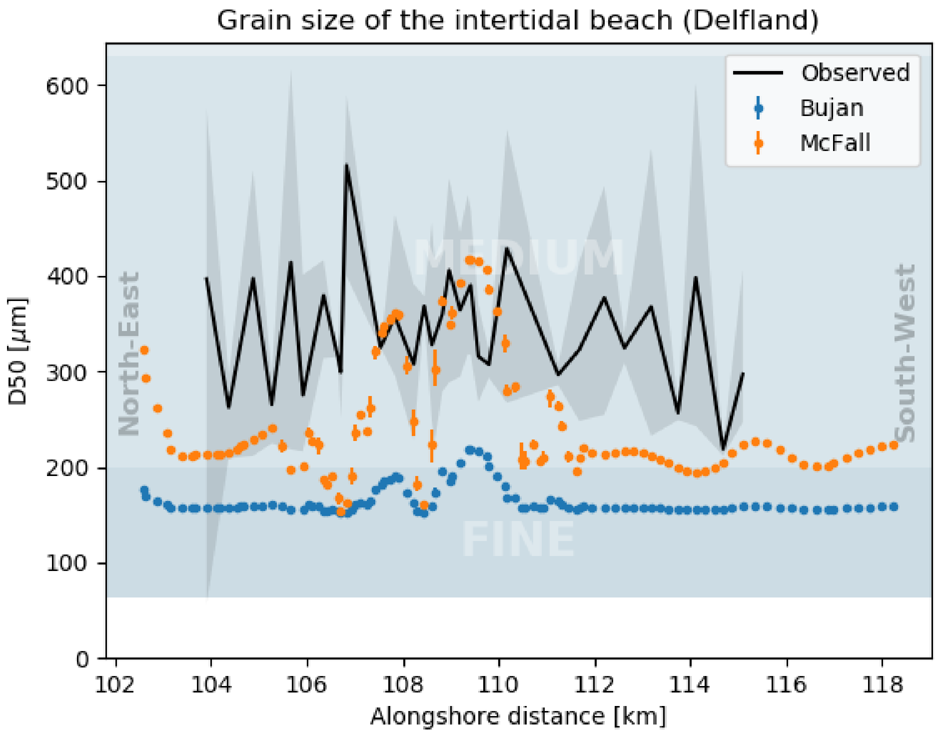

Figure 5.2: Sediment sizes as observed and satellite-derived using two beach face slope models. The grain sizes are plotted against the alongshore position at the Delfland coast. The bandwidth around the observed values indicate the spread in the measurements.

5.3 Case study: Duck

This section describes the results of a case study of the Duck coast in the United States of America. A description of the study site is given in section 3.4.2. The sediment size is derived from the satellite derived slopes presented in chapter 4. The median grain diameter is compared to measured values from U.S. Army Engineer Research et al. (n.d., 1984 & 1994). The measurements are quite dated, but because the beach at Duck is stable no large changes are expected.

5.3.1 Analysis of the field observations

Sediment samples are collected at 17 stations accross the profile to investigate the distribution of sediment. Figure 5.3 shows the median grain size at different positions in the profile. The sediment distribution is alongshore uniform.

At the dry beach the sediment has a bimodal distribution with the main component at 250 μm and the secondary group around 1000 μm (Stauble, 1992). This reflects the two modes of transport: aeolian transport in normal conditions and swash transport in high-water conditions. The sediment distribution is most varied in the intertidal zone. The temporal variation of the median grain size is exceptionally large; at times even in the gravel range ($>$ 2000 μm). Most of the time the coarse distribution occurred was after storm events (Stauble, 1992). The sediments in the nearshore zone are unimodal and show a gradual fining in the seaward direction. The sediment distribution in this zone is most stable. The average of the median grain sizes in the intertidal zone is used in the analysis.

The observed grain sizes ($d50$) are plotted against the elevation at which the samples were taken in figure 5.3. The different distributions are easily distinguished: a gradually fining in the seaward direction with very coarse samples in the intertidal zone.

Even though the sediment at the Duck beach is best characterised by a median sand of about 250 μm, a larger grain diameter is derived from the field observations. Since the adopted approach is limited to the intertidal zone, only these field observations are considered. The mean of the samples ($\varnothing$500 μm) is assumed to best describe the beach sand in the intertidal zone.

5.3.2 Satellite derived grain size

Figure 5.4 shows the grain size estimates derived from satellite imagery for the different beach face relations. The large variation of the sediment distribution in the intertidal zone comes out well in the figure. There is a large bandwidth around the observed values.

The predictions by the Bujan and McFall relation are close together. Bujan's model reacts more violently to the variability of the intertidal beach slopes, so computes a larger range of values. Both models correctly predict a medium sand at the Duck coast, but the McFall model is more stable along the different transects.

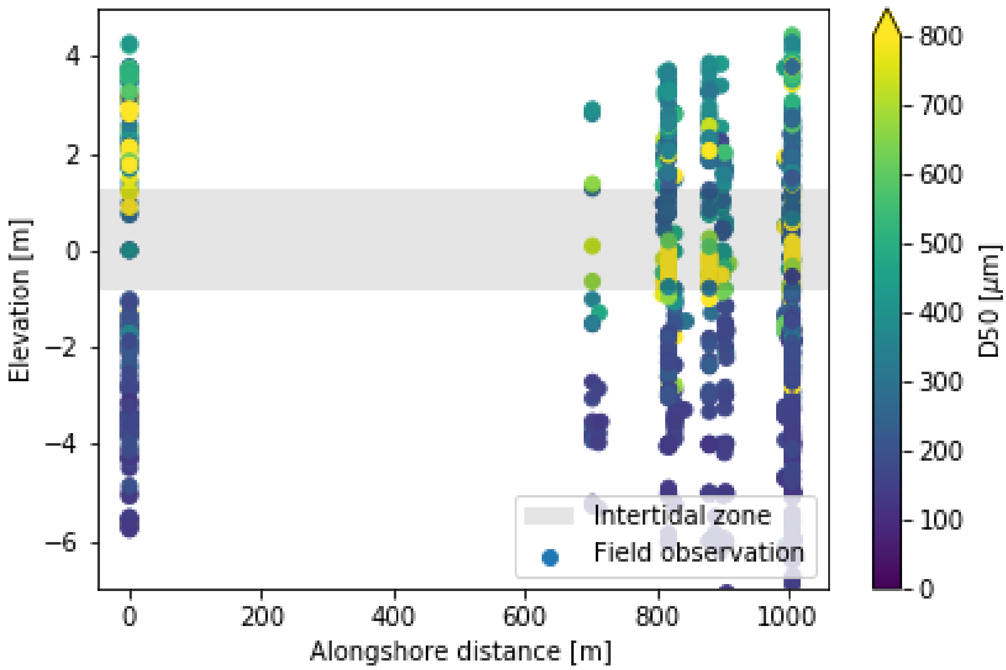

Figure 5.3: Spatial distribution of the median grain diameter at the Field Research Facility (FRF). A gradual fining of the sediment in the offshore direction can be observed. The distribution is bimodal with the main component at 250 μm and the secondary group around 1000 μm. In the intertidal zone very coarse sand and even gravel is found. The largest observed $d50$ is 3820 μm.

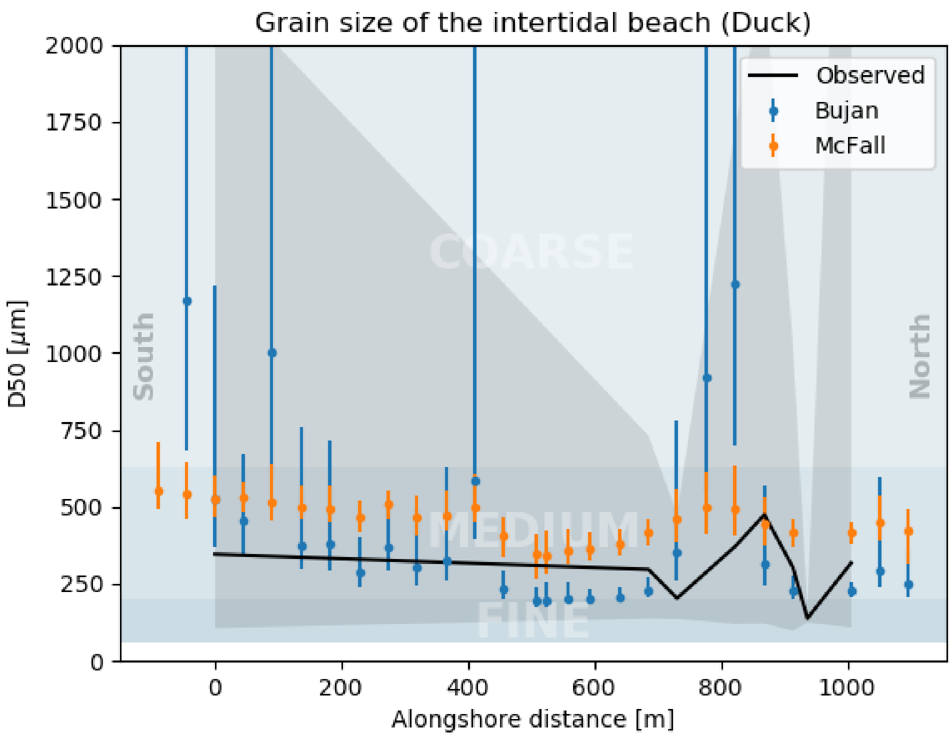

Figure 5.4: Sediment sizes as observed and satellite-derived using two beach face slope models. The grain sizes are plotted against the alongshore position at the Duck coast. The bandwith around the observed values indicate the spread in the measurements.

5.4 Case study: Hasaki

This section describes the results of a case study of the Hasaki coast in Japan. A description of the study site is given in section 3.4.3. The sediment size of the intertidal beach is derived from the satellite derived slopes presented in chapter 4. The median grain diameter is compared to measured values from Hasaki Oceanographical Research Station (HORS) (n.d.).

5.4.1 Analysis of the field observations

Sediment samples are collected regularly at various locations accross the profile, from $y = -60$ to $y = 50$. Figure 5.5 shows the median grain size ($d50$) in millimetre on the vertical axis and time on the horizontal axis. All sediment samples are collected along the HORS pier; the distribution is alongshore uniform. The exact location of the intertidal zone shifts depending on the time of year. It is usually between $y = 10$m and $y = 50$m.

5.4.2 Satellite derived grain size

Figure 5.6 shows the grain size estimates derived from satellite imagery for the different beach face relations. At $y = 0$ m (alongshore distance), the grain sizes have a deviating value. A possible explanation for this is the local situation at this transect. Steeper beach slopes were found here due to the Hazaki Oceanographical Research Station (HORS) pier. The grain sizes at the other transects give a more uniform image.

In general, the same results are established for the Hasaki site as for the Delfland and Duck case study. The satellite derived intertidal beach slopes at the Hasaki coast were exceptionally alongshore uniform. This is also evident in figure 5.6, where the satellite derived grain sizes at the different cross-shore transects are close together. The prediction by the McFall model is very close to the observed value. Bujan's relation underestimates the grain diameter.

Overall, the McFall relation seems to perform best.

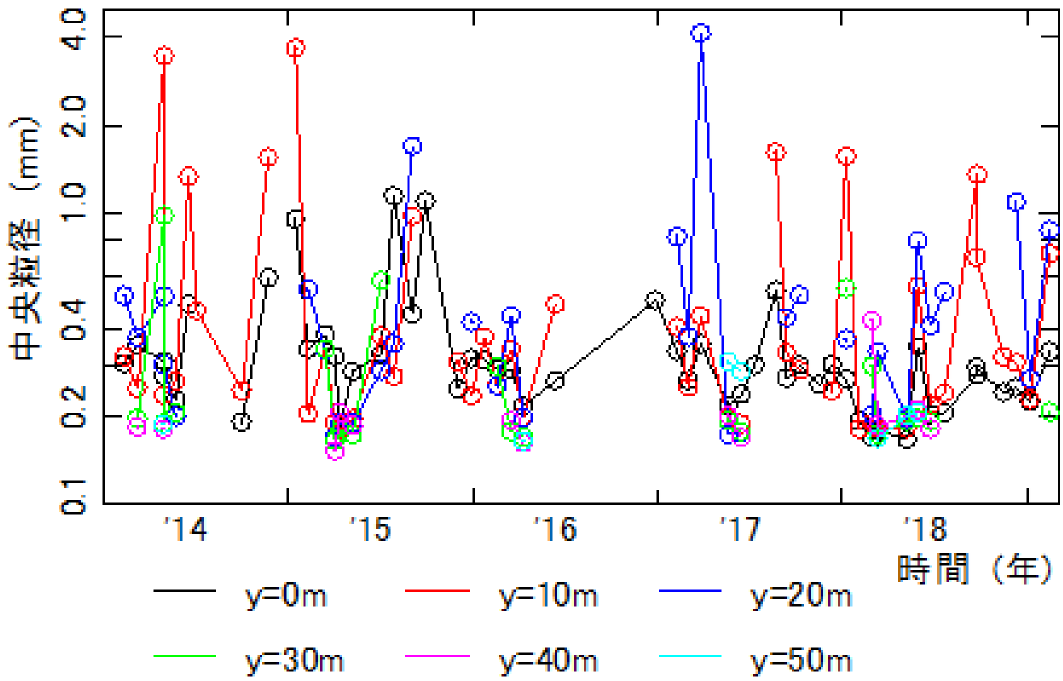

Figure 5.5: Spatial and temporal distribution of the median grain size along the HORS pier. Time is plotted on the horizontal axis (in years) and the sediment $d50$ is plotted on the vertical axis (in mm). The grain size is measured at various cross-shore positions, indicated by the y-coordinate.

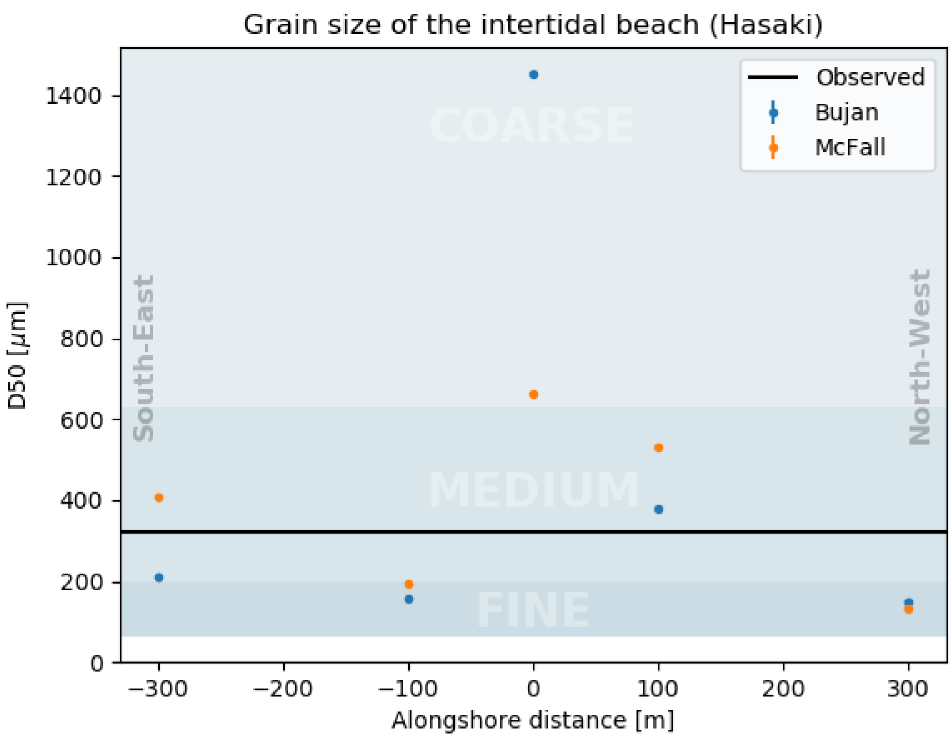

Figure 5.6: Sediment sizes as observed and satellite-derived using two beach face slope models. The grain sizes are plotted against the alongshore position at the Hasaki coast. Sediment samples are only taken at the HORS pier (0 m alongshore), but is presented here as alongshore uniform. The error bars indicate the variation of the grain size for different time periods.

6 Discussion

This chapter expands the time horizon by looking at different years for the Delfland coast. In addition, it reflects on the significance and interpretation of the satellite derived slopes of the intertidal beach described in chapter 4. A reflection is given on the grain sizes described in chapter 5. Furthermore, the most important limitations of the methods employed are studied and presented in this chapter.

6.1 Expanding the time horizon

One of the amazing things about satellite imagery is that an entire data catalogue is ready to be analysed. It is therefore possible to look back in time and compare different time periods. 2017, 2018 and 2019 are analysed, because Sentinel-2B has only been operational since 2017. Figure 6.1 shows the satellite derived slopes along the Delfland coast in 2017, 2018 and 2019.

Due to the unavailability of Sentinel-2B in the first part of the year, there are only 31 images in 2017. And as discussed in chapter 4, the derivation of the intertidal beach slopes improves with more images. As a result, the coverage is lower in 2017 than in 2018 and 2019. Unfortunately, not all surveys for 2019 are currently available which means that the observed slopes only cover the Sand Motor area.

The Delfland coast is a very dynamic area with high erosion rates at the tip of the Sand Motor, accretion of the beaches surrounding it and a large seasonality. Because of this, there are large differences in the slopes over the years. The relatively stable southwestern section of the domain proves that the Onrust method performs consistent over the years. Figure 6.1 show that the derivation of the intertidal beach slopes also scores well in other years than 2018.

6.2 Interpretation of the satellite derived intertidal beach slopes

The beach is a dynamic system that is never in a truly equilibrium state. Thus, some amount of scatter is expected from the measured beach slopes compared to the satellite derived slopes. This is even apparent from the variation in the observed slopes as has been demonstrated in chapter 4.

Figure 4.4, for example, shows the observed slopes at the Delfland coast. A clear is visible in the profiles obtained at different times in the year. This can largely be attributed to seasonal effects. However, since variations in the beach face slope have response times of several days or even minutes (Holland & Holman, 1996), this can also be a result of individual storm events.

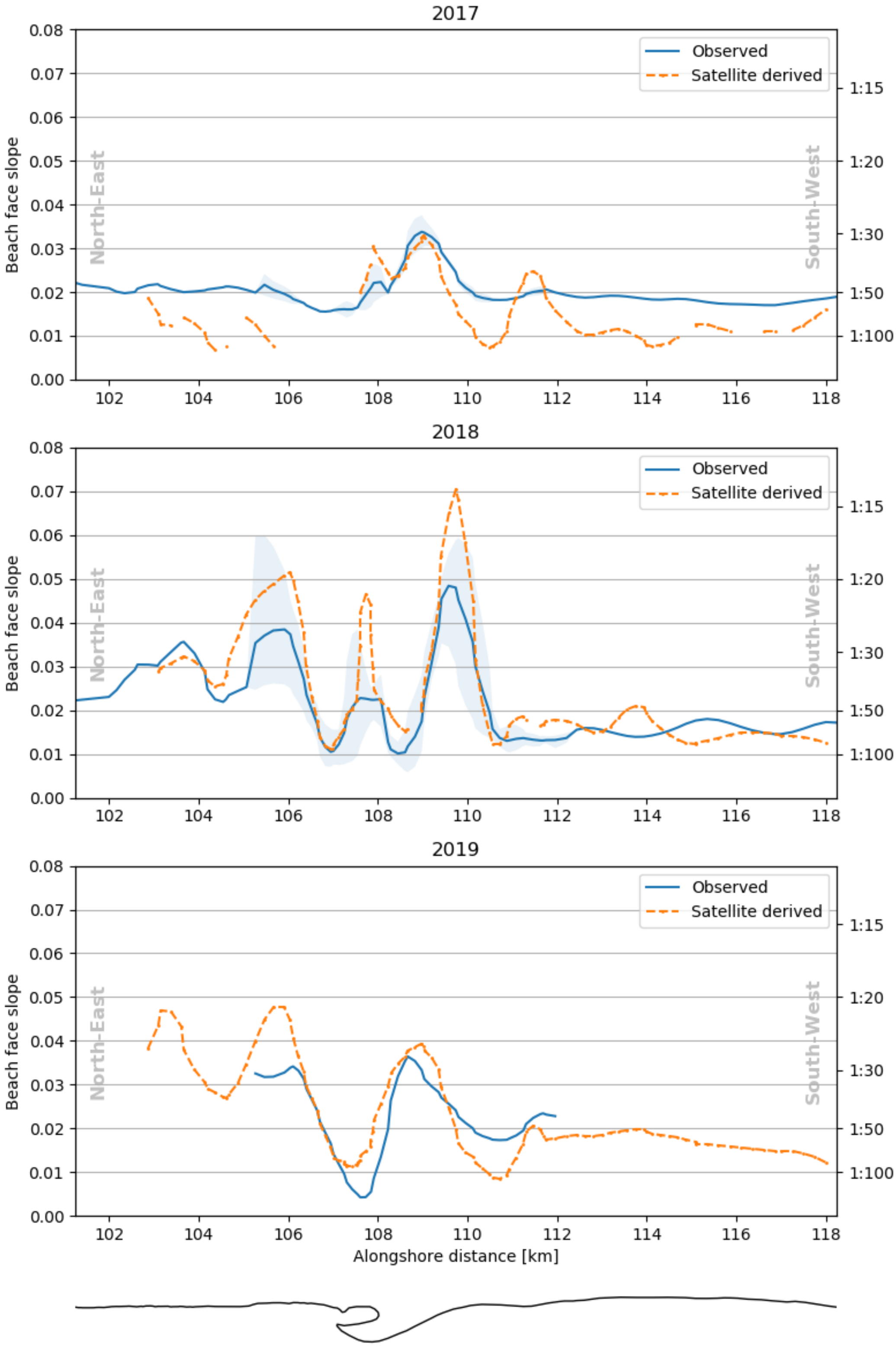

Figure 6.1: The intertidal beach slopes as observed and satellite-derived using the Onrust method. The slopes are plotted against the alongshore position at the Delfland coast for 2017, 2018 and 2019.

This raises the following question: How should the satellite derived intertidal beach slopes be interpreted? For the methods discussed here, images from multiple tidal stages need to be combined in order to be able to determine the slope of the intertidal beach. This means, by definition, that the time period for determining the slope from satellite images is longer than the response time of the beach face. The intertidal beach cannot be assumed to be stable during the time sequence of the satellite images.

In this thesis, the satellite derived intertidal beach slope is interpreted as an 'average' beach slope for the time period it was derived. Variations are certain and are attributed to the everchanging environmental conditions.

6.3 Limitations of the slope derivation methods

Five major limitations incorporated in the methods of section 3.2 or imposed by physical processes at the beach face are listed below.

1. Minimum number of images
2. Dynamics of the beach profile
3. Horizontal extent of the intertidal zone
4. Data availability
5. Beach profile shape

As the satellite derived slopes form the basis of the grain size estimation, these limitations also apply to the sediment size derivation. Herafter, each of the limitations is discussed in detail.

6.3.1 Minimum number of images

The methods incorporate a lower limit on the number of satellite images. The background of this minimum is different for the three methods discussed. Thus, the minimum number of images differs, as indicated below:

Method FAST	±	17 images
Method Sagar	±	50 images
Method Onrust	±	10 images

The FAST method uses a composite technique to make Time Ensemble Averaged (TEA) images. FAST (2017) uses the entire Landsat archive, but it is assumed that a similar analysis can be out with fewer images. With 17 images, it is reasonable to assume that the images cover a large portion of the tidal range (> 95 % certainty).

The Sagar method uses a composite technique to improve image quality. The advantage is improved image quality; one of the disadvantages is a large number of images required. Donchyts (2018) states that a large number of images is required, for computing composite images, to ensure that the distribution of reflectance values converge to the actual distribution. A minimum number of images was not mentioned and is likely to fluctuate per location. Here, 50 images is assumed to be the bare minimum for the Sagar method.

The Onrust method derives the slope by fitting a number of datapoints. Theoretically only two datapoints are required to define a slope, however, due to outliers and the tidal bias more images are needed. Reasonable results were obtained with 10 images.

6.3.2 Dynamics of the beach profile

The satellite derived slope is interpreted as an ‘average’ beach face slope and therefore allows for a certain variability. As the beach face is a highly dynamic zone, a spread around the satellite derived intertidal beach slope is expected.

Larger scale dynamics of the beach system, however, pose limits to the extraction of the slopes. Significant changes to the beach profile lead to a shift of the mean shoreline position: the shoreline position cannot be explained by the varying tides anymore. As these dynamics occur on a larger time scale, they pose limits to the maximum number of images that can be combined. Three types of coasts have been identified where this limitation occurs:

- Erosive coasts
- Accreting coasts
- Seasonal coasts

Along the Delfland coast, for example, a lot of erosion is observed at the location of the Sand Motor. At the tip of the Sand Motor erosion rates exceeded 140 m in the first year (De Schipper et al., 2014). In this thesis no research has been done in analysing the timescales of the erosion, but it is clear that this limits the maximum number of images. The database of the Shoreline Monitor can help to determine whether a coast is stable.

Seasonal variations have the same effect, even though the spatial dimension of the variability is smaller. The shift of the mean shoreline positions leads to compatibility issues, limiting the maximum length of the analysis period. For purely seasonal coasts, intra-annual image collections might form a solution.

A three-month analysis period was proposed to minimize these effects. With revisit times of 5 days (for Sentinel-2) this is equivalent to approximately 18 images. This limits the applicability of the Sagar method to areas with limited seasonability and stable coasts. The results in appendix G demonstrate that a three-month analysis is possible with the Onrust method, but that accuracy decreases.

6.3.3 Horizontal extent of the intertidal zone

The methods proposed in this thesis assume that the intertidal zone can be observed from the satellite images, but in some situations the horizontal extent of the intertidal zone is too small.

In microtidal environments, such as the Mediterranean Sea, the tidal range is small. This means that there is a limited difference between the high-water shoreline and the shoreline at low tides. At the Ebro Delta Coast for example (see appendix F), the tidal range is only in the order of 0.25 m; the variability in the shoreline position is in the order of one pixel. This appears insufficient to determine the slope of the intertidal beach. This study does not answer the question what the minimum size of the the intertidal beach is, however, based on the Ebro Delta case it is expected to be at least twice the pixel resolution (= 20 m)

Very steep beaches have a similar effect: the displacement of the shoreline between high and low water levels is small. With such a small horizontal extend of the intertidal zone it is not possible to derive the slope. Only satellite images with a higher spatial resolution can solve this limitation.

6.3.4 Data availability

Crucial for the slope derivation is the availability of water level information. The approach in this thesis leans on measurements from nearby tidal stations for elevation data. These measurements do not only include the astronomical, but also the meteorological tides. This is important because the effect of wind, seasonal influences or storm surge events can affect the location of the shoreline by tens of metres (Bishop-Taylor et al., 2019). Wave run-up also influences the location of the waterline (García-Rubio et al., 2015), but is too unpredictable to take into account.

This dependence on accurate water level data limits the approach discussed in this thesis to locations near measurement stations.

6.3.5 Beach profile shape

Irregular beach profile shapes limit the application of the methods discussed in this thesis. Water level data is required to determine the elevation of the Satellite Derived Shorelines (SDSs). Bishop-Taylor et al. (2019) describe a situation where an elevated intertidal reef platform causes the tides to become asymmetrical. The shallow platform inundates rapidly and drains slowly resulting in 'trapped' water. At these locations the tidal heights are unsynchronised from the actual water levels and the methods described in this thesis are inadequate.

In addition, complex bar/trough systems in the intertidal zone ensure that no accurate intertidal beach slope can be derived. Bars in the intertidal zone are detected by the SDS extraction algorithm. This means that the data points in the lower intertidal zone are found relatively far offshore. Since a linear model is fitted through the data points these complex shapes cannot be accounted for. Ultimately this means that the intertidal slopes are underestimated.

6.4 Interpretation of the satellite derived grain sizes

Marine sediments are mixtures of grains of varying sizes. Its properties are determined by the characteristics of the different particles, the distribution of the different components, the level of sorting, etcetera. Clearly, these mixtures cannot be fully characterised by means of a single parameter and doing so will result in the loss of information on the true nature of the seabed (Bockelmann et al., 2018). For simplicity, however, this thesis uses median grain diameter (d50) to characterise the beach. The $d50$ is often used as a proxy for the sediment distribution as it provides good insight into the stability.

Beaches experience a natural sediment sorting with finer sediments offshore. This gradual fining was clearly visible in the sediment observations at the Duck coast, see figure 5.3. The derivation of the grain size from satellite imagery cannot account for this natural sorting. Fortunately, the sediment in the intertidal zone is considered most representative for the entire profile: Bascom (1951) suggested that if only one sample could be collected to represent the grain size of a beach, the best position to use as a reference sampling site was the midtide area.

This means that the satellite derived grain size should be interpreted as a representative grain diameter: beaches with a similar grain size have similar stability characteristics.

6.5 Limitation of the sediment size derivation

Three major limitations incorporated in the methods of section 3.3 or imposed by physical processes at the beach face are listed below:

1. Unconsolidated granular sediments
2. Data availability
3. Unequal wave forcing

6.5.1 Unconsolidated granular sediments

The beach face slope models only apply to beaches composed of unconsolidated granular sediments such as sand and gravel. The grain size is a good proxy for stability of unconsolidated granular sediments. Vegetated coasts, cliff coasts or salt marsh coasts, for example, have other parameters influencing the stability. Consequently, the beach face slope relations are not valid here.

6.5.2 Data availability

The amount of data required differs per model, but all beach face relations considered in this thesis require information about the wave climate. As discussed in appendix B the wave height and wave period are important parameters for determining the slope of the beach.

This thesis relies on wave information from nearby buoys. As it is not exactly clear which wave characteristics are required the averaged conditions are used.

There is a contradiction here: this research aims at paving the way for a global derivation of the beach grain size. But for solving the data gab in the intertidal beach slopes and the grain size accurate water level and wave data are required.

6.5.3 Unequal wave forcing

Strongly curved shorelines, such as found at the Sand Motor peninsula or at the Ebro Delta coast, experience a difference in wave forcing along the shoreline. Wave focussing at the tip of the Sand Motor means that the wave energy is underestimated here. At the Ebro Delta coast it is mainly the shoreline orientation that explains the difference in energy of the incoming waves. This results in an alongshore variation of the grain size.

The methods discussed in this thesis cannot account for this alongshore variation of the grain size for two reasons:

1. Not all beach face slope models directly depend on the incoming wave energy. The McFall relation, for example, has only three exposure classes so cannot account for this.

2. Such detailed information about the waves is simply not available and can only be obtained by employing a numerical model. That is beyond the scope of this thesis.

6.6 Reflection on the validation results

Chapter 4 and chapter 5 hold the validation for a method for deriving the grain size of a beach from satellite imagery. First, the slope of the intertidal beach is computed. Three methods (FAST, Sagar and Onrust) and three study sites (Delfland, Duck and Hasaki) are considered.

6.6.1 Assessing the accuracy of the intertidal beach slopes

One of the difficulties of assessing the accuracy of the intertidal beach slopes is that it is hard to establish the ground-truth. The beach slopes are rarely measured in the field, but can be determined from profile surveys. Two problems arise:

1. The definition of the intertidal zone leaves a lot of room for interpretation so that the exact boundaries of this zone are unclear. A different slope can be found depending on the phase of the tidal cycle or the wave conditions. Moreover, a tidal bias occurs due to the uniform image frequency: it is unclear which slope is being measured by the satellites.

2. The profile surveys represent the instantaneous shape of the beach, whereas the intertidal beach slopes derived by satellite is interpreted as the average slope. Due to the short response times to the varying wave conditions, the slope is dynamic within the time sequence of the imagery. Some difference between the surveyed slopes and the derived slopes is therefore explicable.

Clearly, validating the intertidal beach slopes is not straightforward. Despite the two problems above, the correlation coefficients demonstrate that each of the three methods can, to some level, predict the slope of the intertidal beach.

This study also reveals (see appendix F) the sensitivity of the Otsu thresholding algorithm. Due to the size of the Ebro Delta, this case study spans multiple image tiles. In the overlapping sections differences in shoreline positions were observed exceeding 20 metres based on the same underlying imagery. This highlights a sensitivity of the Otsu thresholding algorithm to the total collection of pixels which implies a user-dependency. The methods in this thesis strictly rely on the classification of water and non-water pixels. The consequence of this sensitivity is unknown.

6.6.2 Comparison of the slope derivation methods

The analysis has shown that the FAST method is most robust. Good coverage and Root Mean Square Error (*RMSE*) values were found at all study sites. No manual filtering is required and basic tidal information is sufficient.

It turned out that the composites built by the Sagar method were not clear: there were still waves, shadows and clouds in the images. This indicates that a yearly collection of images is insufficient and that more images are required.

Although initially the results by the Onrust method without manual filtering were not really satisfying in all aspects, the approach is promising. The method with manual filtering shows the potential if an improved SDS algorithm is applied. Moreover, the Onrust method can be applied to seasonal collection of images to capture the variability of the beach face. Leaving aside the manual filtering step, the Onrust method

	Coverage	*RMSE*
Delfland	0.80	0.0119
Duck	0.58	0.0173
Hasaki	0.47	0.0205

Table 6.1: Average validation results for the three study sites.

is most interesting for deriving the grain size from satellite imagery. The correlation coefficients (table 6.1) indicate that satellite derived intertidal beach slopes reasonably match with the beach slopes in the field.

The large number of outliers that are found, especially for the Onrust method, is due to the chosen method for extracting SDSs. This method was proven on composite images but provides insufficient certainty for a method based on single images. The developments are going fast and better algorithms are available now.

6.6.3 Assessing the accuracy of the grain sizes

The step from satellite derived slope to grain size is simple but there are a number of circumstances that need to be considered. First, it was found that not all transect were perpendicular to the shoreline (specifically the JarKus transects). This is not a problem for deriving the slope, since the measured and satellite derived slopes are compared along the same transect. The 'actual' slope is steeper so this results in an underestimation of the median grain size. Second, the required wave characteristics are unclear and good wave information was not always available. Finally, the beach face slope relations are taken as is. They are validated in the corresponding research papers and simply applied in this thesis.

The validation results indicate that the grain size estimates are a little disappointing. However, at all study sites the correct sand type could be determined (coarse, medium, fine). The different study sites do not agree on the best beach face slope relation. Bujan et al. (2019) suggests that a different beach face slope relation might be the best at every study site. For the three study sites it would be the formulation of Bujan et al. (2019).

6.7 Significance of intertidal beach slopes and grain sized derived by satellite

This study is the first attempt to derive sediment sizes from satellite imagery. Although research has been done on determining the extent of the intertidal zone using satellite imagery, the step to estimating grain sizes has never been made.

The grain size is one of the most important parameters in coastal research. Therefore, it goes without saying that a good estimate of the grain size is important. Not only can this study provide information in data-poor regions, it also allows constructing timeseries. With more confidence, satellite derived intertidal beach slope and satellite derived grain size can potentially become a major source of data in the coastal engineering field.

7 Conclusions & recommendations

This research has explored the possibilities of deriving the sediment size by using remote sensing data. Multiple methods have been investigated. The most important findings and conclusions are presented here. Then, the rhree most important recommendations are discussed, which are based the limitations and potentials of the methods.

7.1 Conclusions

With the existing pressures on the coastal zone a thorough knowledge of the shore is becoming more and more relevant. This research aims at providing an alternative approach to solving the data gap. The main question in this research is:

To what level can we derive the beach grain size using Sentinel-2 images?

To answer this research question, multiple methods based on literature have been adapted, developed and employed. The methods have been validated to field data at three study sites. This justifies the following main conclusions:

- It is possible to derive the slope of the intertidal beach from satellite imagery. The three case studies show that accuracies of the satellite derived slopes are reasonably good. The corresponding *RMSE* values are in the order of 0.009 to 0.020 with respect to slopes of 0.015 to 0.10.
- The slope of the intertidal beach is very sensitive to the selection of the limits of the intertidal zone. Thus, comparing the satellite derived slopes to data from the field is not straightforward. This study obtained beach face slopes of 0.005 (1:200) and 0.065 (1:15) from the same surveyed beach profile by choosing a different extent of the intertidal zone. Due to the tidal bias it is unclear which part of the beach profile is being measured by the satellite imagery. This means that the limits depend on the location.
- Deriving the slope of the intertidal beach from satellite imagery requires a horizontal extent of the intertidal zone of more than two times the pixel size (i.e. > 20 m). This means that the methods presented here cannot be applied in micro-tidal environments such as the Mediterranean.
- There are many inaccuracies in images, such as wave foam and cloud cover which make it difficult to classify pixels as water or non-water. The FAST method is very robust to these inaccuracies: the coverage is relatively high and error values are small. The Sagar method requires a lot of images and the *RMSE* is high. The Onrust method uses single images which undoubtedly

means that it is very sensitive to these inaccuracies. After manual filtering of the images, the Onrust method has a very good coverage and contains only minor errors.

- A single-image-method such as the Onrust method has clear advantages: relatively few images are sufficient and no information on the variability is lost in compositing. Unfortunately, bad image quality ensures that the validation results are worse without manual filtering. Future improvements and analysis methods can eliminate the need of manual image filtering. Despite the clear advantages, this research does not endorse that a single image method is most promising. The best results have been achieved with the FAST method.

- It is possible to determine the sediment class of a beach from satellite imagery with very limited information of the beach. Fine, medium and coarse sands can be differentiated.
- Errors in the satellite derived slopes affect the grain size computation. In addition, there is a distribution of the median grain sizes. This means that the derivation of the sediment size is not accurate to the μm at this point.
- Equilibrium beach profiles cannot be applied to relate the slope of the intertidal zone to the grain size. Beach face models are accurate but means dealing with the unclear definitions of the beach face.
- Both the Bujan et al. (2019) and McFall (2019) relations have proven to do well in deriving the sediment class with the benefit that these relations are very simple empirical formulations. Besides the beach face slope, very little data about the beach is needed. As McFall (2019) quoted Albert Einstein: "Everything should be made as simple as possible, but not simpler".

To conclude, this research has shown that satellite imagery is a potential source of information for the intertidal beach slope and for the grain size. The approach presented here is a proof-of-concept, where the possibilities and some of the limitations of deriving slopes and grain size have been uncovered.

Promising results have been achieved for the derivation of the intertidal slopes. This offers interesting opportunities for creating a global-scale data set. Moreover, encouraging results were obtained for the grain size. To link back to the main question: The beach grain size can be derived using Sentinel-2 images to the level of sediment class.

7.2 Recommendations

Primarily based on the limitations and potential outcomes outlined in the discussion in chapter 6, three recommendations are conceived. This can provide direction for follow-up research.

7.2.1 Improving extraction of Satellite Derived Shorelines

The algorithm for extracting Satellite Derived Shorelines that was developed by Hagenaars (2017) was applied in this thesis. This method, based on the Normalised Difference Water Index (*NDWI*) classifier, has proven itself and was able to deliver a high benchmark accuracy (Hagenaars et al., 2018).

However, the *NDWI* classifier is very sensitive to disturbances such as clouds and wave foam. This makes the *NDWI* classifier unsuitable for a single image method as these disturbances are often present. Kelly & Gontz (2018) found that other water indices are more suitable for automated shoreline mapping than the *NDWI*. Unfortunately, none of the indices seemed to do well under all circumstances.

Vos et al. (2019) combined the *MNDWI* with a machine learning algorithm and obtained promising results. With the launch of the Google Earth Engine (GEE) computational power is no longer a problem. Machine learning seems to have the most potential for the automated mapping of shorelines.

7.2.2 Global application

This report contains a proof-of-concept of the derivation of intertidal beach slopes and grain sizes from satellite imagery. As satellite imagery is available around the world, this method has the potential to be employed on a global scale. This would create an interesting data set of grain size distribution around the world.

The current approach relies on accurate water level measurements from nearby tide stations. The data from these observation stations do not only contain the elevation by the astronomical tide, but also the meteorological tide. This is important because the effect of wind, seasonal influences or storm surge events can affect the location of the shoreline by tens of metres (Bishop-Taylor et al., 2019).

For the application on a global scale it is impossible to rely on observation stations around the world: model data can fill this gab. However, tidal models are not as accurate as the observational ones. This study is not able to quantify the effect of wind or storm surge, nor the effect of seasonal influences. Thus, this research cannot rule the consequence of switching to model data. The first step to a global application is to study the effect of using a tidal model compared to measured elevation data.

7.2.3 Other satellite missions

This study was limited to Sentinel-2 imagery, but there are many more satellite missions available. This includes missions with a higher pixel resolution, up to 0.31 m (WorldView satellites). Such imagery can significantly improve the accuracy of the satellite derived intertidal beach slopes and allow steeper slopes and areas with smaller tidal ranges to be mapped.

Since these satellite missions do not have an open data policy, the opportunities lie in combining data from multiple satellite missions. This way it is possible to use the scarce high-resolution data along with the frequent medium resolution data and gain high temporal resolutions.

Bibliography

Aarninkhof, S. (2003). *Nearshore bathymetry derived from video imagery* (doctoral thesis).

Andrade, F., & Ferreira, M. A. (2006). A simple method of measuring beach profiles [Journal Article]. *Journal of Coastal Research*, *22*(4), 995-999. doi: 10.2112/04-0387.1

Bascom, W. N. (1951). The relationship between sand size and beach-face slope [Journal Article]. *Eos, Transactions American Geophysical Union*, *32*(6), 866-874. doi: 10.1029/TR032i006p00866

Bernabeu, A. M., Medina, R., & Vidal, C. (2002). An equilibrium profile model for tidal environments [Journal Article]. *Scientia Marina*, *66*(4), 11. doi: 10.3989/scimar.2002.66n4325

Bernabeu, A. M., Medina, R., & Vidal, C. (2003). A morphological model of the beach profile integrating wave and tidal influences [Journal Article]. *Marine Geology*, *197*(1), 95-116. doi: 10.1016/S0025-3227(03)00087-2

Bishop-Taylor, R., Sagar, S., Lymburner, L., & Beaman, R. J. (2019). Between the tides: Modelling the elevation of australia's exposed intertidal zone at continental scale [Journal Article]. *Estuarine, Coastal and Shelf Science*. doi: 10.1016/j.ecss.2019.03.006

Bockelmann, F.-D., Puls, W., Kleeberg, U., Müller, D., & Emeis, K.-C. (2018). Mapping mud content and median grain-size of north sea sediments – a geostatistical approach [Journal Article]. *Marine Geology*, *397*, 60-71. doi: 10.1016/j.margeo.2017.11.003

Bodge, K. R. (1992). Representing equilibrium beach profiles with an exponential expression [Journal Article]. *Journal of Coastal Research*, *8*(1), 47-55.

Bruun, P. (1954). *Coast erosion and the development of beach profiles* [Book]. U.S. Beach Erosion Board. Retrieved from https://hdl.handle.net/2027/uiug.30112088627325

Bruun, P. (1962). Sea-level rise as a cause of shore erosion [Journal Article]. *Journal of the Waterways and Harbours Division*, *88*(1), 117-132.

Bujan, N., Cox, R., & Masselink, G. (2019). From fine sand to boulders: Examining the relationship between beach-face slope and sediment size [Journal Article]. *Marine Geology*, *417*, 106012. doi: 10.1016/j.margeo.2019.106012

Dean, R. (1977). *Equilibrium beach profiles: U.s. atlantic and gulf coasts* [Book]. Center for Aplied Coastal Research.

Dean, R. (2008). Cross-shore sediment transport processes [Book Section]. In *Coastal engineering manual part iii : Coastal sediment processes* (chap. 3).

De Schipper, M., De Vries, S., Stive, M., De Zeeuw, R., Rutten, J., Ruessink, B., . . . Van Gelder-Maas, C. (2014). Morphological development of a mega-nourishment: First observations at the sand engine [Conference Paper]. In *Icce 2014: Proceedings of 34th international conference on coastal engineering.* Coastal Engineering Research Council.

Dickson, M. E., Walkden, M. J. A., & Hall, J. W. (2007). Systemic impacts of climate change on an eroding coastal region over the twenty-first century [Journal Article]. *Climatic Change*, *84*(2), 141-166. doi: 10.1007/s10584-006-9200-9

Donchyts, G. (2018). *Planetary-scale surface water detection from space* (doctoral thesis). doi: 10.4233/uuid:510bd39f-407d-4bb6-958e-dea363c5e2a8

Eleveld, M. A., van der Wal, D., & van Kessel, T. (2014). Estuarine suspended particulate matter concentrations from sun-synchronous satellite remote sensing: Tidal and meteorological effects and biases [Journal Article]. *Remote Sensing of Environment*, *143*, 204-215. doi: 10.1016/j.rse.2013.12.019

Emery, K. (1961). A simple method of measuring beach profiles [Journal Article]. *Limnology and Oceanography*, *6*, 90-93. doi: 10.4319/lo.1961.6.1.0090

European Space Agency. (2015). *Sentinel-2 user handbook* [Book].

FAST. (2017). *The science behind the mi-safe tool* [Web Page]. Retrieved from https://publicwiki.deltares.nl/display/OET/The+Science+behind+the+MI-SAFE+tool

Fenneman, N. (1902). Development of the profile of equilibrium of the subaqueous shore terrace [Journal Article]. *The Journal of Geology*, *X*(1), 1-32. doi: 10.1086/620977

Flemming, B. W. (2011). 3.02 - geology, morphology, and sedimentology of estuaries and coasts [Book Section]. In E. Wolanski & D. McLusky (Eds.), *Treatise on estuarine and coastal science* (p. 7-38). Waltham: Academic Press. Retrieved from http://www.sciencedirect.com/science/article/pii/B9780123747112003028 doi: 10.1016/B978-0-12-374711-2.00302-8

García-Rubio, G., Huntley, D., & Russell, P. (2015). Evaluating shoreline identification using optical satellite images [Journal Article]. *Marine Geology*, *359*, 96-105. doi: 10.1016/j.margeo.2014.11.002

Gorelick, N., Hancher, M., Dixon, M., Ilyushchenko, S., Thau, D., & Moore, R. (2017). Google earth engine: Planetary-scale geospatial analysis for everyone [Journal Article]. *Remote Sensing of Environment*, *202*, 18-27. doi: 10.1016/j.rse.2017.06.031

Guillén, J., & Jiménez, J. A. (1995). Processes behind the longshore variation of the sediment grain size in the ebro delta coast [Journal Article]. *Journal of Coastal Research*, *11*, 205-2018.

Hagenaars, G. (2017). *Accuracy assessment of coastline dynamics based on satellite images* (Thesis).

Hagenaars, G., de Vries, S., Luijendijk, A. P., de Boer, W. P., & Reniers, A. J. H. M. (2018). On the accuracy of automated shoreline detection derived from satellite imagery: A case study of the sand motor mega-scale nourishment [Journal Article]. *Coastal Engineering*, *133*, 113-125. doi: 10.1016/j.coastaleng.2017.12.011

Hasaki Oceanographical Research Station (HORS). (n.d., 2018). *Beach profiles, water levels, wave characteristics & sediment characteristics* [Dataset].

Hinkel, J., Nicholls, R. J., Tol, R. S. J., Wang, Z. B., Hamilton, J. M., Boot, G., … Klein, R. J. T. (2013). A global analysis of erosion of sandy beaches and sea-level rise: An application of diva [Journal Article]. *Global and Planetary Change*, *111*, 150-158. doi: 10.1016/j.gloplacha.2013.09.002

Hoepffner, N., & Zibordi, G. (2009). Remote sensing of coastal waters [Book Section]. In J. H. Steele (Ed.), *Encyclopedia of ocean sciences (second edition)* (p. 732-741). Oxford: Academic Press. doi: 10.1016/B978-012374473-9.00801-8

Holland, K. T., & Holman, R. A. (1996). Field observations of beach cusps and swash motions [Journal Article]. *Marine Geology*, *134*(1), 77-93. doi: 10.1016/0025-3227(96)00025-4

Huisman, B. (2019). *On the redistribution and sorting of sand at nourishments* (doctoral thesis). doi: 10.4233/uuid:a2bbb49d-8642-4a32-b479-4f0091f2d206

IPCC. (2019). Summary for policymakers [Book Section]. In H. Pörtner et al. (Eds.), *Ipcc special report on the ocean and cryosphere in a changing climate.* Author.

Kelly, J. T., & Gontz, A. M. (2018). Using gps-surveyed intertidal zones to determine the validity of shorelines automatically mapped by landsat water indices [Journal Article]. *International Journal of Applied Earth Observation and Geoinformation*, *65*, 92-104. doi: 10.1016/j.jag.2017.10.007

Kim, H., Hall, K., Jin, J.-Y., Park, G.-S., & Lee, J. (2014). Empirical estimation of beach-face slope and its use for warning of berm erosion [Journal Article]. *Journal of Measurements in Engineering*, *2*(1), 29-42.

King, C. A. M., & Mather, P. M. (1972). Spectral analysis applied to the study of time series from the beach environment [Journal Article]. *Marine Geology*, *13*(2), 123-142. doi: 10.1016/0025-3227(72)90050-3

Komar, P. D. (1998). *Beach processes and sedimentation* [Book]. Prentice Hall.

Komar, P. D., & McDougal, W. G. (1994). The analysis of exponential beach profiles [Journal Article]. *Journal of Coastal Research*, *10*, 59-69.

Kriebel, D. L., Kraus, N. C., & Larson, M. (1991). Engineering methods for predicting beach profile response [Conference Paper]. In *Coastal sediments '91: A specialty conference on quantitative approaches to coastal sediment processes* (p. 557-571). American Society of Civil Engineers.

Lee, P. (1994). The submarine equilibrium profile : a physical model [Journal Article]. *Journal of Coastal Research*, *10*(1).

Leu, D. J. (1977). Visible and near — infrared reflectance of beach sands: A study on the spectral reflectance/ grain size relationship [Journal Article]. *Remote Sensing of Environment*, *6*(3), 169-182. doi: 10.1016/0034-4257(77)90002-5

Luijendijk, A., Hagenaars, G., Ranasinghe, R., Baart, F., Donchyts, G., & Aarninkhof, S. (2018). The state of the world's beaches [Journal Article]. *Scientific Reports*, *8*(1), 6641. doi: 10.1038/s41598-018-24630-6

Madsen, A. J., & Plant, N. G. (2001). Intertidal beach slope predictions compared to field data [Journal Article]. *Marine Geology*, *173*(1), 121-139. doi: 10.1016/S0025-3227(00)00168-7

McFall, B. C. (2019). The relationship between beach grain size and intertidal beach face slope [Journal Article]. *Journal of Coastal Research*, *In-Press*. doi: 10.2112/JCOASTRES-D-19-00004.1

McFeeters, S. K. (1996). The use of the normalized difference water index (ndwi) in the delineation of open water features [Journal Article]. *International Journal of Remote Sensing*, *17*(7), 1425-1432. doi: 10.1080/01431169608948714

McGranahan, G., Balk, D., & Anderson, B. (2007). The rising tide: assessing the risks of climate change and human settlements in low elevation coastal zones [Journal Article]. *Environment and Urbanization*, *19*(1), 17-37. doi: 10.1177/0956247807076960

McLean, R. F., & Kirk, R. M. (1969). Relationships between grain size, size-sorting, and foreshore slope on mixed sand - shingle beaches [Journal Article]. *New Zealand Journal of Geology and Geophysics*, *12*(1), 138-155. doi: 10.1080/00288306.1969.10420231

Murray, N. J., Phinn, S. R., Clemens, R. S., Roelfsema, C. M., & Fuller, R. A. (2012). Continental scale mapping of tidal flats across east asia using the landsat archive [Journal Article]. *Remote Sensing*, *4*(11), 3417. doi: 10.3390/rs4113417

Murray, N. J., Phinn, S. R., DeWitt, M., Ferrari, R., Johnston, R., Lyons, M. B., ... Fuller, R. A. (2019). The global distribution and trajectory of tidal flats [Journal Article]. *Nature*, *565*(7738), 222-225. doi: 10.1038/s41586-018-0805-8

Nicholls, R., Wong, P., Burkett, V., Codignotto, J., Hay, J., McLean, R., ... Saito, Y. (2007). Coastal systems and low-lying areas [Book Section]. In C. Intergovernmental Panel on Climate (Ed.), *Climate change 2014 – impacts, adaptation and vulnerability: Part a: Global and sectoral aspects: Working group ii contribution to the ipcc fifth assessment report: Volume 1: Global and sectoral aspects* (Vol. 1, p. 361-410). Cambridge: Cambridge University Press. doi: 10.1017/CBO9781107415379.010

N. J. Cooper Beng, P., BSc, J. L., & P. Lowe Bsc, J. (2000). Beach-profile measurement, theory and analysis: Practical guidance and applied case studies [Journal Article]. *Water and Environment Journal*, *14*(2), 79-88. doi: 10.1111/j.1747-6593.2000.tb00231.x

Rector, R. L. (1954). *Laboratory study of equilibrium profiles of beaches* [Book]. US Beach Erosion Board.

Reis, A. H., & Gama, C. (2010). Sand size versus beachface slope — an explanation based on the constructal law [Journal Article]. *Geomorphology*, *114*(3), 276-283. doi: 10.1016/j.geomorph.2009.07.008

Rijkwaterstaat, Provincie Zuid-Holland, & EcoShape. (n.d., 2011-2018). *Zandmotor data* [Dataset]. TU Delft. doi: 10.4121/collection:zandmotor

Roelvink, D., & Reiniers, A. (2011). *A guide to modeling coastal morphology* (Vol. 12) [Book]. doi: 10.1142/7712

Rousseeuw, P. J., & van Driessen, K. (2006). Computing lts regression for large data sets [Journal Article]. *Data Mining and Knowledge Discovery*, *12*(1), 29-45. doi: 10.1007/s10618-005-0024-4

Sagar, S., Roberts, D., Bala, B., & Lymburner, L. (2017). Extracting the intertidal extent and topography of the australian coastline from a 28year time series of landsat observations [Journal Article]. *Remote Sensing of Environment*, *195*, 153-169. doi: 10.1016/j.rse.2017.04.009

Seto, K. C., & Shepherd, J. M. (2009). Global urban land-use trends and climate impacts [Journal Article]. *Current Opinion in Environmental Sustainability*, *1*(1), 89-95. doi: 10.1016/j.cosust.2009.07.012

Stauble, D. K. (1992). *Long-term profile and sediment morphodynamics: Field research facility case history* (Report No. CERC-92-7). Coastal Engineering Research Center.

Sunamera, T. (1975). “static” relationship among beach slope, sand size, and wave properties [Journal Article]. *Geographical Review of Japan*, *48-7*, 485 489.

Sunamura, T. (1984). Quantitative predictions of beach-face slopes [Journal Article]. *GSA Bulletin*, *95*(2), 242-245. doi: 10.1130/0016-7606(1984)95⟨242:QPOBS⟩2.0.CO;2

U.S. Army Engineer Research, Coastal Development Center, & Hydraulics Laboratory, Field Research Facility, Duck, North Carolina. (n.d., 1977-2019). *Beach profiles, water levels, wave characteristics & sediment characteristics* [Dataset]. Retrieved from https://frfdataportal.erdc.dren.mil/

Vos, K., Harley, M. D., Splinter, K. D., Simmons, J. A., & Turner, I. L. (2019). Sub-annual to multi-decadal shoreline variability from publicly available satellite imagery [Journal Article]. *Coastal Engineering*, *150*, 160-174. doi: 10.1016/j.coastaleng.2019.04.004

Wilson, A., & Jetz, W. (2016). Remotely sensed high-resolution global cloud dynamics for predicting ecosystem and biodiversity distributions [Journal Article]. *PLoS Biology*, *14*(3). doi: 10.1371/journal.pbio.1002415

Work, P. A., & Dean, R. G. (1991). Effect of varying sediment size on equilibrium beach profiles [Conference Paper]. In *Coastal sediments '91: A specialty conference on quantitative approaches to coastal sediment processes.*

Xu, H. (2006). Modification of normalised difference water index (ndwi) to enhance open water features in remotely sensed imagery [Journal Article]. *International Journal of Remote Sensing*, *27*(14), 3025-3033. doi: 10.1080/01431160600589179

Appendices

A Background on Satellite Imagery

Earth observation is the gathering of information of our planet. When this is done using space-borne sensors it is referred to as satellite imagery. This appendix covers the most important concepts in satellite imagery and will give background on the Copernicus programme and the Sentinel-2 mission in particular. Furthermore, it shows how multispectral satellite imagery can be used to extract the intertidal beach slopes on a global scale.

A.1 A short history of earth observation

Earth observation started shortly after the invention of photography. Realising the potential of earth observation, early reasearchers attached cameras to balloons to create the first-ever aerial photography in the 1840s. Aerial photography really took off with the invention of the airplane and played an important role during the first and second world war.

The launch of Sputnik 1 (1957), the world's first artificial satellite, changed earth observation forever. Only a few years later the first meteorological satellite was launched marking the start of satellite remote sensing.

Satellites are carrying increasingly sophisticated instruments to observe the Earth, far beyond the visible spectrum. Currently there are over 700 earth observing satellites in orbit with numerous applications including:

- Weather forecasting
- Wildlife conservation
- Agriculture
- Resource management
- Natural disaster response
- Climate science

A.2 Monitoring the coastal zone

Satellite research for coastal monitoring is emerging, thanks to the increased convenience of analysing satellite imagery. Coastal satellite science mainly focusses on imagery from the American Landsat programme and the European Copernicus programme. Their open data policy means that images are freely available and provide worldwide coverage.

In this study images from the Sentinel-2 mission (part of the Copernicus programme) are analysed, because of the relatively high spatial and temporal resolution.

A.3 Copernicus programme

The Copernicus programme is an earth observation programme from the European Union (European Space Agency, 2015). It is a cooperation between the European commission and the European Space Agency (ESA). It's mission is to provide strategic, social, economic and environmental benefits to European public authorities and to the civil society.

The Copernicus programme builds upon six dedicated families of satellites called the Sentinels. The Sentinels have different functions and are equipped with different sensors:

Sentinel-1 provides all-weather, day and night radar imagery for land and ocean services.

Sentinel-2 provides high-resolution optical images for land services.

Sentinel-3 provides high-accuracy optical, radar and altimetry data for marine and land service.

Sentinel-4 provides monitoring of the atmospheric composition.

Sentinel-5 provides monitoring of the atmospheric composition.

Sentinel-6 provides high-accuracy altimetry data.

Previous research by Donchyts (2018); García-Rubio et al. (2015); Hagenaars et al. (2018) has proven the capabilities of optical images for delineating shorelines by detecting the water/land interface. The methodology for extracting the Satellite Derived Shoreline (SDS) from multispectral satellite imagery is described in appendix C.

A.4 Sentinel-2

The Sentinel-2 family is a constellation of two polar-orbiting satellites. They are equipped with the Multispectral Instrument (MSI) for capturing images in the optical and infrared range. They have a high revisit time of 5 days at the equator.

A.4.1 The Multispectral Instrument

Satellite images are pixel based geospatial data sets. Light intensities are recorded by the MSI aboard the Sentinel-2 satellites. Multispectral data is acquired in 13 different bands; each band is sensitive to different wavelengths. The MSI captures information in the optical and infrared wavelengths.

Sentinel-2 images are made up of 13 dedicated bands. The data in each band is recorded separately; the different bands have pixel sizes ranging from (10 to 60) metres. The following table provides an overview of the different bands in the MSI:

Band	Description	Pixel size
B1	Coastal aerosol	60 m
B2	Blue	10 m
B3	Green	10 m
B4	Red	10 m
B5	Vegetation red edge	20 m
B6	Vegetation red edge	20 m
B7	Vegetation red edge	20 m
B8	NIR	10 m
B8A	Narrow NIR	20 m
B9	Water Vapour	60 m
B10	Cirrus	60 m
B11	SWIR	20 m
B12	SWIR	20 m

A.4.2 Data products

Sentinel-2 products are freely available due to the ESA free and open data policy. Distinction is made between various product levels:

Level 0 is the raw image data. It is unavailable to the public.

Level 1A is obtained by decompressing the level 0 raw image data. It is unavailable to the public.

Level 1B product is obtained by rediometrically correcting detector variations.

Level 1C products are geometrically corrected for the earth's rotation and satellite orbit and are orthorectified using a digital elevation model (DEM). The level 1C product provides top of atmosphere (TOA) reflectances. These are available in Google Earth Engine (GEE) for analysing.

Level 2A product provides Bottom Of Atmosphere (BOA) reflectances by correcting for atmosphere variations.

The distinction between the TOA and BOA reflectances is made because light waves are modified by the earth's atmosphere. The TOA reflectance images are selected for this study as they have proven to be sufficient for the identification of water and land pixels and they provide a standardised comparison between images acquired on different dates (Vos et al., 2019).

The Sentinel-2 data products are a compilation of granules. The granules, also called tiles, are 100×100 km^2 orthorectified images. Figure A.1 shows that the tiling grid has overlapping sections.

A.4.3 Low Earth orbit

The Sentinel-2 satellites are in a sun-synchronous orbit. That is a nearly polar orbit, in which it passes over any given point of the Earth's surface at the same local mean solar time. This has some advantages for earth observation missions, as this means that the imagery shows consistent lighting conditions. The Sentinel-2 satellites are 180 degrees out of face and pass over the equator at 10:30 (am) mean solar time. This value of mean local solar time was chosen as a compromise between a suitable level of solar illumination and the minimisation of potential cloud cover.

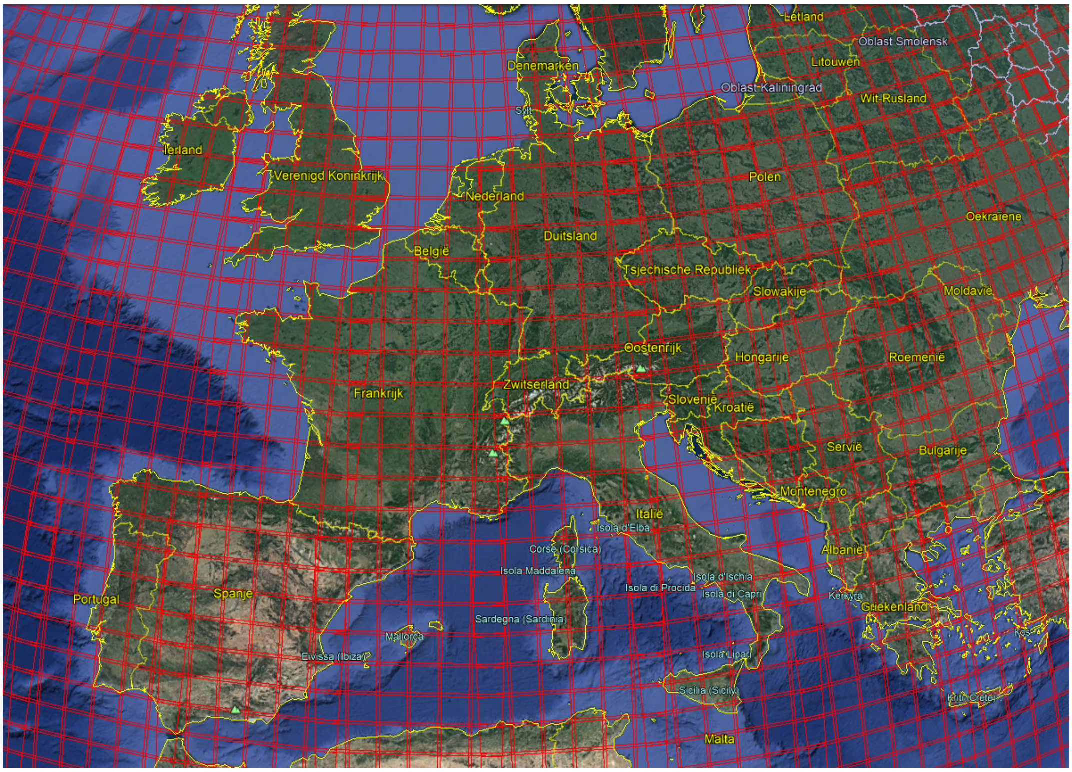

Figure A.1: The Sentinel-2 tiling grid consists of 100×100 km^2. This map shows the tiling grid over Europe. Each tile has an identification number. Note that Sentinel-2 only acquires data over land regions.

The Sentinel-2 constellation orbits at an altitude of 786 km, where it cycles the earth in 10 days. This means that the revisit time is only 5 days. Especially towards the poles where orbit trajectories are closer together images are overlapping. This means that there may be more images than once per 5 days.

B Describing the Shape of the Beach

This appendix is a standalone chapter providing background on the shape of the beach. The equilibrium beach profile as a method of describing the state of the beach is explained in depth. Several beach profile models are discussed in B.2. The beach face, the most dynamic section of the beach profile, is studied in more detail, see paragraph B.3.

B.1 The Shape of the beach

The coastal system is an extremely complex environment: wind, waves and currents continuously move sediment around so that the shape of the beach continuously changes. The shape of the beach is most commonly described by the *beach profile*: "the cross-sectional trace of the beach perpendicular to the high tide shoreline, extending from the backshore cliff or dune to the inner continental shelf or a location where waves and currents do not transport sediment to and from the beach".

Figure B.1 shows a graphic representation of a beach profile and points out the most important definitions:

Bar elongated sand body created by currents or by waves.

Beach zone of unconsolidated material that extends from the (low-water) shoreline to the dunefoot or the line of permanent vegetation.

Beach face seaward section of the beach which is exposed to and shaped by the action of the waves.

Inshore part of the active coastal zone situated below the low water line.

Intertidal zone area of the shore within the tidal range. In other words, it is the area that is above water level at low tide and underwater at high tide. The intertidal zone is often synonymous with the beach face; in this thesis it is used to point out the same area as the beach face.

Shoreline boundary line between land and water.

B.2 The Equilibrium Beach Profile

In general beach profiles are steepest at the shoreline and have a progressively decreasing slope as the water depth increases in the offshore direction (Komar & McDougal, 1994). This has led to the development of several equilibrium beach profile models. The equilibrium beach profile is mainly a theoretical concept for describing the form of the profile. A truly equilibrium morphology can only be achieved in a laboratory

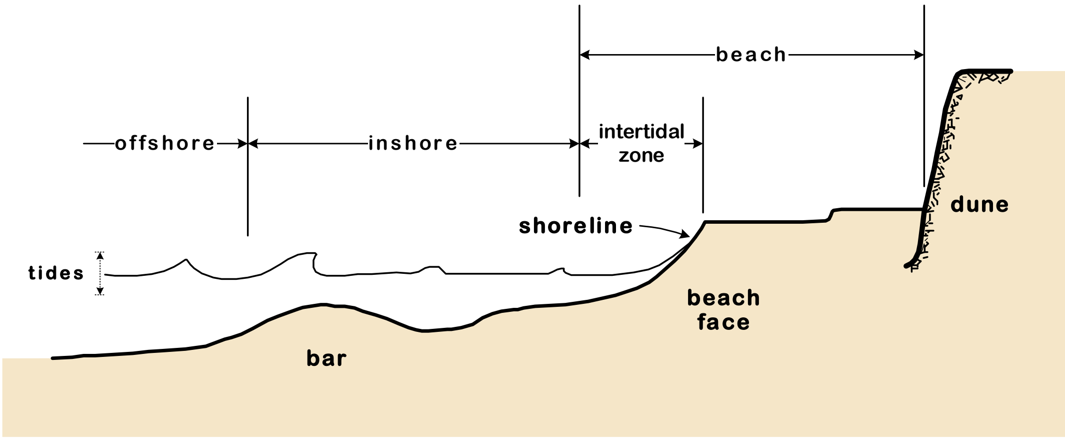

Figure B.1: Terminology of the beach profile.

wave tank where waves of constant height and period are maintained (Komar, 1998). Such conditions seldom, if ever, occur in nature so that the beach profile is always evolving.

Due to the many variables involved, quantitative predictions of the beach slopes are remote (Sunamura, 1984). Most models aim at capturing the basic shape of the profile without the deviant shapes such as bars and troughs. Moreover, they only describe the underwater section of the profile.

Over the years, a large number of equilibrium beach profile models have been developed (Komar, 1998), such as the Bruun profile (Bruun, 1954; Dean, 1977; Kriebel et al., 1991; Work & Dean, 1991), the exponential profile (Bodge, 1992; Komar & McDougal, 1994), the logarithmic profile (Lee, 1994) and the 2-step equilibrium profile (Bernabeu et al., 2002). The exponential profile and the logarithmic profile use empirical constants. This means that they cannot be applied in a prognostic manner; only in a descriptive manner (Dean, 2008). The reason for studying equilibrium beach profiles in the context of this research is for their predictive values. Therefore, only the Bruun model and the 2-step equilibrium beach profile are elaborated on.

B.2.1 Bruun model

One of the first to develop a beach profile expression was Bruun (1954). Based on his research at the Denmark cost he found that the beach profile can be described by a basic power function with the general form:

$$h = A \cdot x^{\rho} \quad \text{with} \quad \rho = 2/3 \tag{B.1}$$

Figure B.2 gives a general impression of the shape of the model. h is the water depth, A is the shape factor and x is the distance from the shoreline. The value of 2/3 was later theoretically motivated by Dean (1977) assuming a constant shear stress at the bottom along the profile. Due to simple shape it is often used for engineering (Kriebel et al., 1991).

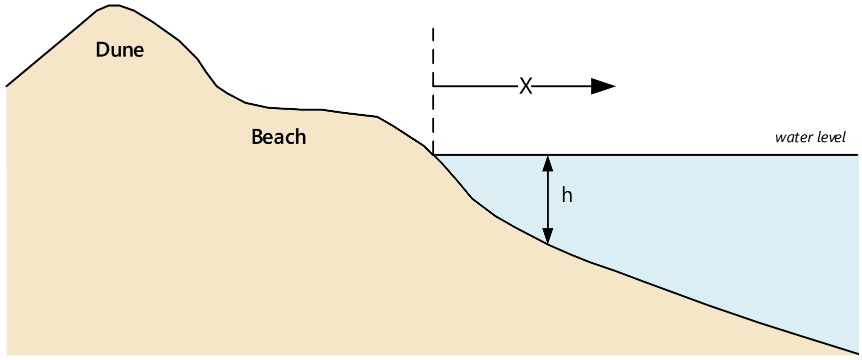

Figure B.2: Bruun/Dean equilibrium beach profile

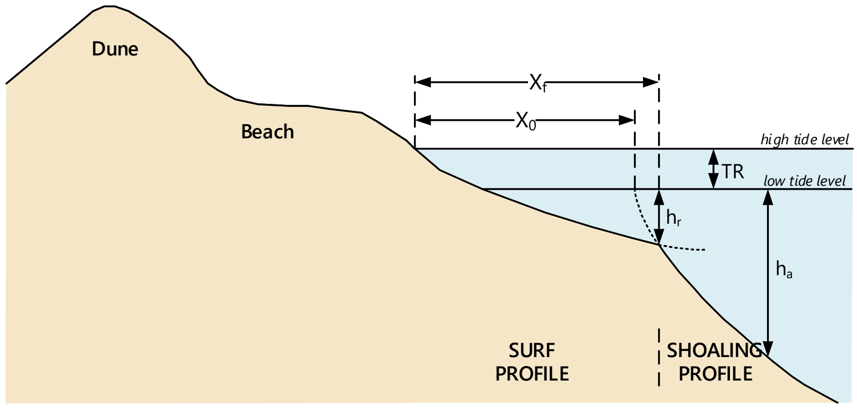

Figure B.3: 2-Step Equilibrium Beach Profile

Bruun determined the value of the shape factor A empirically based on the best fit to the measured profile. Further research by Dean (1977); Kriebel et al. (1991); Work & Dean (1991) related the parameter A to wave and sediment characteristics:

$$A = 2.25 \left(\frac{w_f^2}{g} \right)^{2/3} \quad \text{with} \quad w_f = \frac{16.17 d50^2}{1.8 \cdot 10^{-5} + \sqrt{12.1275 d50^3}} \tag{B.2}$$

w_f is the sediment fall velocity, which is proportional to the grain size. Work & Dean (1991) showed that including additional parameters, like cross-shore distribution of median sediment size, did not significantly improve the goodness-of-fit. This indicates that the simpler approach, with A constant, already gives a good fit.

The main criticism on the Bruun profile is related to the dimensionality of A ($m^{1/3}$) and the infinite slope at the shoreline (Komar, 1998). Since the shape parameter (equation B.2) does not include an influence from wave characteristics, the Bruun profile is not able to explain seasonality.

B.2.2 2-Step equilibrium beach profile

Most equilibrium beach profiles, including the Bruun profile, relate the beach morphology solely to the grain size. Bernabeu et al. (2002) propose a profile that incorporates the tidal influence on the beach morphology. Figure B.3 shows the profile shape which, as the name suggests, consist of two steps: a surf profile and a shoaling profile.

Starting point of the formulation is that the location of wave breaking continuously changes throughout the tidal cycle. Assumed is that energy dissipation in the shoaling zone is dominated by bottom friction and energy dissipation in the surf zone is dominated by turbulence:

$$\text{Surf profile :} \qquad x = \left(\frac{h}{A}\right)^{3/2} + \frac{B}{A^{3/2}} h^3 \tag{B.3}$$

$$\text{Shoaling profile :} \qquad X = x - x_0 = \left(\frac{h}{C}\right)^{3/2} + \frac{D}{C^{3/2}} h^3 \tag{B.4}$$

x is the distance from the shoreline, h is the water depth and the coefficients $A, B, C \& D$ are shape parameters. They are given by:

$$\begin{aligned} A &= (0.32 - 0.02\Omega_{sf}) \\ B &= 0.89 \exp\left[-1.24\Omega_{sf}\right] \\ C &= (0.06 + 0.04\Omega_{sf}) \\ D &= 0.22 \exp\left[-0.83\Omega_{sf}\right] \end{aligned}$$

Ω is the dimensionless sediment fall velocity: $\Omega = H/\omega T$. The 2-Step equilibrium beach profile resolves the main concerns of the Bruun profile, but is more difficult to apply due to increased number of parameters.

B.3 The Beach Face

The beach face is the most dynamic section of the beach profile: it is the section where swash processes are dominant. The beach face immediately responds to changing conditions: with more energetic waves the slope instantaneously becomes milder and in calm conditions the slope returns to a steeper equilibrium. Although a lot of research has been put into understanding the dynamics of the beach face, the detailed processes are not fully understood. Sunamura (1984) identifies 5 factors that influence the slope of the beach face:

1. Beach sediment characteristics (grain size, degree of sorting, size distribution)
2. Wave properties (wave height, wave steepness, swash period)
3. Groundwater level
4. Tidal stages
5. Longshore current velocity

Sunamura found that sediment grain size, wave height, and wavelength are the crucial factors. The slope of the beach face is primarily governed by the asymmetry in the intensity of the swash up-rush versus the backwash (Komar, 1998).

B.3.1 Dynamics of the beach face

The following overview shows the factors influencing the beach face slope (based on Sunamura, 1984):

- **Beach sediment characteristics**

Grain size	↑	-	↑	Beach face slope
Degree of sorting	↑	-	↑	Beach face slope
Specific gravity	↑	-	↑	Beach face slope

- **Wave properties**

Wave height	$\uparrow$ - $\downarrow$	Beach face slope
Wave steepness	$\uparrow$ - $\downarrow$	Beach face slope
Swash period	$\uparrow$ - $\downarrow$	Beach face slope

- **Groundwater level**

Groundwater level	$\uparrow$ - $\downarrow$	Beach face slope

- **Tidal stages**

Tidal level	$\uparrow$ - $\uparrow$	Beach face slope

- **Longshore current velocity**

Longshore current velocity	$\uparrow$ - $\uparrow$	Beach face slope

B.3.2 Beach face slope relations

Several relations for the beach face slope have been established using the general correlations between the variables. Since the processes involved are not fully understood only empirical relations are available. An extraordinary emphasis has been placed on sandy coasts however (Bujan et al., 2019) so that most relations are not valid for the whole range of sediment sizes encountered in the coastal environment. Bujan et al. (2019) concluded this after a careful analysis of 2144 measurements. Figure B.4 provides an overview of the formulations included in the study.

Rector (1954)

Rector conducted measurements in a wave flume to study the equilibrium beach profile. The experiments were performed in a controlled laboratory setting with uniform wave action. He found the following relation for the slope of the beach face:

$$\tan\beta = c_1 \frac{(d50/(1000L))^{c_2}}{(H_s/L)^{c_3}} \quad \text{with} \quad c_1 = 0.07; c_2 = 0.1; c3 = 0.42 \tag{B.5}$$

$\tan\beta$ is the slope of the beach face, $d50$ is the median grain size, L is the offshore wave length and H_s is the offshore significant wave height. $c_1, c_2 \& c_3$ are empirical constants. The formulation is valid for medium to very coarse sands.

Sunamera (1975)

In addition to a laboratory study, Sunamera (1975) also studied data from field campaigns along the Japanese and Californian coast. Focus was placed on the grain size and wave characteristics as these factors were deemed dominant. Sunamera obtained the following relation for the field measurements:

$$\tan\beta = c_1 \frac{T\sqrt{gd50}}{H_b} \quad \text{with} \quad c_1 = 0.1 \tag{B.6}$$

$\tan\beta$ is the slope of the beach face, T is the wave period, $d50$ is the median grain size and H_b is the breaker wave height. The formulation is based on a limited number of field measurements and is only applicable for medium to coarse sand beaches.

Sunamura (1984)

Continuing his research, Sunamura studied field observations from the British, Japanese and United States Pacific coast. An empirical relation between the beach

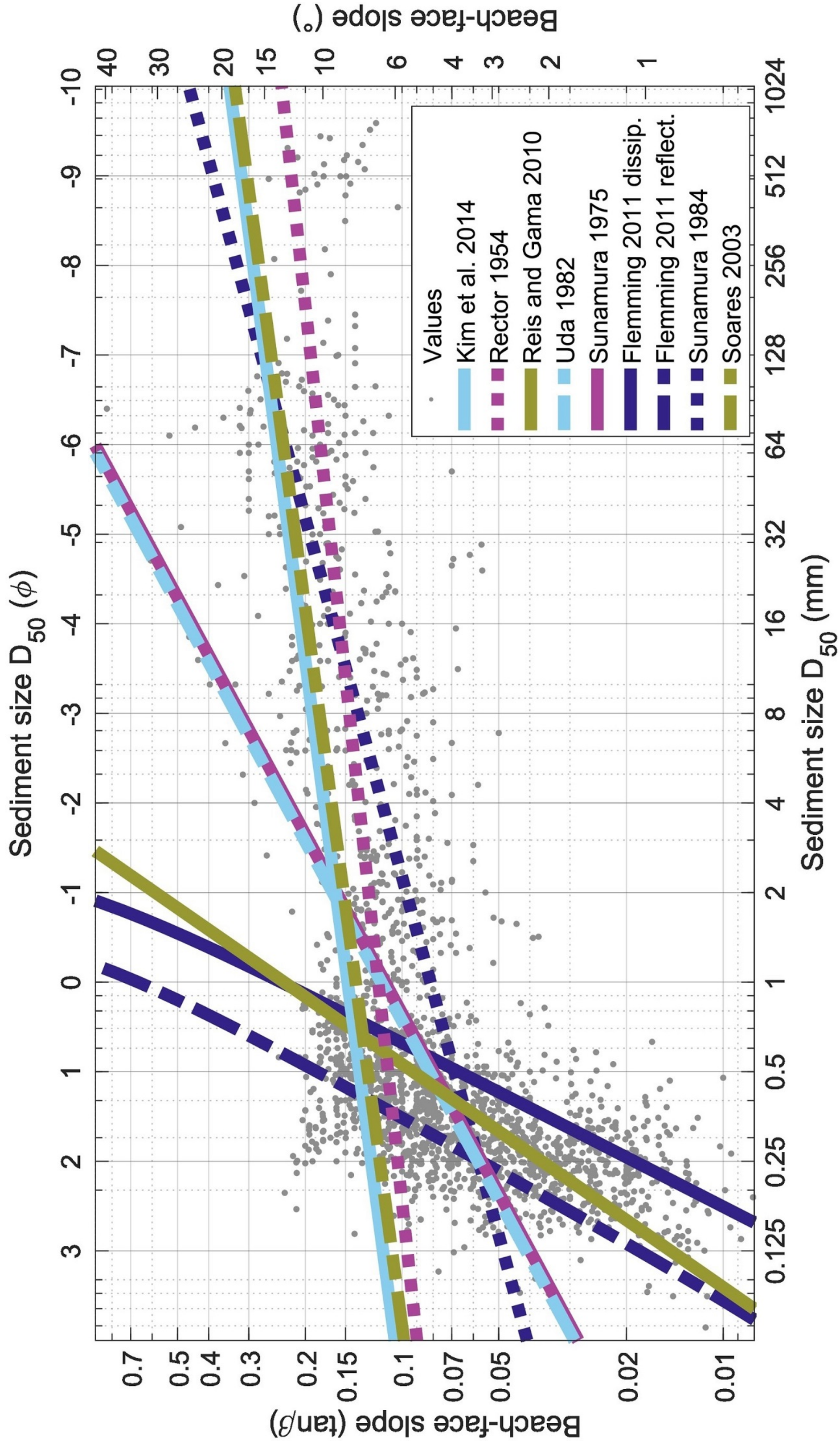

Figure B.4: Overview of the existing beach face relations. The most recent methods are not included. (Bujan et al., 2019) face slope and the sediment size at the beach was obtained based on the new data:

$$\tan\beta = \frac{c_1}{\sqrt{H_b/g^{0.5}d50^{0.5}T}} \quad \text{with} \quad c_1 = 0.12 \tag{B.7}$$

$$H_b = 0.399^{0.2}\left(TH_0^2\right)^{0.4} \tag{B.8}$$

$\tan\beta$ is the slope of the beach face, H_b is the breaker wave height, $d50$ is the median grain size and T is the wave period. The breaker wave height can be derived using equation (B.8).

Sunamura (1984) is unclear which wave conditions must be used. Madsen & Plant (2001) provided two interpretations:

- The slope refers to the steady-state slope. This means that the steady-state wave conditions must be applied.
- The slope refers to the average beach face slope. This means that the average wave conditions must be applied.

In this thesis the beach face slope is derived from satellite imagery. Multiple images are combined so the analysis period should be expressed in days, weeks or months, whereas the response time is much shorter. Thus, it is evident that there is no steady-state, so in thesis the average conditions are considered. Making use of that assumption the average grain size ($d50$) can be estimated using equation (B.7). (B.7) was developed for median to coarse sand beaches.

Reis & Gama (2010)
In an analysis of field experiments along the southwest coast of Portugal an expression was found for the slope of the beach face:

$$\tan\beta = c_1 H_s^{c_2} d50^{c_3} \quad \text{with} \quad c_1 = 0.9; c_2 = -2.33; c_3 = 1.33 \tag{B.9}$$

$\tan\beta$ is the slope of the beach face, H_s is the significant wave height and $d50$ is the median grain size. The 102 pairs of data include samples from beaches with medium to very coarse sands.

Flemming (2011)
Flemming found that there is a correlation between the beach face slope and the beach state. Such a correlation is obvious because reflective beaches are characterised by a steep nearshore zone and dissipative beaches have a relatively flat nearshore zone. He found the following expression where Φ_{50} is the median grain diameter along the ϕ scale:

$$\tan\beta = \tan\left(c_1 + c_2\exp\left(-\Phi_{50}/c_3\right)\right) \quad \text{with:} \quad \Phi_{50} = -^2\log d50 \tag{B.10}$$

Dissipative beach state :	with	$c_1 = 0;$	$c_2 = 13.39;$	$c_3 = 0.7954$
Reflective beach state :	with	$c_1 = 0.057;$	$c_2 = 33.5152;$	$c_3 = 0.8517$

The relation above is only validated for fine to coarse sand beaches.

Kim et al. (2014)

Unsatisfied with Sunamura's and Reis & Gama's equations, Kim et al. proposes a new empirical relation to predict the slope of the beach face. The independent variables are the wave period and the bed sediment grain size, as is shown here:

$$\tan\beta = c_1 T^{c_2} d50^{c_3} \quad \text{with} \quad c_1 = 0.332; c_2 = -0.416; c_3 = 0.122 \tag{B.11}$$

$\tan\beta$ is the slope of the beach face, T is the wave period and $d50$ is the median grain size. The coefficients are obtained from multiple linear regression using data from three flume experiments with medium to coarse sands (200 μm to 700 μm)

Bujan et al. (2019)

Recently, Bujan et al. (2019) and McFall (2019) independently developed an exponential relation between sediment size and beach face slope. The beach face slope formulation found by Bujan et al. (2019) is given in equation B.12. The reason for the development of this relation is the limited application of other models: an extraordinary emphasis was placed on sandy coasts (see figure B.4). The models discussed before are not valid over the whole range of sediment sizes encountered in the coastal environment.

The research uses a huge data set of 2144 measurements of beach face slope and associated grain sizes. The samples are collected from beaches worldwide, covering the range from very fine sand to boulders. The analysis shows that the correlation between beach face slope and grain size has an exponential shape:

$$\text{Slope} = a_4\,(d50 - 0.125)^{b_4} + c_4 \tag{B.12}$$

$$\text{with} \quad a_4 = -0.154; b_4 = -0.145; c_4 = 0.268$$

$\tan\beta$ is the slope of the beach face, $d50$ is the median grain size and $a_4; b_4; \& c_4$ are scale parameters based on a best fit on the analysed beaches. Despite the limited number of input parameters, the relation provides good agreement for all sediment sizes.

McFall (2019)

Simultaneous to the work of Bujan et al. (2019), McFall developed an exponential beach face relation (B.13;B.14;B.15) intended to understanding the expected behaviour of the beach face slope. Similarly, data from beaches worldwide (181 beaches) are collected and the relation is found empirically.

McFall found that the beach face responds different in different coastal environments. Three regimes are distinguished based on the wave height that is exceeded 12 hours per year:

- $H_{s,12} > 3m$: Exposed
- $1m < H_s < 3m$: Moderately protected
- $H_{s,12} < 1m$: Protected

Each level of beach exposure has a different relation between the slope $(1/X)$ and the grain size (d):

$$\text{Protected}: \quad X = 3.1 d50^{-1.1} \tag{B.13}$$

$$\text{Moderately protected}: \quad X = 2.1 d50^{-1.8} \tag{B.14}$$

$$\text{Exposed}: \quad X = 3.9 d50^{-1.85} \tag{B.15}$$

The simplicity of the Bujan et al. (2019); McFall (2019) is what distinguishes these methods from the expression by Sunamura (1984), for example, where a thorough knowledge of the wave characteristics is required. Nevertheless these methods still perform well: the correlation coefficients for the McFall model are 0.87, 0.88 and 0.87 for protected, moderately protected and exposed beaches respectively.

C Guide to extracting shoreline features from satellite imagery

This appendix provides a summary of previous research by Donchyts (2018); Hagenaars (2017); Luijendijk et al. (2018) and others. This results in a comprehensive guide on extracting shoreline features from optical satellite imagery.

Satellite imagery has a wde number of applications; in the Coastal Engineering field it is mainly used for coastal monitoring. The use of satellite imagery for coastal monitoring really got off the ground after the launch of the Google Earth Engine , Google's platform for Earth science data and analysis, which took away all the IT pains related to analysing satellite imagery.

Satellite imagery for shore monitoring has large advantages, such as large spatial coverage, large temporal coverage, and consistent temporal resolution (aside from cloud covered images). Clearly, analysing satellite imagery to monitor shorelines has large advantages. However, Donchyts (2018) raises the issues of global objectivity, accuracy and applicability when it comes to identifying land and water pixels.

Extracting shoreline features from satellite imagery consists of three steps:

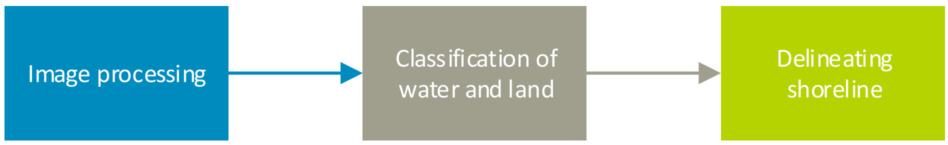

C.1 Image processing

The instrument aboard the satellite (the MSI for the Sentinel-2 family of satellites) captures the light intensities for specific wavelengths. These are called Digital Numbers. Several sensor corrections are applied by the administrator before the images are published. The public images (Level 1C) contain the top of atmosphere (TOA) reflectance values. These images are fit for analysis: it is possible to extract shoreline features from these images with no further image processing. A number of image processing techniques are listed here that can be applied for a specific purpose.

C.1.1 Georeferencing

The Level 1C product from the Sentinel-2 mission is already georeferenced. This means that the internal coordinate system of the image is related to the ground system of geographic coordinates. Georeferencing may be necessary when combining

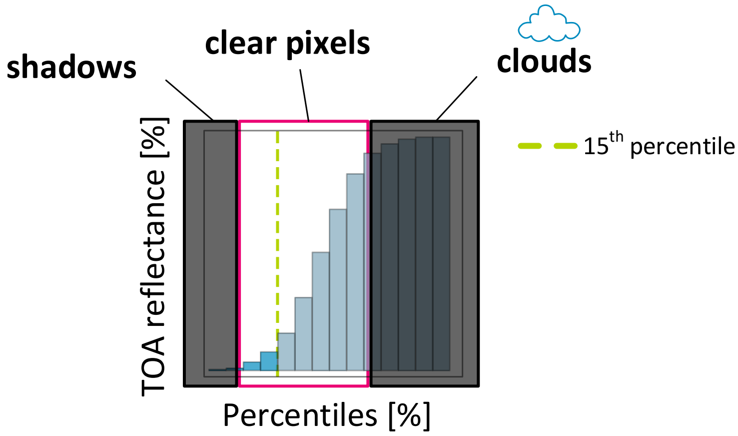

Figure C.1: Histogram of TOA reflectance values per pixel. The principle of compositing is that the lowest and highest reflectance values correspond to shadows and cloud respectively. The 15^{th} percentile results in clear pixels. Adopted from Hagenaars et al. (2018).

multiple sources of satellite imagery. In that case it is important that the coordinate systems from the different satellite missions match.

C.1.2 Atmospheric corrections

By taking the atmospheric conditions into account it is possible to convert the TOA reflectance to surface reflectance (or Bottom Of Atmosphere (BOA) reflectance). This may be required for time-series analysis. Hagenaars (2017) declared that the TOA reflectances are sufficient for the extraction of shoreline features.

C.1.3 Image compositing

Compositing is an image processing technique that is often used in optical satellite imagery to reduce inaccuracies in order to improve image quality (Hagenaars et al., 2018; Luijendijk et al., 2018). Examples of environmental related drivers of inaccuracy are cloud cover, waves and soil moisture.

Image compositing reduces a collection of satellite images (for example all images for a specific year) to a single image by calculating the pixel value based on all available pixels for that location. Common reduction techniques are the mean value, the median value or the 15th percentile of the underlying images. The last is illustrated in figure C.1.

A drawback of aggregating multiple satellite images into yearly composites is that it reduces the detection om smaller scale variability. Information on variability within the time sequence is lost.

C.1.4 Pansharpening

Pansharpening is an image processing technique that is often used in multispectral imagery to improve image quality. High-resolution panchromatic and lower-resolution multispectral are merged in the process to create a single high-resolution colour image. Pansharpened images sometimes contain spectral distortions as the panchromatic band has a different colour tone than the combination of colour bands.

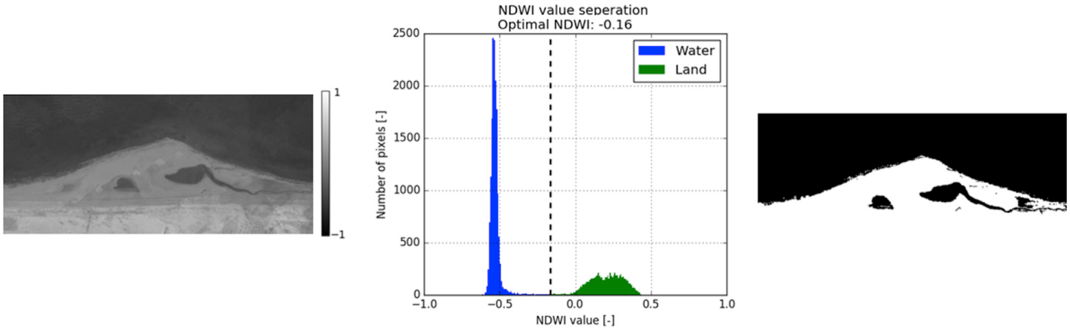

Figure C.2: *NDWI* greyscale image (left), *NDWI* histogram (middle) and resulting binary image (right). Adopted from Hagenaars et al. (2018).

The Sentinel-2 mission does not capture panchromatic data, so pansharpening is not applicable. The Landsat satellites are equipped with an instrument that captures panchromatic data so pansharpening is of added value. However, Hagenaars et al. (2018) did not find a significant improvement of the accuracy of Satellite Derived Shorelines (SDSs) by applying pansharpening.

C.2 Classification of water and non-water pixels

The main step in the analysis is the classification of water and non-water pixels. Classification means that every pixel is labelled as a land pixel or as a water pixel. Land and water can be differentiated using the reflectance properties of the different bands. For example: light in the near-infrared (NIR) wavelengths is absorbed in water, whereas it is reflected on the earth's surface. This is the starting point for classification based on index thresholding. Alternatively, machine learning algorithms are applied to distinguish water and land.

C.2.1 Unsupervised index thresholding

The basic premise in the unsupervised classification is that the pixels within a group should have a similar reflectance pattern: water pixels always 'look' different than land pixels. Spectral water indices try to find exactly that: a way of 'looking' so that water and land pixels can easily be distinguished.

Several spectral water indices have been developed over the years, the Normalised Difference Water Index (*NDWI*) (developed by McFeeters (1996)) is probably the best known. C.2.2 gives an overview of the spectral indices used for delineating shorelines. The *NDWI* is based on the green and NIR spectral bands: as water strongly absorbs light in the NIR range and reflects green light and land reflects light of both wavelengths, they can be differentiated. Figure C.2 shows how index-based classification works for a Sentinel-2 scene of the Sand Motor mega-nourishment in the Netherlands. Each pixel is assigned an *NDWI* value (between -1.0 and 1.0); the left figure shows the resulting grayscale image.

Therafter, the Otsu thresholding algorithm is used to determine the threshold value. The middle figure is a histogram of all the *NDWI* values. Two distinct peaks can be observed: one for water pixels, one for land pixels. The Otsu thresholding algorithm determines the optimal value to split the two peaks.

Pixels with an *NDWI* value smaller than a threshold value (in this example -0.16)

are associated with water and pixels with a higher value are classified as land. This results in a binary image where each pixel is either water or land. This is shown in the right figure. Other spectral indices can be applied similarly.

C.2.2 Spectral indices for water classification

The $NDWI$ is an enhancement technique for monitoring water content. It is the most common spectral index used to discriminate between water and land features, but there are many more indices available. Kelly & Gontz (2018) compared and assessed seven water indices for deriving shorelines: $NDWI$, $MNDWI$ (Xu, 2006), $NDVI$, TCW, $AWEI_{sh}$, $AWEI_{nsh}$, WI_{2015}. These indices are shown in the following overview:

$$NDWI = \frac{\lambda_{green} - \lambda_{NIR}}{\lambda_{green} + \lambda_{NIR}} \tag{C.1}$$

$$MNDWI = \frac{\lambda_{green} - \lambda_{SWIR1}}{\lambda_{green} + \lambda_{SWIR1}} \tag{C.2}$$

$$NDVI = \frac{\lambda_{NIR} - \lambda_{red}}{\lambda_{NIR} + \lambda_{red}} \tag{C.3}$$

$$\begin{aligned} TCW = {} & 0.0315\lambda_{blue} + 0.2021\lambda_{green} + 0.3102\lambda_{red} + 0.1594\lambda_{NIR} \\ & + 0.6806\lambda_{SWIR1} + 0.6109\lambda_{SWIR2} \end{aligned} \tag{C.4}$$

$$AWEI_{sh} = \lambda_{blue} + 2.5\lambda_{green} - 1.5\left(\lambda_{NIR} + \lambda_{SWIR1}\right) - 0.25\lambda_{SWIR2} \tag{C.5}$$

$$AWEI_{nsh} = 4\left(\lambda_{green} - \lambda_{SWIR1}\right) - \left(0.25\lambda_{NIR} + 2.75\lambda_{SWIR2}\right) \tag{C.6}$$

$$\begin{aligned} WI_{2015} = {} & 1.7204 + 171\lambda_{green} + 3\lambda_{red} - 70\lambda_{NIR} \\ & - 45\lambda_{SWIR1} - 71\lambda_{SWIR2} \end{aligned} \tag{C.7}$$

where λ_{blue}, λ_{green}, λ_{red}, λ_{NIR}, λ_{SWIR1} and λ_{SWIR2} are the pixel intensities in the blue band (0.46 to 0.53 μm), the green band (0.54 to 0.58 μm), the red band (0.65 to 0.68 μm), the near infrared band (0.78 to 0.89 μm), the first short-wave infrared band (1.57 to 1.66 μm) and the second short-wave infrared band (2.10 to 2.28 μm).

Kelly & Gontz (2018) validated the SDSs using these indices against GPS-surveyed intertidal beach zones. The Modified Normalised Difference Water Index ($MNDWI$) was found to be the best index for automated shoreline mapping based on its performance and threshold replicability. It does not require site-specific calibration and is thus fit for application on a global scale.

All indices have their own drawbacks. The $MNDWI$, for example, fails at detecting the difference between water and ice. On the other hand, wave foam in the surf zone distorts the $NDWI$.

C.2.3 Supervised machine learning classification

Although *NDWI* has been used extensively to monitor the intertidal zone (Luijendijk et al., 2018; Murray et al., 2012), it is affected by the white water near the land-water boundary (Bishop-Taylor et al., 2019). Hagenaars et al. (2018) concluded that this decreases the accuracy of SDSs with deviations in the order of 40 m. Machine learning classifiers are deployed to overcome these problems (Murray et al., 2019; Vos et al., 2019).

Machine learning relies on recognizing patterns in an abundance of data. Classification using machine learning uses labelled data, or 'training data', to find patterns, rather than using a predefined algorithm. Because training data are required, machine learning classifiers are referred to as supervised. This implies that machine learning algorithms are user-dependent and do not scale well (Hagenaars, 2017; Sagar et al., 2017).

In this research, preference is given to the use of an index-based classification algorithm in lieu of a machine learning classifier. The advantage of unsupervised thresholding is that it is possible to automate water detection in a user-independent way. Also, machine learning classifiers have the tendency to become a 'black box'.

C.3 Accuracy of the SDS position

Literature suggests that very high accuracies of the SDS position can be achieved in the absence of inaccuracies. Especially clouds and wave foam were found to be challenging with respect to an accurate detection of shorelines. Hagenaars et al. (2018) identified 6 sources of inaccuracy:

1. Cloud cover
2. Foam caused by waves
3. Soil moisture and grain size
4. Sensor corrections
5. Georeferencing
6. Image pixel resolution

C.3.1 Cloud cover and wave foam

Cloud cover forms a major challenge when analysing optical remote sensing data. Optical radiation is blocked by clouds, so they block the line of sight to the Earth's crest. Cloud detection algorithms, such as the FMask algorithm, have been developed to identify and mask clouds in the images. Unfortunately, the FMask algorithm is not available for Sentinel-2 scenes because thermal values are not recorded.

The reason cloud cover and wave foam are so problematic for the detection of shorelines is that they have similar reflectance properties to land (when using the *NDWI*). Therefore, these areas are mistakenly identified as non-water pixels.

As this research is not aimed at improving cloud detection, the fairly simple method of cloud masking using image metadata will be applied. The research will aim in finding the optimum between minimum cloud cover and a reasonable number of images. Fortunately, there is a large correlation between the presence of clouds and high wave action. Storms associated with the generation of waves are often accompanied by cloudy skies. Nonetheless, Hagenaars et al. (2018) shows that filtering on wave height (in addition to filtering on cloudcover metadata) can improve the accuracy of shoreline position.

C.3.2 SDS offset in a benchmark case

Hagenaars et al. (2018) determined the accuracy of the shoreline derivation algorithm using a benchmark case where all sources of inaccuracy were minimised. The best possible accuracy that can be achieved with Sentinel-2 images is 1.3 metres with a standard deviation of 5.1 metres. This is an incredible result, especially considering that the pixel resolution is 10 metres.

In a regular situation with clouds and waves present, there is a significant seaward bias of the SDS. The average offset was found to be 97.5 metres with a standard deviation of 300 metres. Clouds cover results in deviation of $\mathcal{O}200$ m; wave foam results in deviations of $\mathcal{O}40$ m.

D Example of the slope derivation from satellite imagery (Delfland coast)

In this appendix an example computation is worked out for the satellite derived slope at the Delfland coast. The FAST, Sagar and Onrust method are applied at JarKus transect 9011094 to derive the slope of the intertidal beach.

D.1 JarKus transect 9011094

This appendix shows an example of the intertidal slope derivation at JarKus transect 9011094at the Delfland coast in the Netherlands. The Delfland coast is a 17 km long sandy coast between Hook of Holland and Scheveningen. In 2011, the Sand Motor, a mega-nourishment, was constructed here. Figure D.1 shows a map of the study area.

D.2 Intertidal beach slopes derived from observed profiles

The intertidal beach slopes at the Delfland are not measured, but regular beach profile surveys are done. The observed slopes are derived from the beach profiles by fitting a linear model to the area between highest astronomical tide (HAT) + 0.5 m and lowest astronomical tide (LAT) - 0.5 m.

Figure D.1: Map of the Delfland Coast. The Delfland coast is a 17 km long sandy coast ranging from Hook of Holland in the southwest to Scheveningen in the northeast of the domain. JarKus transect 9011094 is indicated in the figure. It is located at the south of the nourishment.

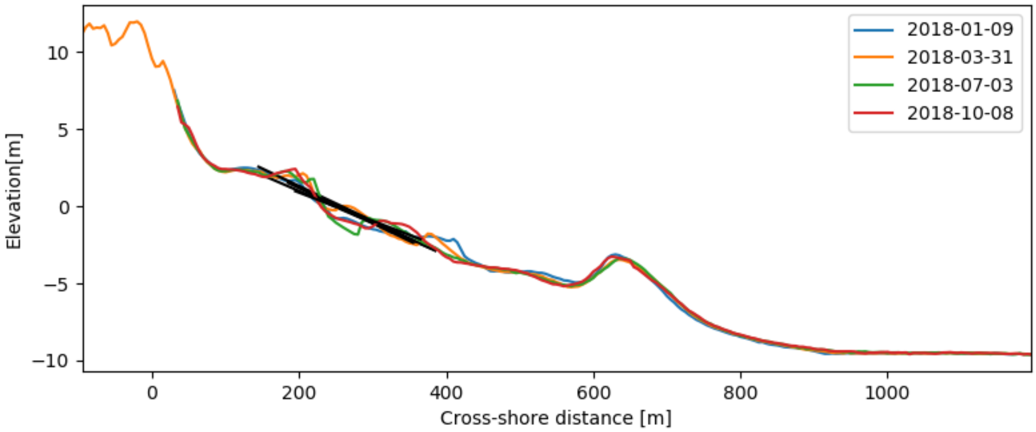

Figure D.2: Profiles observed at JarKus transect 9011094. There were four surveys in 2018. The slopes of the beach face are indicated by the black lines. Especially in autumn, after the calm summer period, the beach face slope seems an underestimate. This period also has the largest regression error.

The observed profiles are plotted in figure D.2. The derived beach face slopes are:

Date	Beach face slope	Standard error
2018-01-09	0.0207 (1 : 48)	±0.0009
2018-03-31	0.0226 (1 : 44)	±0.0009
2018-07-03	0.0228 (1 : 44)	±0.0027
2018-10-08	0.0183 (1 : 55)	±0.0022

It seems that the variation in the slope is mostly caused by the displacement of the bar in the system. In the summer months, the bar moved up in the profile (into the intertidal zone) resulting in flatter intertidal beach slopes. During the storm season the longshore sand bar has moved offshore.

D.3 Satellite derived slopes at transect 9011094

The slopes are computed four times: (1) FAST method, (2) Sagar method, (3) Onrust method and (4) Onrust method without manual filtering. These methods are carefully described in chapter 3.

In the fourth computation the manual filtering (step 0) is omitted. By leaving out the manual filtering step in the fourth method a more objective comparison with the other methods is possible. Because the Onrust method uses individual images, it is more vulnerable to outliers and less robust in morphologically active sites such as the Sand Motor. In addition, fewer images are required compared with the other two methods, so this method is applied to three months of images rather than the whole year.

Figure D.3 presents the fitted slopes for JarKus transect 9011094. The four plots give the slope for the FAST, Sagar, Onrust and Onrust without manual filtering methods respectively. Hereafter, each of the plots is studied in depth.

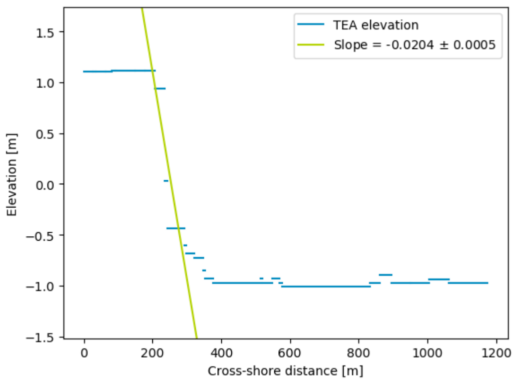

(a) Method FAST

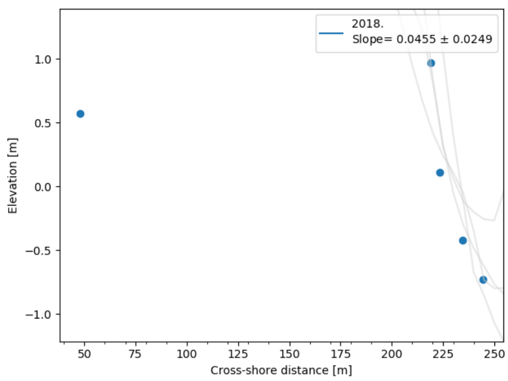

(b) Method Sagar

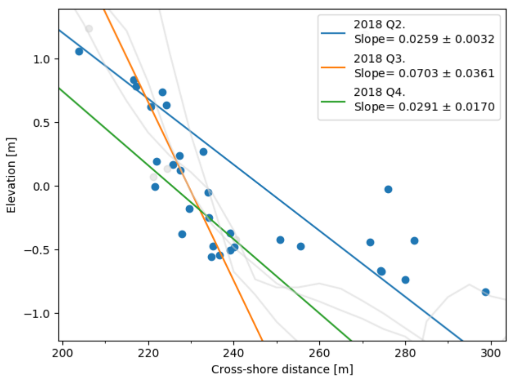

(c) Method Onrust

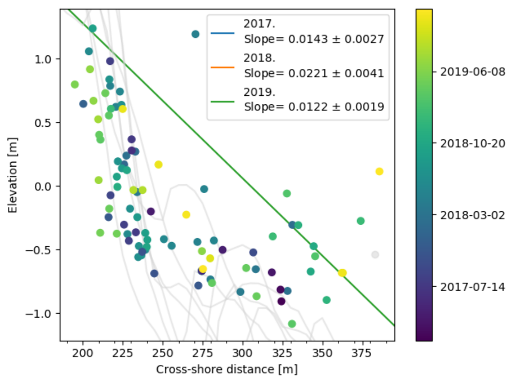

(d) Method Onrust (without manual filtering)

Figure D.3: Intertidal beach slopes for transect 9011094 derived using the three methods discussed. The Onrust method is applied twice (c and d), both with and without manual filtering. The observed profiles are plotted in gray.

Figure D.4: Composite image of the Delfland coast. The 15th percentile was used to create this composite. Images within 60 % to 80 % of the tide are used.

D.3.1 FAST method

Figure D.3a presents the slope as derived using the FAST method (see section 3.2.2). The data points are obtained by mapping the values of the Time Ensemble Averaged (TEA) image to the cross-shore transect. The TEA elevation values in the tails of the plot are HAT or LAT because the probabilities of water occurrence are 1.0 and 0.0 respectively.

A stepped model is fitted to the data points. A linear section is fitted in the intertidal zone. The intertidal beach slope is $0.0204 \pm 0.0\,(1:49)$. This is very close to the observed values.

D.3.2 Sagar method

Figure D.3b shows the satellite derived intertidal beach slope using the Sagar method. The 57 images are grouped per tidal level:
80% - 100% of the tides: 6 images
60% - 80% of the tides: 6 images
40% - 60% of the tides: 10 images
20% - 40% of the tides: 25 images
0% - 20% of the tides: 9 images

Composites are made from the images per tidal level group: the 57 images are reduced to only 5 composites. The Satellite Derived Shorelines (SDSs) are extracted from each composite su that there are 5 data points in the plot. The first and second group contain relatively few images for compositing. Visual inspection of the images (see figure D.4) confirms that the resulting composite is not clear of contaminants such as clouds, cloud shadows and wave foam. Consequently, the SDS is not extracted correctly which explains the outlier in figure D.3b.

The least squares algorithm is applied to fit a linear slope to the data points. The fit represents the intertidal beach slope. According to the Sagar method the gradient of the intertidal beach is $0.0697 \pm 0.0377\,(1:14)$. This is steeper than the slope found in the field. However, the data points seem to fit well to the observed slopes in figure D.3b: the intertidal bar that is formed in summer is not accounted for in the Sagar method.

D.3.3 Onrust method with manual filtering

Figure D.3c and figure D.3d present the beach slopes according to the Onrust method. The first approach, the Onrust method with manual filtering, is discussed here.

By applying the manual filtering the capabilities and potential of a method based on single images can be shown. Such a method captures much more of the variability of the shoreline position. This is also visible in the figures: The waterline points cover the entire range of measured profiles. Besides, there are outliers: these can be attributed to bad image quality or local disturbances.

39 of the 57 remain after manual filtering. The slope of the intertidal beach are calculated using these images. The slope at transect 9011094 ranges from $0.0260 \pm 0.0032\,(1:38)$ to $0.0708 \pm 0.0330\,(1:14)$. This is steeper than the values observed. Similar to the Sagar method the steepest slopes are derived in the absence of the intertidal bar, which has moved further offshore. For calculating the relevant slopes, a larger area is studied which includes a subtidal bar.

D.3.4 Onrust method with automated filtering

Figure D.3c and figure D.3d present the beach slopes according to the Onrust method. The second approach, the Onrust method without manual filtering, is discussed here.

The Onrust method without manual filtering computes a slope of $0.0101 \pm 0.0015\,(1:99)$ in winter and $0.0499 \pm 0.0205\,(1:20)$ in summer. This large variation is the result of a bar in the intertidal zone, as is seen in figure D.3d.

E Estimating the grain size using equilibrium beach profiles

This thesis proposes an approach for using equilibrium beach profiles to derive the sediment grain diameter. Extraordinary about this approach is that the shape of the profile is unknown; only the gradient of the intertidal zone has been determined. This appendix applies this approach to the intertidal beach slopes at the Delfland coast to prove that this approach fails in determining a robust estimate of the median grain diameter.

E.1 Introduction

The term *equilibrium beach profile* refers to the state of the beach that would arise in a situation with constant forcing by the environmental conditions. The beach profile is constantly converging to this state but due to the everchanging conditions never reaches this state.

Equilibrium beach profiles are empirical relations intertidal for describing the shape of the beach profile. Appendix B discusses several models; some of which can be applied prognostically, others only in a descriptive manner. This appendix addresses the question of whether it is possible to apply these models to the intertidal zone. It does that by looking at the observed profiles to minimise errors by other influences.

E.2 Estimating grain size from full profile

Equilibrium beach profile models are not specifically intended for describing the shape of the beach face but for describing the shape of the entire profile. Therefore, this approach is first checked by fitting the models to the full measured profile at the Delfland coast. Even though there are many more models available, this appendix only focusses on the models described in appendix B:

- Bruun model (Bruun, 1954)
- 2-Step equilibrium beach profile model (Bernabeu et al., 2003)

A least squares algorithm is applied to find the best fit to the observed profiles. Only the section below the highest astronomical tide (HAT) is included because the equilibrium beach profiles only include the profile below the waterline. The models are fitted to the measured profiles so that their shapes match. This is done for each profiles, see figure E.1.

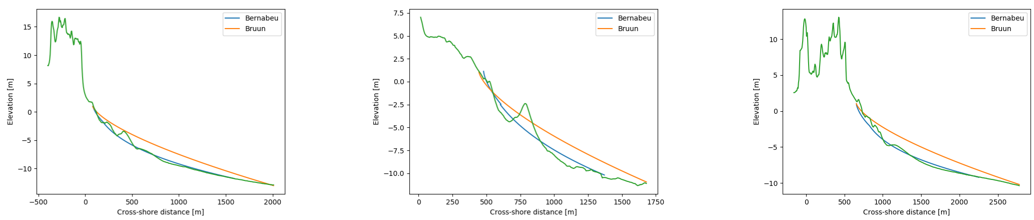

Figure E.1: Equilibrium beach profiles fitted to the measured slopes.

The parameters A and Ω are the fitting parameters for the Bruun and Bernabeu models respectively. These follow from the fit. Subsequently, the median grain size is estimated from the parameters. This is explained in appendix B.

Figure E.2 presents an overview of the grain size estimates along the Delfland coast. The estimated grain sizes for Bruun's and Bernabeu's model are plotted.

The Bruun model predicts too large grain diameters: nearly all predictions are in the gravel range, whereas the observed sediment is medium sand. The Bernabeu model leads to better results. The 2-step equilibrium beach profile (Bernabeu et al., 2002) slightly overestimates the grain size.

Since the environmental conditions are always changing it is not exactly clear which wave characteristics should be used in the equilibrium beach profile relations. As a first estimate the average conditions are used. Optimisation of the wave characteristics could improve the grain size estimate.

E.3 Estimating grain size from intertidal beach slope

In the previous section it is shown that the 2-step equilibrium beach profile looks promising for estimating the median grain size. However, when limiting to the intertidal zone it is likely to become more difficult to produce a proper fit. For example, the Bruun model predicts an infinite slope at the shoreline.

The same approach as for the full profiles is applied to the intertidal beach to find an estimate of the grain size. Figure E.3 presents the median grain sizes at the different transects along the Delfland coast.

It is clear that the grain diameter estimated using the Bruun model shows poor agreement with the observed values. The Bernabeu model performs better, but when the 2-step equilibrium beach profile is fitted to the section of the profile in the intertidal zone, the predicted grain sizes are scattered over the plot. Obtaining a proper fit can no longer be expected; the errors in the predicted values are large.

E.4 Conclusion

In this chapter it has been proven that equilibrium beach profiles can indeed be used to find a relation between the profile shape and the median grain size. One of the oldest models, the Bruun model, does not seem to perform very well, but newer models such as the Bernabeu model are very promising.

However, this thesis suggests an approach where only the section of the profile in the intertidal zone is used. The slope of this section, also referred to as the beach face

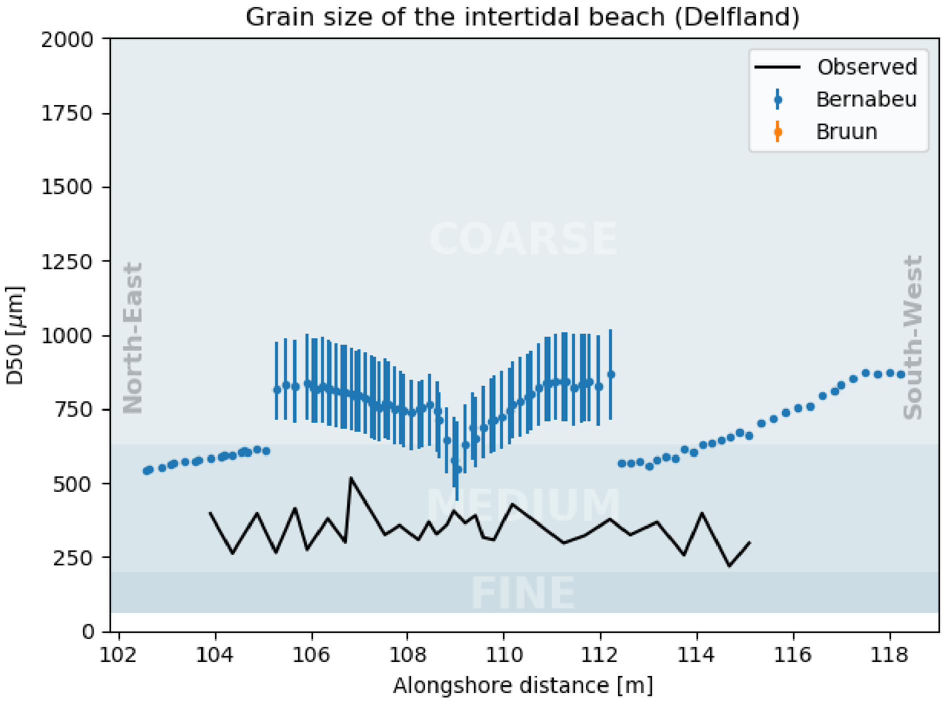

Figure E.2: Sediment size ($d50$) at the Delfland coast derived using the equilibrium beach profile approach. Two equilibrium beach profiles are applied: Bernabeu et al. (2003); Bruun (1954). The models are fitted to the entire profile. The bars indicate the spread of the estimate as a result of slope variability.

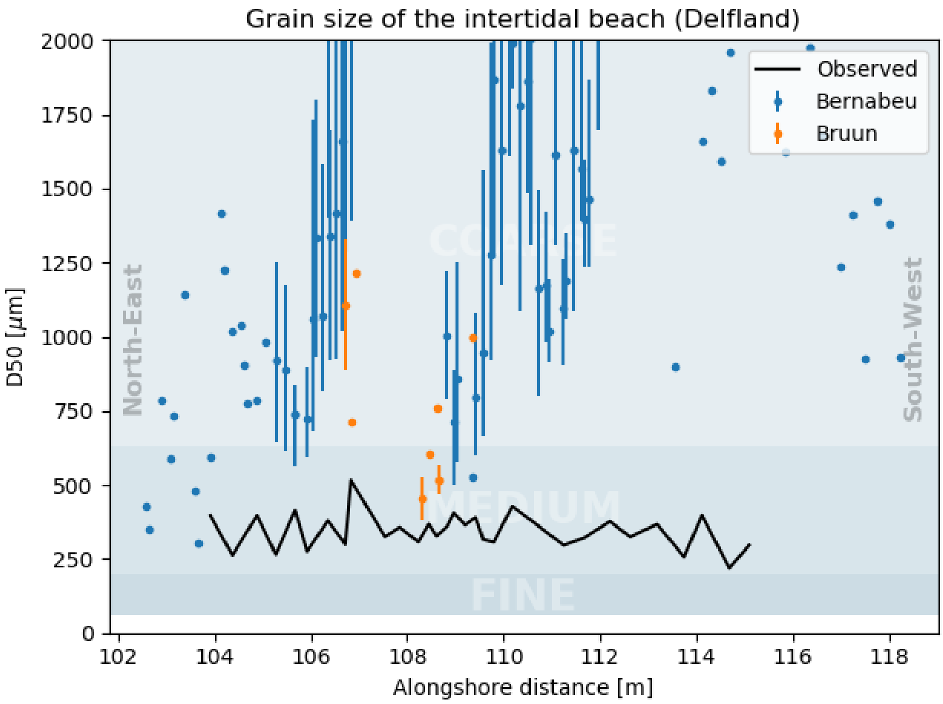

Figure E.3: Sediment size ($d50$) at the Delfland coast derived using the equilibrium beach profile approach. Two equilibrium beach profiles are applied: Bernabeu et al. (2003); Bruun (1954). The models are fitted to the section of the profile in the intertidal zone. The bars indicate the spread of the estimate as a result of slope variability.

slope, can be derived from optical satellite imagery. This opens up the possibility of deriving the sediment size on a global scale, but not using the proposed method with equilibrium beach profiles.

To conclude, this appendix shows that equilibrium beach profiles are not intended and cannot be used for describing the shape of the intertidal beach.

E.5 Sneak preview into using the beach face relations

A sneak preview of the computation using beach face slope relations is given in figure E.4. Three beach face slope relations are used: Bujan et al. (2019); McFall (2019); Sunamura (1984).

Sunamera predicts a grain size in the clay range; the grain diameter is extremely small. The Sunamera relation does not seem to work here, probably because the slope is too flat for the Sunamera relation. The McFall relation performs excellent and predicts a medium sand, as has also been observed in the field. The Bujan relation underestimates the grain size and results in a fine sand. At first sight however, it still results in a very good estimate.

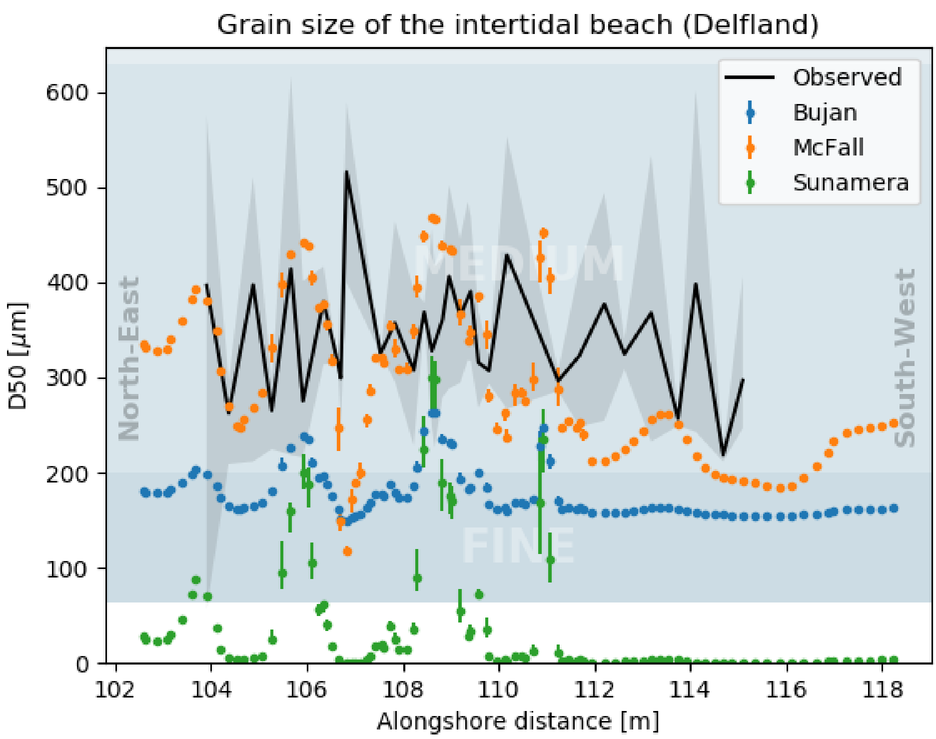

Figure E.4: Sediment Delfland. The bandwith around the observed size indicates the difference between the measurements.

F Intertidal beach slope derivation at the Ebro Delta Coast

The Ebro Delta is located on the Mediterannean coast in Spain. The delta region is used for a case study for deriving the intertidal beach slopes in this appendix. First a description of the study site is given, then the satellite derived slopes are studied.

F.1 Study site

The Ebro river flows into the Mediterranean Sea in the north of Spain. At it's mouth a large delta has formed. Due to the irregular river flow, the Ebro Delta shows both river-dominated patterns and wave-dominated patterns. As a result of the damming of the Ebro river, the delta is now mainly wave-dominated. Combined with sea level rise (SLR) and land subsidence, a large part is expected to flood in the next centuries. Figure F.1 shows the very distinct shape of the delta.

Figure F.1: Satellite image of the Ebro Delta captured in January 2018 by a Landsat satellite (NASA).

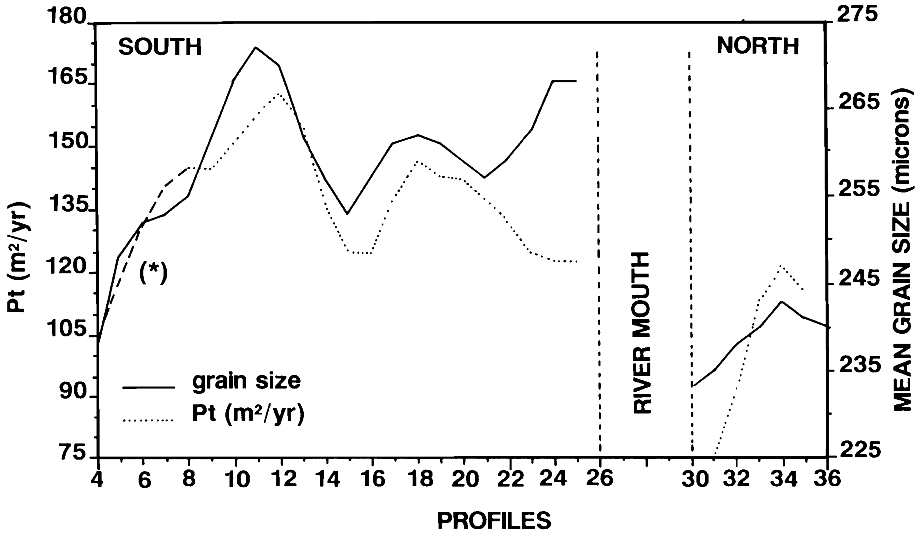

Figure F.2: Alongshore distribution of the grain size and wave energy.

F.1.1 Sediments supplied by the river

The Ebro Delta has a 50 km long sandy shoreline. Sediments have a fluvial origin and are distributed over the Delta by the forces of the waves. Guillén & Jiménez (1995) found that there is a large alongshore sorting in the grain size. Figure F.2 shows the distribution of grain size along the delta. The figure shows a clear correlation between wave power and the grain size. The mean grain size along the Ebro Delta coast ranges from 235 μm to 270 μm.

The variation of the wave power is mainly the result of the orientation of the shoreline. Due to the shape of the delta, there is a large variation in the incident wave angle. As the incident wave power reflects the energy to transport sediments, coarsest sediments are found in the areas with the most wave power. Selective transport of finer sediments leads to the progressive coarsening in these areas (Guillén & Jiménez, 1995).

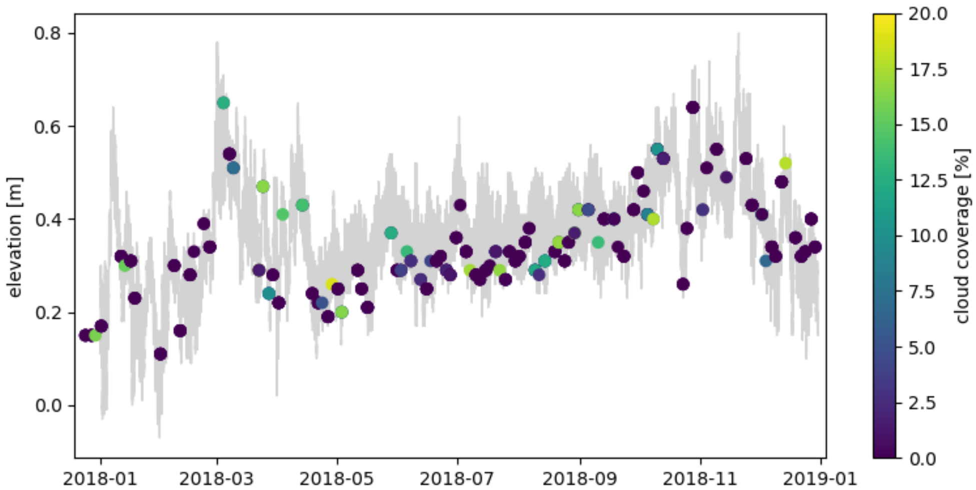

Figure F.3: Distribution of images in time plotted against the water level. Each dot represents an image. The water levels have been measured at the port of Tarragona.

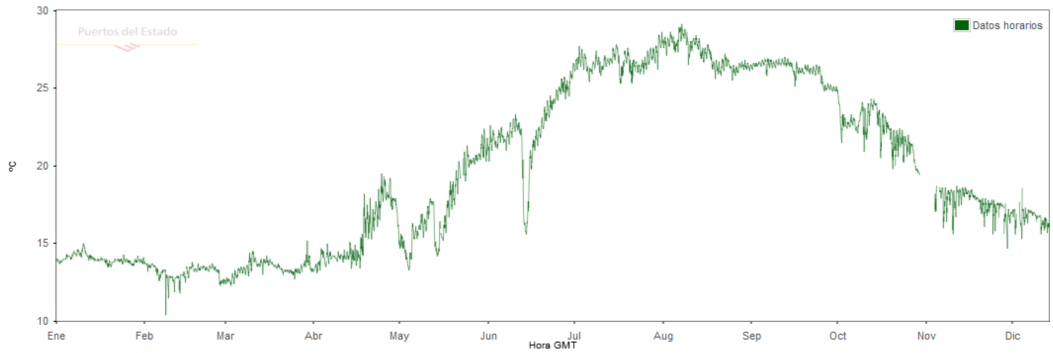

(a) Time series of the water temperature

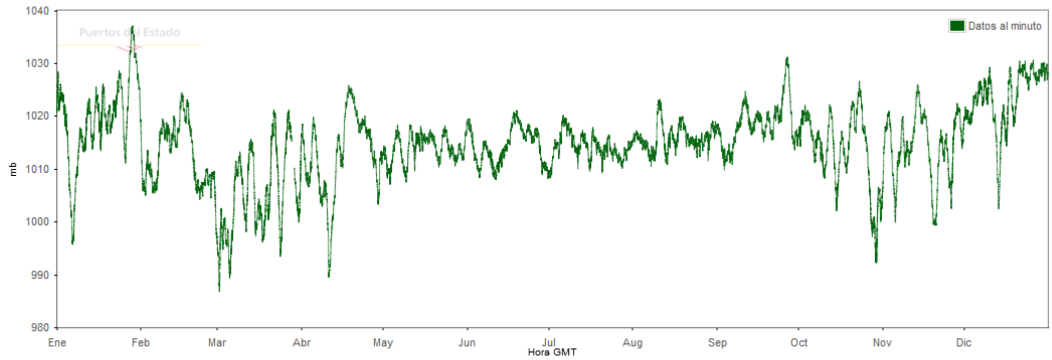

(b) Time series of the atmospheric pressure

Figure F.4: Time series of the meteorological conditions at Tarragona Port in 2018.

F.1.2 Microtidal environment

Like most of the Mediterranean coast the Ebro Delta is a microtidal environment, with an astronomical tidal range of 0.25 m. The water levels are recorded at the port of Tarragona* which is about 60 km to the north.

The tidal elevation is plotted in figure F.3 (gray line). It can be seen that the tidal range is small ($\mathcal{O}$ 0.25 m). In addition, there seem to be other mechanisms that control the waterlevel on the longer time scales. Figure F.4 shows two plots containing the time series of the water temperature and the atmospheric pressure at Tarragona Port.

Density effects (mainly temperature) seem to explain the gradually increasing water level in summer. Storm events (associated with low atmospheric pressures) can also be observed in both figure F.3 and figure F.4b. For example, at the beginning of March 2018 Storm Emma passed over Western Europe. Air pressure was clearly lowered in this period, at the same time a peak in the water level is found. In conclusion, it appears that the meteorological tide is of greater magnitude then the astronomical tide.

*Obtained from https://portus.puertos.es

Figure F.5: Satellite image of the Ebro Delta coast for 27-12-2017. one for the tile with *ID* 31TCF and the other for the tile with *ID* 31TBF.

F.1.3 Satellite images

The satellite images are also indicated in figure F.3. A total number of 399 Sentinel-2 scenes are analysed. All images are made in 2018. The large amount can be explained by the size of the region: the Ebro Delta spans multiple Sentinel-2 image tiles. This also means that most images only cover a part of the region. Especially in the summer months, a clear bias to the lower water levels is observed.

F.1.4 Sensitivity of Otsu thresholding

Shorelines are extracted from the imagery using Hagenaars's approach. Due to the size of the Ebro Delta, the sensitivity of the Otsu thresholding algorithm is clearly illustrated.

Sentinel-2 images are recorded in a continues datatake and are later subdivided into tiles for easier processing. These tiles are overlapping at the edges. Figure F.5 shows the satellite images of 27-12-2017 from the Ebro Delta coast. Two shorelines are delineated: one for each of the overlapping tiles.

At the indicated transect (upper right of the image) the difference between both shorelines is 6 metres, but in the more muddy sections at the bottom of the image differences grow to more than 20 metre.

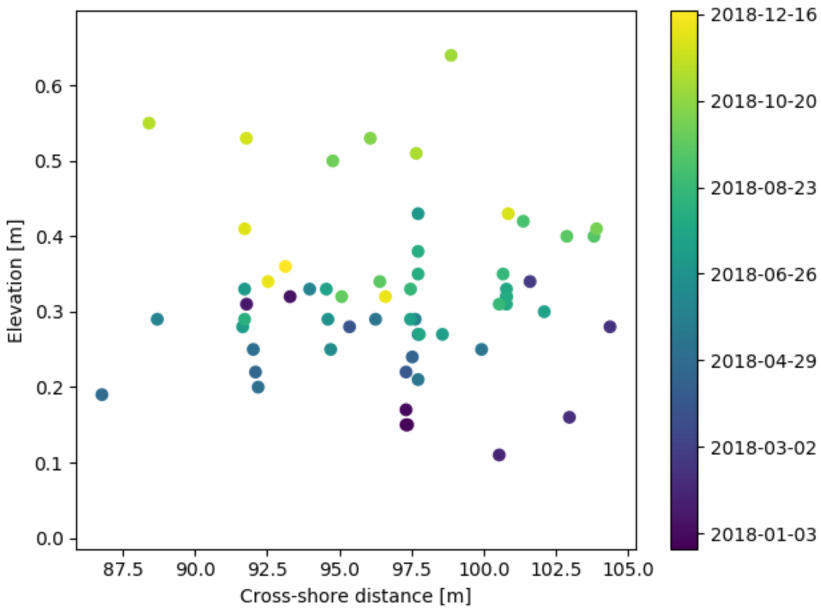

Figure F.6: Waterline points at the Ebro Delta coast near profile 15. The horizontal axis shows the cross-shore distance of the shoreline, the vertical axis the water level elevation at that moment. The range of cross-shore distances is small: around the size of a single pixel.

Since the pixel values in both tiles are exactly the same this example demonstrates the sensitivity of the Otsu thresholding algorithm. It appears that it is not as user-independent as previously assumed.

F.2 Satellite derived slopes

The Satellite Derived Shorelines are derived for all images; the Onrust method (see section 3.8) is applied to derive the intertidal beach slopes. Figure F.6 shows the horizontal locations of the shorelines plotted against the elevation of the water level for a cross-shore transect. This transect is located south of the river mouth around profile 15.

The tidal difference between the points is small. Consequently, the cross-shore distances have a small range of approximately 15 m. This is only slightly larger than the pixel resolution. Taking into account the uncertainty in the shoreline position (Hagenaars et al., 2018), this means that the extent of the tidal zone is too small to derive an intertidal beach slope.

G Improved temporal resolution of satellite derived intertidal beach slopes

So-far the intertidal beach slopes are derived from yearly collections of images. However, single image methods, suchs as the Onrust method, offer the possibility to look at smaller time scales in order to obtain the variability of the slope. In this appendix, the intertidal beach slopes are derived per season.

G.1 Temporal resolution

The Onrust method extracts the shorelines from single images such that a Satellite Derived Shoreline (SDS) is derived for every image. With a minimum of 10 shorelines it is possible to make a good estimate of the slope of the intertidal beach. Sentinel-2 has a return period of 5 days, so after 50 days sufficient images are acquired. The robustness increases with the number of images, but decreases with time as there is a natural variability of the beach face slope.

Figure G.1 shows that the tropics and the mid-latitudes have high cloud frequencies. Clouded images cannot be used for extracting SDSs; consequently, longer time spans are required in areas with frequent cloud coverage. A three month period is selected as a compromise.

For simplicity the three month periods are not chosen analogous to the seasons. Instead, quarters are used:

Q1 - January, February, March
Q2 - April, May, June
Q3 - July, August, September
Q4 - October, November, December

The quarterly intertidal beach slopes are derived for the three study sites considered in this thesis.

G.2 Delfland

Figure G.2 shows that the performance of the Onrust methods differs very much per season. In winter, hardly any slopes are derived; in spring the satellite derived slopes seem to converge to the observed slopes. This seasonal effect is related to the quality

Figure G.1: Mean annual cloud frequency in percentage from Wilson & Jetz (2016). The cloud frequencies are developed from 15 year of twice-daily Moderate Resolution Imaging Spectroradiometer (MODIS) scenes. White indicates that a location is always clouded; black indicates cloud-free locations. No data is available over the large ocean basins.

		Coverage	*RMSE*
Method Onrust	2018 Q1	0.15	0.0152
	2018 Q2	0.96	–
	2018 Q3	0.79	0.0119
	2018 Q4	0.63	0.0324

Table G.1: Summary of the coverage and *RMSE* for the Onrust method per quarter at the Delfland coast. There were no surveys in Q2, thus no error has been calculated.

of the satellite imagery: the Dutch storm season (a lot of clouds and waves) is in autumn and winter.

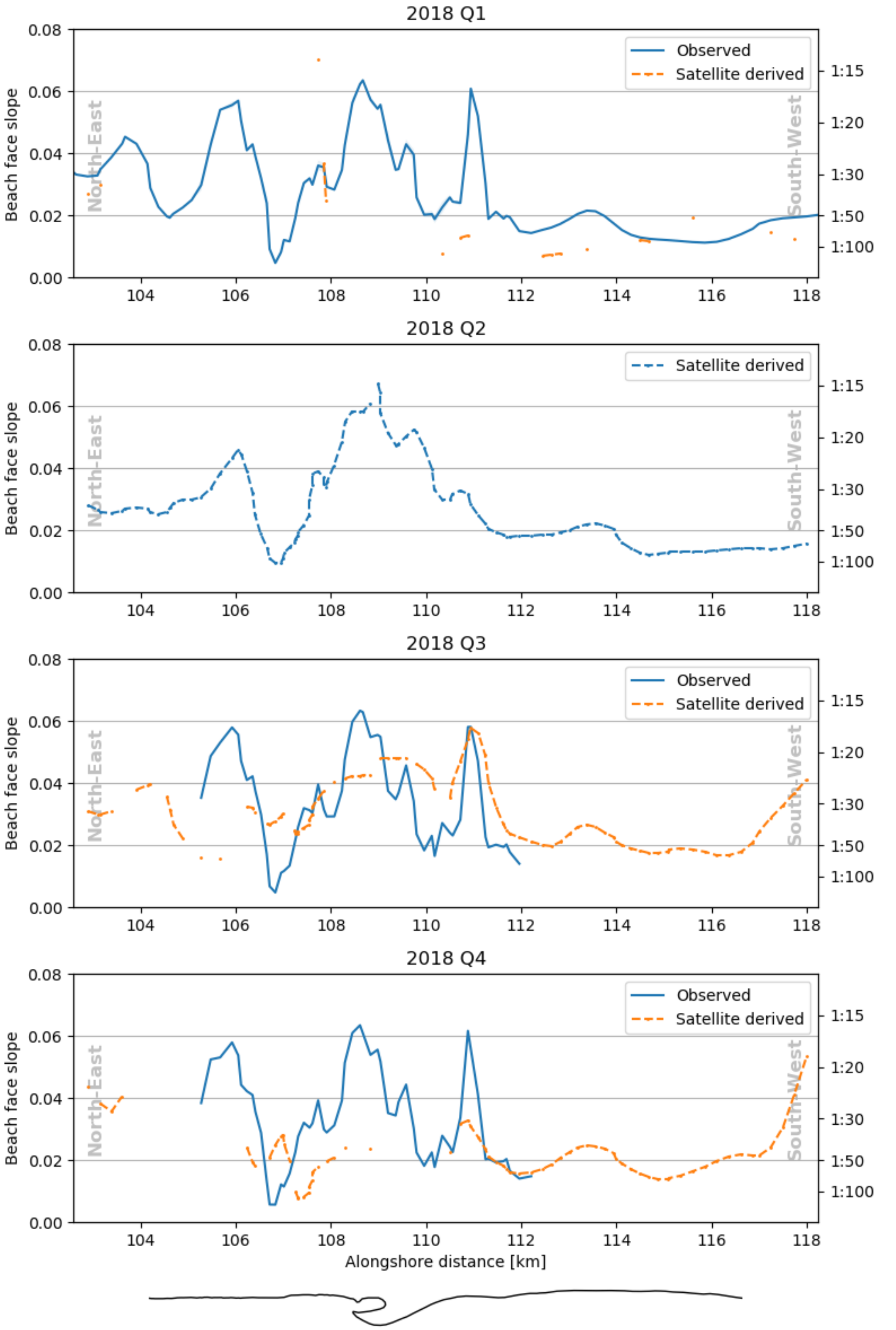

Figure G.2: The intertidal beach slopes as observed and satellite-derived using the Onrust method. The slopes are computed per three-month period. The slopes are plotted against the alongshore position at the Delfland coast. Images are first manually screened for clouds, shadows and waves. The bandwidth around the observed slopes indicate the variability.